Resolvent Analysis of Non-stationary Turbulent Flows and Transient Flow Phenomena

Thesis by

Eric Ballouz

In Partial Fulfillment of the Requirements for the
degree of
Doctor of Philosophy in Mechanical Engineering

CALIFORNIA INSTITUTE OF TECHNOLOGY
Pasadena, California

2025
Defended February 24th, 2025

ACKNOWLEDGEMENTS

My adviser Jane joined Caltech shortly after myself, and I have the privilege of being her very first graduate student. Jane's knowledge of the field is staggering, her advice, be it technical or professional, always pertinent and useful. She is organized and meticulous, and all-in-all an exemplary role model for aspiring academics. I am immensely grateful that she agreed to serve as my adviser.

I would also like to thank the rest of my committee for their support throughout my PhD journey: Professors Tim Colonius, Adrian Lozano-Durán, and John Dabiri. Tim is a cornerstone of the mechanical engineering department; his classes, advice, and insight during seminars have invaluably shaped this thesis. Adrian's innovative and rigorous research is an inspiration, and his comments on my work have always led to its improvement. John first made his mark on me when he served on my candidacy committee; his stimulating questions pushed me to contemplate aspects of my research that I had not considered. His curiosity and collegiality are admirable qualities that enrich the aerospace and mechanical engineering departments.

I am grateful to my collaborators, Professor Scott Dawson and his former student Dr. Barbara Lopez-Doriga. Scott is a patient and encouraging mentor who is always ready to provide incisive remarks and creative ideas. Barbara's creativity and diligence are likewise inspiring. Working with her has been a pleasure, one that I hope to repeat in the future as we advance in our careers. I am deeply thankful to have gotten to know such a warm person.

I am additionally thankful for my colleagues in the group whose commitment to research, inquisitiveness, and welcoming spirit create an environment I hope to emulate when I one day form my own research group. Their interest in my work, made apparent through the deep questions they raised during our group meetings, has raised the standards I hold for myself. Thank you Di, Emma, Diederik, Xinyi, Micah, Mickey, and Ching-Te. I am also grateful for the administrative staff of the mechanical engineering department, especially Jenni and Lynn. They make the department a uniquely welcoming and functional work environment.

A doctorate degree is often seen as a sort of transitory period, a stepping stone into the "real world". But six years of one's life is quite a long time to be stuck in what some simply consider to be a transition. During my years in the greater Los Angeles area, I can safely say that I lived a full life thanks to my community of friends and my family. I thank Daniel, Lana, Rita, Tracy, Stephanie, Leo, Katie, and Ben for their love and companionship. I thank my grandparents, Yvette and Joseph, for their warmth and pride in me, as well as our weekly video calls that have allowed me to maintain a connection to my home. I thank my mother, Mary-Anne, for her support and uplifting encouragement. I thank them for making this thesis but a small part of the last few years. I am incalculably grateful to them all, now and always, for being my companions in the life I lived here in Pasadena, and the one I have yet to live after I graduate.

ABSTRACT

In this work, we develop a wavelet-based formulation of resolvent analysis in order to extend the method to transient phenomena and non-stationary flows. We apply this method in two ways: first, to analyze systems that were not previously amenable to traditional resolvent analysis, and second, to probe the limits of the resolvent forcing modes' "optimality" in a nonlinear simulation as well as investigate the mechanisms that suppress their effectiveness. In wavelet-based resolvent analysis, the Navier-Stokes equations are linearized about a mean profile, Fourier-transformed in the homogeneous directions, and wavelet-transformed in time. The nonlinear terms are represented as forcing terms acting on the system, and a maximally perturbing forcing mode and the response it produces are then computed for this linear system. The wavelet formulation enables the forcing and response modes to represent transient trajectories. By windowing the wavelet-based resolvent operator, we can also compute optimal forcing modes restricted to a time-localized pulse along with their transient response.

For the first application of the method, we use the windowing approach to study bursting in channel flow. The optimal response mode grows and decays in time scales that match turbulent data, and we show that this optimal burst exploits the Orr mechanism. We also study channel flow subjected to a spanwise pressure gradient. The corresponding resolvent modes mirror the mean flow and gradually realign themselves according to the new flow conditions. More interestingly, they exhibit a collapse of the lift-up mechanism during this realignment, which offers an explanation to the depletion of tangential Reynolds stresses in the turbulent system.

For the second application of the method, we inject time-localized resolvent forcing modes for the minimal flow unit into a simulation of the system, at different intensities. The principal resolvent forcing mode is much more effective than a randomly generated forcing structure at amplifying the near-wall streak. For initial times and close to the wall, the turbulent minimal flow unit matches the principal response mode well, but due to nonlinear effects, the response decays prematurely. By computing the nonlinear energy transfer to secondary scales, we find that the breakdown of the actuated mode proceeds similarly across all forcing intensities: in the near-wall region, the induced streak forks into two branches, while in the outer region, the streak breaks up in the streamwise direction. In both regions, spanwise gradients account for the dominant share of nonlinear energy transfer.

PUBLISHED CONTENT AND CONTRIBUTIONS

Ballouz, E., Dawson, S. T. M., & Bae, H. J. (2024). Transient growth of wavelet-based resolvent modes in the buffer layer of wall-bounded turbulence. *J. Phys.: Conference Series*, *2753*(1), 012002. https://doi.org/10.1088/1742-6596/2753/1/012002
The authors all contributed to designing the project. E. Ballouz wrote the code and performed the numerical experiments presented in the work. E. Ballouz also conducted the data analysis and wrote the article.

Ballouz, E., Dawson, S. T. M., & Bae, H. J. (2025). Transient growth and nonlinear breakdown of wavelet-based resolvent modes in turbulent channel flow [Submitted]. *arXiv preprint arXiv:2502.08670*. https://doi.org/10.48550/arXiv.2502.08670
The authors all contributed to designing the project. E. Ballouz modified H. J. Bae's existing simulation code to perform the numerical experiments presented in the work. E. Ballouz conducted the data analysis and wrote the article.

Ballouz, E., Lopez-Doriga, B., Dawson, S. T. M., & Bae, H. J. (2024). Wavelet-based resolvent analysis of non-stationary flows. *J. Fluid Mech.*, *999*, A53. https://doi.org/10.1017/jfm.2024.903
The authors all contributed to designing the project. E. Ballouz wrote the code and performed the numerical experiments presented in the work. E. Ballouz also conducted the data analysis and wrote the article.

Ballouz, E., Lopez-Dóriga, B., Dawson, S. T. M., & Bae, H. J. (2023). Wavelet-based resolvent analysis for statistically-stationary and temporally-evolving flows. *AIAA SCITECH 2023 Forum*, 0676. https://doi.org/10.2514/6.2023-0676
The authors all contributed to designing the project. E. Ballouz wrote the code and performed the numerical experiments presented in the work. E. Ballouz also conducted the data analysis and wrote the article.

López-Doriga, B., Ballouz, E., Bae, H. J., & Dawson, S. T. M. (2023). A sparsity-promoting resolvent analysis for the identification of spatiotemporally-localized amplification mechanisms. *AIAA SCITECH 2023 Forum*, 0677. https://doi.org/10.2514/6.2023-0677
E. Ballouz met the first author regularly to discuss the project and occasionally provided feedback and suggestions.

López-Doriga, B., Ballouz, E., Bae, H. J., & Dawson, S. T. M. (2024). Sparse space–time resolvent analysis for statistically stationary and time-varying flows. *J. Fluid Mech.*, *999*, A87. https://doi.org/10.1017/jfm.2024.955
E. Ballouz met the first author regularly to discuss the project and occasionally provided feedback and suggestions.

TABLE OF CONTENTS

LIST OF ILLUSTRATIONS

LIST OF TABLES

Chapter 1

INTRODUCTION

The equations governing the motion of fluids are concise—a momentum conservation equation for each spatial direction and an equation of mass conservation—but their apparent simplicity belie an ability to describe phenomena of a staggering richness and complexity. The mission to better understand the physics of fluids is an old one—Archimedes' *On Floating Bodies* dates back to the third century BC, though the modern and more complete equations of motion were formulated a little more recently, in the mid-nineteenth century, by Claude-Louis Navier and George Gabriel Stokes—and has engaged a wide array of disciplines, combining pen-and-paper analysis, experiments, and the design of numerical solvers and models.

One aspect of fluid mechanics that continues to inspire a large number of its scholars is the tendency of turbulent fluids to organize themselves into ordered structures. From vortices at the wingtips of birds to the whirling of storms in our atmosphere, the chaotic flow of fluids manages to produce identifiable coherent shapes. The emergence of order from chaos, beyond just lending itself to poetic contemplation, has important implications for the quest to hone our mastery of fluid mechanics. These coherent structures are often energetic, and understanding their behavior—their birth, motion, interactions, and disappearance—can lead to interpretable insights about the physics of fluids, without having to fully simulate the Navier-Stokes equations. After all, shoals of fish manage to deftly navigate the deep ocean currents without solving partial differential equations at each relevant scale of motion, and probably only react to the perceptible and energetic components of the flow. A better understanding of coherent structures is especially rewarding for the design of more efficient vehicles, or the modeling of systems too complex to simulate fully.

1.1 Coherent structures in wall-bounded turbulence

A canonical system that turbulence researchers often consider is the wall-bounded flow. This type of flow is extremely relevant to the design of vehicles, but also to the modeling of atmospheric and oceanic flows close to the ground or ocean bed, respectively. Wall-bounded flows are the topic of this work, though we only consider simplified geometries, primarily flow within a channel. We work with an idealized channel in a numerical setting: two parallel infinite walls between which an incompressible turbulent fluid is flowing. There are no side walls; the domain boundaries along and transverse to the flow are periodic. At the top and bottom walls, the fluid satisfies the no-slip and no-penetration boundary conditions. We refer to the flow direction as "streamwise", the axis stretching from the bottom-wall to the top as "wall-normal", and the remaining direction as "spanwise". Both direct numerical simulations (DNS) of this idealized case and physical experiments within channels reveal the presence of coherent structures: elongated regions of low and high velocity near the wall stretching in the direction of the flow (the streamwise direction). These streamwise streaks are paired with streamwise rolls—sweeping motions in the cross-flow plane, rotating about the streamwise axis.

These structures have been decisively measured and extracted from numerical and experimental data through, for example, spatiotemporal correlations (Abreu et al., 2020; Berkooz et al., 1993; Borée, 2003; Lumley, 1967, 2007; Mezić, 2013; Tissot et al., 2021). The shape and life-cycle of these roll/streak pairs, as well as their interactions with the rest of the flow, have been extensively studied (Adrian, 2007; Bakewell & Lumley, 1967; Blackwelder & Eckelmann, 1979; Johansson et al., 1987; H. T. Kim et al., 1971; Klebanoff et al., 1962; Kline et al., 1967; Robinson, 1991; Smith & Metzler, 1983; Smits et al., 2011). The persistent generation of streamwise streaks from spanwise rolls and their subsequent breakdown which regenerates rolls form what is dubbed the self-sustaining process. This quasiperiodic cycle can be more clearly observed in a minimal flow unit (Jiménez & Moin, 1991): a channel restricted in the streamwise and spanwise directions in order to exclude the dynamics of the outer region of the channel. Recent methods based on graph-theoretic approaches (Elnahhas et al., 2024) provide new evidence of the self-sustaining process in larger channels as well by revealing consistent patterns of energy exchange between rolls and streaks. Many works are dedicated to understanding the mechanisms that drive this cycle (Butler & Farrell, 1993; Chernyshenko & Baig, 2005; Del Alamo & Jiménez, 2006; Hamilton et al., 1995; Jiménez, 2018; Landahl, 1980; Panton, 2001). The organization of near-wall turbulence into energetic rolls and streaks has inspired the pursuit of lower-dimensional models, wherein the high-dimensional wall-bounded flow is summarized by the dynamical evolution of large structures.

Streaks and rolls are staples of turbulent channel flow, which is stationary—it is homogeneous in time and its average statistical properties are time-invariant. A time-varying mean flow, however, can greatly influence the behavior of turbulence.

When a spanwise pressure gradient is applied to channel flow causing the flow to rotate, the turbulent Reynolds stresses counterintuitively decrease, initially (Lozano-Durán et al., 2020). The newly formed rolls, positioned more closely to the wall and oriented in the direction of the rotating flow (and thus misaligned with the traditional streamwise rolls) are believed to disrupt the streak generation process. In an other non-stationary configuration, where the top and bottom walls of the channel oscillate in tandem, the flow can alternate between laminar and turbulent regimes (Blondeaux & Vittori, 1994; Verzicco & Vittori, 1996; Vittori & Verzicco, 1998). Coherent structures in non-stationary turbulent flows can behave and interact in unexpected ways, and illuminating their time-varying behavior would expand our understanding turbulence. The analysis of these flows is a core motivation of this thesis.

1.2 Linear analysis of turbulence

As mentioned, one approach used to characterize coherent structures relies on the wealth of data generated by recent DNS, and newly developed data-driven approaches have indeed produced many insights on the creation and destruction of coherent structures (Elnahhas et al., 2024; Lozano-Durán & Arranz, 2022; Picard & Delville, 2000; Taira et al., 2017; Towne et al., 2018). Another branch of this field is centered on understanding the generation and sustenance of coherent structures through the direct analysis of the properties of the equations of motion. To simplify their analysis, the Navier-Stokes equations are often linearized. Nonlinear mechanisms are essential to turbulence, but much insight can be gleaned from considering the linearized equations. In particular, the linearized equations become amenable to the rich array of mathematical tools developed for the analysis of linear operators.

The linear analysis of flows usually proceeds as follows: the equations of motion are linearized about a base profile, traditionally the laminar steady state solution; linear equations are formulated for the velocity and pressure fluctuations about this base flow and their stability properties investigated (Schmid et al., 2002). One important result for inviscid shear flows with a monotonic base profile is the Fjørtoft criterion (Fjørtoft, 1950), which states that, in order for perturbations to be unstable, the base velocity profile must have an inflection point such that the concave portion of the flow is below the convex portion (or equivalently, the mean vorticity must be a maximum at the inflection point). Results and analysis methods have also been derived for viscous shear flows, mainly by considering the eigenvalue spectra of the linear operators acting on the perturbations (Schmid et al., 2002). These methods have been used as a theoretical basis for investigating the transition to turbulence: unstable perturbations grow to the point where nonlinear effects cannot be neglected and turbulence is tripped.

Another insight from linear analysis is that flows need not be unstable to perturbations in order to transition to a turbulent state. Perturbations about certain globally stable base flow configurations—wall-bounded shear flows, for example—can still grow significantly, even if they are doomed, in the purely linear setting, to eventually decay to zero. It is during the transient growth of perturbations that the assumption of linearity can break down and the flow risks turning turbulent. In such flows that sustain the intense transient growth of perturbations, an "optimal" initial condition is sought. The optimal initial condition is defined such that, when integrated up to a specified time using the linearized equations, it leads to a state of maximal kinetic energy. In short, this optimal perturbation theory, introduced in Böberg and Brösa (1988) and Butler and Farrell (1992), seeks to uncover the most perturbing initial condition and the structures it generates. What is remarkable is that the optimal initial conditions for channel flow (Butler & Farrell, 1992, 1993) tend to resemble the aforementioned streamwise rolls, which, when integrated forward in time, produce streamwise streaks. Linear analysis thus offers an explanation to the structure of near-wall turbulence: out of the noise of perturbations arising from the nonlinear dynamics shuffling energy across scales, the ones aligned with the optimal perturbation—rolls in the case of channel flow—are preferentially amplified by the linear dynamics of the flow and grow into powerful streaks that overwhelm other structures.

In addition to their theoretical tractability, linear mechanisms play a role in physical flows and are often believed to be fundamental drivers of wall-bounded turbulence (Chernyshenko & Baig, 2005; Del Alamo & Jiménez, 2006; Jiménez, 2013; Lozano-Durán et al., 2021; Panton, 2001). One such mechanism is the Orr mechanism (Orr, 1907), in which the mean shear profile near the wall tilts wall-normal velocity perturbations forward in the streamwise direction, stretches vertical scales, and washes out wall-normal gradients; to preserve continuity, wall-normal fluxes and velocity perturbations are magnified, which in turn intensifies streamwise perturbations through cross-component coupling. The role of the Orr mechanism in producing long-lasting streamwise velocity perturbations and sustaining turbulent channel flow has been investigated in Encinar and Jiménez (2020) and Jiménez (2013, 2015). We discuss the Orr mechanism in detail in Chapter 4.1. Another example is lift-up (Hwang & Cossu, 2010), which occurs when wall-normal velocity perturbations transport slow-moving fluid near the wall away into the faster flow field farther away from the wall, where it can be accelerated by the faster mean flow. Modulating lift-up can significantly impact the Reynolds stresses in turbulent channel flow; this is discussed in Chapter 4.2.

Many offer further evidence that linearly-driven transient growth is a prominent driver turbulent fluctuations (Del Alamo & Jiménez, 2006; Pujals et al., 2009). These works show that, even after removing the nonlinear term from the perturbation equations, linear transient growth via the mean shear generates the dominant (streaky) structures in wall-bounded turbulence. The linearized system additionally accounts for much of the energy spectra and reproduces the self-similar profile in the logarithmic region. In a similar vein, Lozano-Durán et al. (2021) show through numerical experiments that the minimal flow unit can sustain turbulence without the nonlinear feedback between the velocity fluctuations and the mean velocity profile, except when the Orr-mechanism or push-over—the momentum transfer to the streamwise velocity perturbation that is enabled by the spanwise mean shear—are suppressed.

Disentangling the roles of lift-up and pushover in energizing near-wall streaks is a subject of ongoing research. Most recently, Markeviciute and Kerswell (2024) tackle the problem by employing an alternate linearization scheme, in which the base flow is a sum of the traditional channel flow profile and a near-wall streak from optimal perturbation theory "frozen" at its maximum amplification. They investigate the transient growth of secondary, smaller scale perturbations on top of an existing streak. Under their formulation, the secondary perturbations are found to undergo significant transient growth, driven by spanwise gradients, and artificially suppressing the spanwise gradients stunts the growth of perturbations. In other words, the push-over mechanism seems to be responsible for the transfer of energy from the streak to secondary scales, thus helping shape the structure of near-wall turbulence. In Chapter 5, where we study the breakdown of an injected "optimal" streak in a turbulent channel, we lend special attention to the role of the spanwise self-advection term in re-distributing energy across scales.

In light of the importance of linear mechanisms in wall-bounded turbulence and the success of eigenfunction methods at helping elucidate the privileged role of rolls and streaks, this work focuses on another related linear analysis method: resolvent analysis. In resolvent analysis, the Navier-Stokes equations are also written as a linear dynamical system for velocity and pressure fluctuations about a base flow. The base flow can be the laminar solution as in traditional optimal perturbation theory, but more modern implementations use the turbulent mean profile, averaged over ensembles as well as the homogeneous spatial directions—in channel flow, the streamwise and spanwise directions—and time (McKeon & Sharma, 2010). Rather than neglect the nonlinear term, we represent it as a forcing term acting on this system, along with any additional exogenous force on the system. The resolvent operator refers to the linear map between the forcing inputs and the flow states. In this linearized setting, without computing the nonlinear terms, we can solve for the input (or forcing) terms that would generate the output trajectories (or responses) with the largest kinetic energy (Jovanović & Bamieh, 2005). This is done in practice by taking a singular value decomposition (SVD) of the discretized resolvent operator. The first right singular mode—the principal forcing mode—reveals the inputs to which the linearized equations of motion are most sensitive, similar to the optimal perturbation of Butler and Farrell (1992). The first left singular mode—the principal response mode—reveals the most amplified outputs. The first singular value squared yields the kinetic energy amplification factor. The assumption underpinning this approach is that the optimal structures computed by resolvent analysis will be preferentially "selected" and amplified by the linear dynamics of the flow, thus manifesting as sustained coherent structures.

Resolvent analysis is traditionally applied to systems exhibiting spatial and temporal homogeneity. The linearized Navier-Stokes are first Fourier transformed in time and the homogeneous spatial directions prior to resolvent analysis; the method thus targets the linear amplification properties of individual wave numbers and frequencies. In the context of wall-bounded turbulent flows, the equations are Fourier-transformed in the streamwise and spanwise directions, and time, and the targeted length scales are the traditional streamwise and spanwise streak spacings in the buffer layer (Bae et al., 2021; McKeon, 2017; McKeon & Sharma, 2010; Moarref et al., 2013).

When applied to wall-bounded turbulent flows, resolvent analysis is successful at identifying streamwise rolls as the most perturbing structures, and streamwise streaks as the most amplified structures (Bae et al., 2021; McKeon & Sharma, 2010). Resolvent modes also highlight noteworthy dynamics of near-wall turbulence. The computed response modes, interpreted as waves propagating in the streamwise direction at a velocity determined by their frequency and streamwise wavelength, tend to peak in energy where their wave speed matches the mean streamwise velocity (Cui & Jacobi, 2023; McKeon, 2017; McKeon et al., 2013; Moarref et al., 2013; Toedtli et al., 2019). The most prominent modes that arise from resolvent analysis are thus consistent with Taylor's frozen turbulence hypothesis, which describes turbulent structures as propagating close to the local mean velocity (Taylor, 1938). The location where the wave speed equals the mean velocity—and where perturbations are most amplified—defines a critical layer where the resolvent operator would be singular if not for viscosity (McKeon & Sharma, 2010). This underscores the potentially significant energy amplification achievable by perturbations to the flow, especially in the critical layer. We expect such maximally amplified modes to those play a significant role in shaping the behavior and structure near-wall turbulence. Additionally, resolvent modes have been found to reflect the self-similar and universal properties of wall-bounded turbulence, inheriting them from the mean profile. Energy spectra computed using resolvent response modes exhibit two peaks, one close to the wall and one farther away which, when scaled accordingly, collapse for a wide range of Reynolds numbers (Moarref et al., 2013).

Because resolvent response modes are expected to figure prominently in turbulent flows, and given that they adhere to scaling laws that govern them, they have been fruitfully used as flow reconstruction tools. Linear combinations of the leading response modes have been used to construct low-dimensional approximations of turbulent flows, including channel and pipe flow (Ahmed et al., 2021; Arun et al., 2023; Bae et al., 2020a, 2020b; Beneddine et al., 2017; Gómez et al., 2016; Illingworth et al., 2018; Moarref et al., 2013). Using resolvent modes to model flows is especially tractable when the singular values of the resolvent operator decay quickly, meaning that only a small handful need be computed to capture the effects of linear amplification. The weighting coefficients are often trained on DNS data and serve to capture the nonlinearly determined distribution of forcing contributions on different length scales (Moarref et al., 2013). Other works have also explored the use of resolvent modes in estimating and predicting flows with sparse measurements. Specifically, a low-rank approximation of the resolvent operator can be used to model correlations between different spatial locations of the flow (Martini et al., 2020; Towne et al., 2020).

Resolvent modes are descriptive enough to be used for the purpose of reconstruction and estimation. They also carry a physical relevance, and can be used as dynamical models of turbulent flows. In Toedtli et al. (2019), resolvent modes are used to model the response of turbulent channel flow to a varying-phase opposition control. The resolvent model captures the change in the profiles and drag well despite discrepancies in the predicted stress profile between the model and DNS. To control turbulent flows, cheaply computed resolvent modes can be used in lieu of expensive DNS to design forcing functions. Liu et al. (2021) apply this framework to reduce pressure fluctuations along a cavity in supersonic flow. Yeh and Taira (2019) uses the resolvent analysis of a flow over an airfoil to identify a forcing frequency and length scale that enhance momentum mixing and reduce flow separation. Lin et al. (2023) repeat this method for a plunging cylinder to reduce lift fluctuations.

The assumption underpinning the above control design framework is that resolvent modes, though only optimal for the linearized equations, nevertheless capture fundamental mechanisms of energy transfer, even within fully turbulent flows. Works like Bae et al. (2021) lend credibility to this assumption, and resolvent modes are indeed found to play a role in the transfer of energy to coherent near-wall turbulent perturbations. In a modified DNS, subtracting the contribution of the principal resolvent forcing mode from the nonlinear term at every time step interrupts the streak-regeneration process. Consequently, buffer layer turbulence is greatly suppressed. Resolvent forcing and response modes show promise in emulating the behavior of turbulent flows under forcing, and this is linked to the role the forcing modes themselves play in amplifying near-wall turbulence in simulated flows.

The traditional formulation of the resolvent operator relies on Fourier-transforming the linearized Navier-Stokes equations in time. This restricts its formulation to statistically steady and quasiperiodic flows. The resulting SVD modes will be Fourier modes in time, and cannot represent temporally local effects, be it for the purpose of analysis, reconstruction, or control. Indeed, we remind the reader that certain mechanisms vital to near-wall turbulence—such as the Orr mechanism—are transient, and a mean flow that varies in time can have a significant impact on the turbulence. Traditional Fourier-based resolvent analysis is not easily adaptable to these flow configurations and has thus not been used to study them. In the context of flow control and estimation, the time horizon of the influence of resolvent modes on the flow is also important. To improve the estimation capabilities of resolvent modes, Martini et al. (2020) re-weight the resolvent operator to reflect temporal statistics. When applying resolvent analysis to the control of flow separation over an airfoil, Yeh and Taira (2019) modify the resolvent operator using the exponential discounting method introduced in Jovanovic (2004) to select forcing and responses modes acting on a time scale of interest. Indeed, in more physical scenarios, the flow would only be forced intermittently, either by spontaneous events arising in the unforced flow or by externally imposed actuation, and it would be valuable to study how a turbulent flow instantaneously reacts to such forcing.

Given the value of this property to analysis, estimation and control, we dedicate this work to the formulation of resolvent modes capable of encoding time. Rather than construct our resolvent modes using Fourier modes in time, we propose using wavelets. In practice, we wavelet-transform the linearized fluctuation equations in time before constructing the resolvent operator. Wavelets are similar to Fourier modes in that they can be used to represent square-integrable functions. What makes wavelets suited to our goal, however, is the fact that their mass is concentrated in particular time interval; integrating against a wavelet thus captures information centered in its support. The wavelet expansion of a function of time involves projecting the function on both re-scaled (as in the Fourier case) and shifted versions of a mother wavelet (Mallat, 1999). The wavelet transform is thus a function of the time shift and the scaling coefficient, allowing it to explicitly represent time and frequency information simultaneously. The wavelet transform and the formulation of the wavelet-based operator are the subject of Chapter 3. Wavelet-based resolvent modes with their additional time and frequency localization allow them to reflect the influence of a time-varying mean profile, or capture transient events.

This novel formulation allows us to obtain optimally amplified transient trajectories, whose temporally and spatially integrated kinetic energy is maximized. Though seemingly similar to optimal perturbation theory, we note that the two methods use different measures of optimality. Optimal perturbation theory indeed maximizes the kinetic energy ratio between the initial condition and the solution at the chosen terminal time, while the wavelet-based resolvent analysis maximizes the integrated kinetic energy of the response over the entire time domain. We argue in Chapter 4.1 that the latter captures structures that tend to persist in time, rather than spike and decay rapidly. Moreover, wavelet-based resolvent analysis does not prescribe the instance of the initial perturbation, which, in optimal transient growth theory, is defined to be at the time origin. The optimal wavelet-based forcing mode can appear any instance of the time domain: for example, when applied to turbulent oscillating Stokes flows (Ballouz, Lopez-Doriga, et al., 2024; Ballouz et al., 2023), the computed forcing and response modes coincide with the times in the cycle when the streamwise root-mean-square velocity peaks. As will be seen throughout this work, transient forcing modes usually precede their corresponding response mode, which suggests that time-localized resolvent analysis correctly extracts causal relations between the forcing and response structures.

The wavelet-based modes allow us to analyze both non-equilibrium effects of a time-varying mean flow, or transiently amplified perturbations. Given that resolvent modes are often used as surrogates of turbulent flows, or as ways to actuate and control these flows, we are also interested in the limitations of these applications. The transient growth of any linearly "optimal" structure within a fully turbulent flow is modulated by the myriad nonlinear interactions not considered upon the computation of the mode. With the objective of controlling near-wall turbulence in mind, a problem that interests us is whether significant transient growth can still be achieved in a turbulent flow. We can test this using similar methods as Bae et al. (2021)—that is, by running a modified DNS of a turbulent channel in which we inject a time-localized resolvent forcing mode. By comparing the results to the transient resolvent response corresponding to the injected forcing, we can measure the interactions of the developing "optimal" response—no longer optimal in this case—with the background turbulence of the system. In addition to its value to control, such an experiment also reveals insights on the streak breakdown process, paving the way to future research projects that investigate another step of the self-sustaining process.

Thesis outline

Chapter 2 covers the mathematical formulation of Fourier based resolvent analysis methods. These rely on equations that have been Fourier-transformed in time and are applicable to flows with either a constant or time-periodic base flow. The Fourier-based methods are the backbone of the extension we develop, wavelet-based resolvent analysis, which we discuss in Chapter 3. The chapter also addresses issues of efficiency and convergence, and validates the method against the Fourier-based ones. In Chapter 4.1, we explore a novel application of resolvent analysis, one that requires the wavelet-based formulation: Orr bursts in channel flow, a transient phenomenon argued to play a key role in sustaining wall-bounded turbulence. Another novel application involving a non-periodic time-varying base flow is explored in Chapter 4.2. We study the linear amplification of perturbations in turbulent channel flow that has been subjected to a sudden and sustained spanwise pressure gradient. In Chapter 5, we test the effectiveness of resolvent modes at actuating a turbulent system and capturing its response to actuation. We inject a time-localized wavelet-based resolvent forcing mode into a DNS of the minimal flow unit, and track the growth and decay of the induced streak. Special attention is given to the nonlinear interactions that lead to the breakdown of the mode. We conclude the dissertation in Chapter 6, and propose new research topics of near-wall turbulence that make use of wavelet-based resolvent analysis.

Chapter 2

BACKGROUND: FOURIER-BASED RESOLVENT ANALYSIS

This chapter concerns the formulation of Fourier-based methods of resolvent analysis, in which the equations of motions are Fourier-transformed in time. Traditional resolvent analysis (Chapter 2.1) targets the linear amplification of a perturbation traveling at a single wave speed. This formulation has the longer history, and we reproduce some of its key results for turbulent channel flow. Harmonic resolvent analysis (Chapter 2.2) extends the method to oscillating flows, and considers a handful of interacting perturbation frequencies.

2.1 Traditional resolvent analysis

This section outlines the traditional formulation of resolvent analysis, *i.e.* its most common formulation prior to 2020. For the rest of this work, we assume that our fluid of interest is governed by the incompressible Navier-Stokes equations, though works like Bae et al. (2020b) and Gomez et al. (2022) have also formulated resolvent analysis for the compressible equations.

Formulation

As in other linear analysis methods, the subjects of resolvent analysis are the velocity and pressure fluctuations about a mean profile. Consider $\bar{u}_i$, the total velocity in the x_i direction, and $\bar{p}$, the total pressure. These quantities include both the mean and fluctuating components. Suppose the velocities in all directions are non-dimensionalized with a reference velocity u^*, the length scales with a reference length L^*, and pressure with a reference density ρ^*. Suppose time is correspondingly non-dimensionalized using u^* and L^*. The nondimensional flow quantities obey the incompressible Navier-Stokes equations:

$$\frac{\partial \bar{u}_i}{\partial t} + \bar{u}_j \frac{\partial \bar{u}_i}{\partial x_j} = -\frac{\partial \bar{p}}{\partial x_i} + \frac{1}{Re} \frac{\partial^2 \bar{u}_i}{\partial x_j \partial x_j}, \quad \frac{\partial \bar{u}_i}{\partial x_i} = 0, \tag{2.1}$$

where $Re = u^* L^* / \nu^*$ is the Reynolds number, with ν^* being the kinematic viscosity. The fluctuations are defined with respect to the total velocity: $u_i := \bar{u}_i - U_i$ and $p := \bar{p} - P$, where $U_i := \langle \bar{u}_i \rangle$ and $P := \langle \bar{p} \rangle$ denote the mean velocity and pressure profiles, respectively, and the brackets $\langle \cdot \rangle$ denote the averaging operation. The averaging is often done in the directions of homogeneity, and thus depends on the symmetry of the analyzed fluidic system. For example, for channel flow, the mean profiles are traditionally obtained by averaging the solution from simulations over the streamwise and spanwise spatial directions and time.

By expressing $\bar{u}_i$ and $\bar{p}$ as a sum of the fluctuating and mean component, we can split equations (2.1) into coupled equations for the mean and the fluctuations:

$$\frac{\partial U_i}{\partial t} + \left\langle \bar{u}_j \frac{\partial \bar{u}_i}{\partial x_j} \right\rangle = -\frac{\partial P}{\partial x_i} + \frac{1}{Re}\frac{\partial^2 U_i}{\partial x_j \partial x_j}, \qquad \frac{\partial U_i}{\partial x_i} = 0, \tag{2.2}$$

$$\frac{\partial u_i}{\partial t} + U_j \frac{\partial u_i}{\partial x_j} + u_j \frac{\partial U_i}{\partial x_j} = -\frac{\partial p}{\partial x_i} + \frac{1}{Re}\frac{\partial^2 u_i}{\partial x_j \partial x_j} + f_i, \qquad \frac{\partial u_i}{\partial x_i} = 0. \tag{2.3}$$

We use f_i to denote the nonlinear terms in the fluctuating equations. The equations above do not have an analytic solution unless in particular situations and are most commonly solved numerically. In resolvent analysis, we do not seek exact solutions to the above system. Only the equations for the fluctuations are considered and the mean profile is assumed to be an invariant parameter independent of the fluctuations. Moreover, in contrast to optimal linear growth, the nonlinear terms f_i are not ignored, but instead modeled as forcing functions applied exogenously onto the fluctuating system. In other words, resolvent analysis assumes that f_i is independent of u_i and p. The goal of resolvent analysis is to formulate a linear mapping between the nonlinearities and the fluctuation field. We note that some of the terms in the fluctuating equations may be zero depending on the flow configuration. For channel flow, which is homogeneous in the streamwise (x_1) and spanwise (x_3) directions, $U_2 = U_3 = 0$ and $\partial U_1/\partial x_1 = \partial U_1/\partial x_3 = 0$.

In traditional resolvent analysis, the fluctuations are assumed to be periodic in the homogeneous directions, and equations (2.3) are Fourier-transformed in those spatial directions. Moreover, the mean flow is statistically stationary and therefore independent of time; the fluctuation equations are assumed to be periodic in time and further Fourier-transformed in time. After applying the aforementioned Fourier transformations, the equations for the fluctuations are discretized over the non-homogeneous spatial dimensions of the grid and we obtain the following:

$$\widehat{\boldsymbol{D}_t}\widehat{\boldsymbol{u}}_i + \widehat{\boldsymbol{u}}_j \boldsymbol{dU}_{i,j} + \boldsymbol{U}_j \widehat{\boldsymbol{D}_j}\widehat{\boldsymbol{u}}_i = -\widehat{\boldsymbol{D}}_i\widehat{\boldsymbol{p}} + \frac{1}{Re}\widehat{\boldsymbol{L}}\widehat{\boldsymbol{u}}_i + \widehat{\boldsymbol{f}}_i, \qquad \widehat{\boldsymbol{D}}_i\widehat{\boldsymbol{u}}_i = 0, \tag{2.4}$$

where $\widehat{\boldsymbol{u}}_i$, $\widehat{\boldsymbol{f}}_i$ and $\widehat{\boldsymbol{p}}$ respectively denote the transformed and discretized u_i, f_i, and p, $\widehat{\boldsymbol{D}_t}$ and $\widehat{\boldsymbol{D}_i}$ are the transformed discrete differentiation operators in time and the x_i– directions respectively, and $\widehat{\boldsymbol{L}}$ is the transformed Laplacian. For systems that are homogeneous in the streamwise and spanwise directions and periodic in time, we can write $\widehat{\boldsymbol{D}_t} = -\mathrm{i}\omega$, $\widehat{\boldsymbol{D}_1} = \mathrm{i}k_1$, $\widehat{\boldsymbol{D}_3} = \mathrm{i}k_3$, $\widehat{\boldsymbol{D}_2} = \boldsymbol{D}_2$, and $\widehat{\boldsymbol{L}} = -k_1^2 + \boldsymbol{D}_2^2 - k_3^2$, where ω is the chosen frequency for the temporal Fourier transform, (k_1, k_3) are the streamwise and spanwise wavenumber pair, and $\boldsymbol{D}_2$ is the discrete derivative in the x_2–direction. We use $\boldsymbol{U}_i$ and $\boldsymbol{dU}_{i,j}$ to denote the diagonal matrices whose diagonal terms are respectively U_i and $\partial U_i/\partial x_j$ evaluated at the grid points, and we note that since the system is homogeneous in x_1 and x_3, $\boldsymbol{U}_2 = \boldsymbol{U}_3 = \boldsymbol{dU}_{i,1} = \boldsymbol{dU}_{i,3} = \mathbf{0}$. Each of the discretized momentum and continuity equations is an N_2-dimensional system, where N_2 is the spatial resolution in the x_2 direction. These linearized equations can then be cast as

$$\begin{bmatrix} \hat{\boldsymbol{u}}_1(x_2) \\ \hat{\boldsymbol{u}}_2(x_2) \\ \hat{\boldsymbol{u}}_3(x_2) \\ \hat{\boldsymbol{p}}(x_2) \end{bmatrix} = \widehat{\boldsymbol{H}}^{(k_1,k_3,\omega)} \begin{bmatrix} \hat{\boldsymbol{f}}_1(x_2) \\ \hat{\boldsymbol{f}}_2(x_2) \\ \hat{\boldsymbol{f}}_3(x_2) \\ \mathbf{0} \end{bmatrix}, \tag{2.5}$$

where $\widehat{\boldsymbol{H}}^{(k_1,k_3,\omega)}$ denotes the traditional Fourier-based resolvent operator

$$\widehat{\boldsymbol{H}}^{(k_1,k_3,\omega)} = \left[\left(-\mathrm{i}\omega\boldsymbol{I} - \frac{1}{Re}\boldsymbol{L} + \mathrm{i}k_1\boldsymbol{U}_1 + \boldsymbol{U}_2\boldsymbol{D}_2 + \mathrm{i}k_3\boldsymbol{U}_3 \right) \begin{pmatrix} \boldsymbol{I} & \mathbf{0} & \mathbf{0} & \mathbf{0} \\ \mathbf{0} & \boldsymbol{I} & \mathbf{0} & \mathbf{0} \\ \mathbf{0} & \mathbf{0} & \boldsymbol{I} & \mathbf{0} \\ \mathbf{0} & \mathbf{0} & \mathbf{0} & \mathbf{0} \end{pmatrix} + \begin{pmatrix} \mathbf{0} & \widehat{\boldsymbol{dU}}_{1,2} & \mathbf{0} & \mathrm{i}k_1\boldsymbol{I} \\ \mathbf{0} & \widehat{\boldsymbol{dU}}_{2,2} & \mathbf{0} & \boldsymbol{D}_2 \\ \mathbf{0} & \widehat{\boldsymbol{dU}}_{3,2} & \mathbf{0} & \mathrm{i}k_3\boldsymbol{I} \\ \mathrm{i}k_1\boldsymbol{I} & \boldsymbol{D}_2 & \mathrm{i}k_3\boldsymbol{I} & \mathbf{0} \end{pmatrix} \right]^{-1}, \tag{2.6}$$

and the superscript (k_1, k_3, ω) indicates the choice of streamwise and spanwise wavenumbers k_1 and k_3, and frequency ω used in the Fourier transforms. The functional dependence on x_2 indicates the discretisation over the wall-normal spatial dimension.

The analysis of the resolvent operator $\widehat{\boldsymbol{H}}^{(k_1,k_3,\omega)} \in \mathbb{C}^{4N_2} \times \mathbb{C}^{4N_2}$ consists of taking its singular value decomposition (SVD). Before taking the SVD of $\widehat{\boldsymbol{H}}^{(k_1,k_3,\omega)}$, an additional weighting step is performed so that the first right singular vector maximizes a norm of interest, traditionally the kinetic energy seminorm (Jovanović & Bamieh, 2005; McKeon, 2017; McKeon & Sharma, 2010). Specifically, an SVD is performed on the following matrix:

$$\begin{pmatrix} \boldsymbol{dX_2} & \mathbf{0} & \mathbf{0} & \mathbf{0} \\ \mathbf{0} & \boldsymbol{dX_2} & \mathbf{0} & \mathbf{0} \\ \mathbf{0} & \mathbf{0} & \boldsymbol{dX_2} & \mathbf{0} \\ \mathbf{0} & \mathbf{0} & \mathbf{0} & \mathbf{0} \end{pmatrix} \widehat{\boldsymbol{H}}^{(k_1,k_3,\omega)} \begin{pmatrix} \boldsymbol{dX_2^{-1}} & \mathbf{0} & \mathbf{0} & \mathbf{0} \\ \mathbf{0} & \boldsymbol{dX_2^{-1}} & \mathbf{0} & \mathbf{0} \\ \mathbf{0} & \mathbf{0} & \boldsymbol{dX_2^{-1}} & \mathbf{0} \\ \mathbf{0} & \mathbf{0} & \mathbf{0} & \mathbf{0} \end{pmatrix}, \tag{2.7}$$

where the elements of the diagonal matrix $\boldsymbol{dX_2}$ are the integration weights at each grid point. For a uniform grid, $\boldsymbol{dX_2} = \boldsymbol{I}$ can be used. The SVD enables us to solve the following optimization problem:

$$\begin{aligned} &\max_{\widehat{f}_1,\, \widehat{f}_2,\, \widehat{f}_3} \left\{ [\widehat{\boldsymbol{u}}_1] + [\widehat{\boldsymbol{u}}_2] + [\widehat{\boldsymbol{u}}_3] \right\} \\ &\text{subject to} [\widehat{\boldsymbol{f}}_1] + [\widehat{\boldsymbol{f}}_2] + [\widehat{\boldsymbol{f}}_3] = 1 \text{ and equation (2.6),} \end{aligned} \tag{2.8}$$

where, for a wall-normal spatial domain $[0, L_2]$, we use $[\cdot] = \frac{1}{L_2}\int_0^{L_2} |\cdot|^2 dx_2$ to denote the x_2-integrated energy. The solution to (2.8) is the largest singular value squared σ_1^2.

The left and right singular vectors are interpreted as response and forcing modes, respectively, and the singular values as amplification factors or gains. The principal forcing mode, *i.e.* the right singular vector corresponding to σ_1, is the forcing which produces the velocity fluctuations with the largest kinetic energy via the linearized system. This mode is often interpreted as the most effective at perturbing the linearized system. The principal response mode, *i.e.* the left singular vector corresponding to σ_1, reveals the structure of the most amplified velocity and pressure fluctuation field. We denote the principal forcing and response modes by $\hat{\boldsymbol{\phi}}(x_2) = [\hat{\boldsymbol{\phi}}_1^T, \hat{\boldsymbol{\phi}}_2^T, \hat{\boldsymbol{\phi}}_3^T, \mathbf{0}^T]^T$ and $\hat{\boldsymbol{\psi}}(x_2) = [\hat{\boldsymbol{\psi}}_1^T, \hat{\boldsymbol{\psi}}_2^T, \hat{\boldsymbol{\psi}}_3^T, \hat{\boldsymbol{\psi}}_p^T]^T$ respectively. The modes are normalized such that their integrated kinetic energy satisfies

$$[\hat{\phi}_1] + [\hat{\phi}_2] + [\hat{\phi}_3] = 1, \tag{2.9}$$

$$[\hat{\psi}_1] + [\hat{\psi}_2] + [\hat{\psi}_3] = 1. \tag{2.10}$$

Application to turbulent channel flow

Let us now apply this method to turbulent channel flow and reproduce the modes obtained in McKeon and Sharma (2010) and Moarref et al. (2013) in order to highlight some of their properties. In particular, the modes inherit certain symmetries from the geometry of the domain. Moreover, the principal forcing modes appear in the form of streamwise rolls, while the principal response modes appear as streamwise streaks, *i.e.* regions of alternating positive and negative velocity anomalies elongated in the streamwise direction. The most amplified modes tend to peak at the critical layer, defined as the wall-normal height where the mode's wave speed matches the mean streamwise velocity.

For what follows, the length scales are non-dimensionalized by the channel half-height δ^* and velocity scales by the friction velocity u_τ^* so that $Re = Re_\tau$. For the mean velocity profile, we use that of a turbulent channel flow at friction Reynolds $Re_\tau = 186$, obtained from the DNS conducted in Bae and Lee (2021). The DNS uses a second-order staggered finite-difference (Orlandi, 2000) and a fractional-step method (J. Kim & Moin, 1985) with a third-order Runge-Kutta time-advancing scheme (Wray, 1990). Periodic boundary conditions are imposed in the streamwise and spanwise directions; no-slip and no-penetration boundary conditions are imposed at the top and bottom walls. The simulation code has been validated in previous studies in turbulent channel flows (Bae et al., 2018, 2019; Lozano-Durán & Bae, 2019) and flat-plate boundary layers (Lozano-Durán et al., 2018). The dimensions of the numerical domain are $L_1 = 8\pi$, $L_2 = 2$, and $L_3 = 3\pi$ in the streamwise, wall-normal, and spanwise directions, respectively. We use uniform grids in the streamwise and spanwise directions of size $N_1 = 768$ and $N_3 = 288$, respectively, such that the grid spacing is $\Delta x_1^+ = \Delta x_3^+ = 6$. The $N_2 = 130$ wall-normal grid points are distributed according to a hyperbolic tangent profile, such that $\min(\Delta x_2^+) = 0.16$ near the wall and $\max(\Delta x_2^+) = 7.2$ near the centerline. Here, the superscript $(\cdot)^+$ denotes wall units defined for length scales as $(\cdot)^+ = (\cdot)Re_\tau$. The simulations were run for an additional $t = 100$ after transients in order to compute U_1 and dU_1/dx_2 by averaging the results in the streamwise and spanwise directions, and time.

Equation (2.4) is discretized on a Chebyshev grid of size $N_2 = 128$; $\boldsymbol{U}_1$ and $\boldsymbol{dU}_{1,2}$ are projected onto the grid points by interpolation. The discrete differentiation operators $\boldsymbol{D}_2$ and $\boldsymbol{D}_2^2$ are pseudospectral Chebyshev derivative matrices (Trefethen, 2000; Weideman & Reddy, 2000). These derivatives are dense, but we find that the resolvent modes converge for our small grid size—that is, they do not change if we increase N_2 further. For much larger N_2, the use of sparse matrices becomes essential for a tractable computation. We choose to target the near-wall streaks, which, for $Re_\tau = 186$, are spaced according to $\lambda_1^+ \approx 1000$ and $\lambda_3^+ \approx 100$ (Bae et al., 2021; Moarref et al., 2013). These length scales also correspond to the peaks in the streamwise spectrum. We choose the frequency ω which produces the largest linear amplification σ_1; this corresponds to $\omega = 17.14$.

Because of the symmetry about the centerline, resolvent analysis of channel flows produces pairs of equivalent modes. In Figure 2.1 (a), the singular values indeed

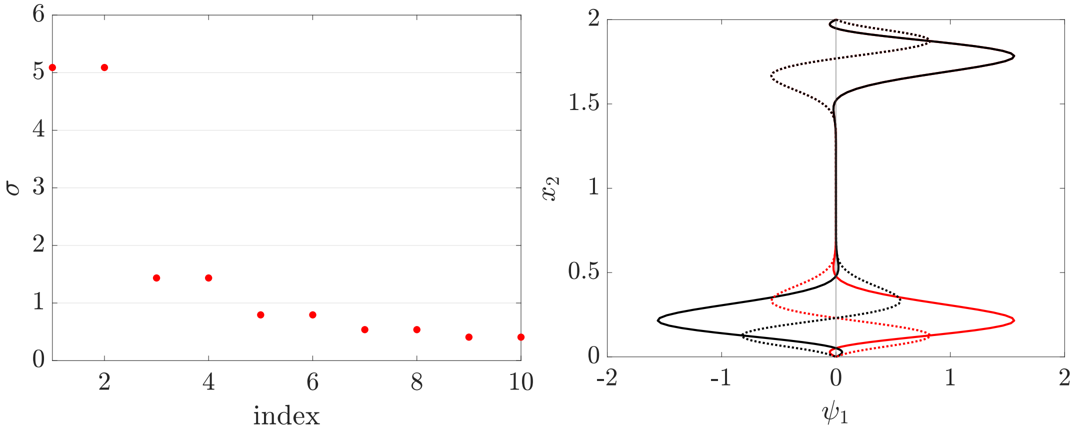

(a) (b)

Figure 2.1: (a) First ten singular values from Fourier-based resolvent analysis of channel flow at $Re_\tau = 186$; (b) principal (black) and second (red) response modes. Solid lines represent the real part of the respective modes, while dotted lines represent the imaginary part. We note that in the top half of the channel, the modes are identical and only the principal one is visible. The Fourier parameters used are $(\lambda_1^+, \lambda_3^+, \omega) = (1000, 100, 17.14)$, and the vertical black line is the zero-velocity reference line.

occur in near-equal pairs; the corresponding forcing modes thus generate equally amplified response modes. For the bottom half of the channel, the modes corresponding to the first two singular values are identical; for the top half, they are opposite (Figure 2.1 (b)). The modes form a two-dimensional singular plane, for which we can construct the following convenient basis vectors: the first, proportional to the sum of the modes, captures the response in the bottom half of the channel, and the second, proportional to their difference, captures the response in the top.

To construct the modes in physical space, we take into account this symmetry. Consider a velocity vector $\hat{\boldsymbol{u}}^{(k_1,k_3,\omega)} = (\hat{u}_1^{(k_1,k_3,\omega)}, \hat{u}_2^{(k_1,k_3,\omega)}, \hat{u}_3^{(k_1,k_3,\omega)}, \hat{p}^{(k_1,k_3,\omega)})$ and a forcing vector $\hat{\boldsymbol{f}}^{(k_1,k_3,\omega)} = (\hat{f}_1^{(k_1,k_3,\omega)}, \hat{f}_2^{(k_1,k_3,\omega)}, \hat{f}_3^{(k_1,k_3,\omega)}, 0)$ that satisfy the linearized and transformed equations (2.3), where the dependence on Fourier parameters (k_1, k_3, ω) are marked explicitly. Because $U_2 = U_3 = 0$ and $dU_1/dx_1 = dU_1/dx_3 = 0$, another solution pair is formed by $\hat{\boldsymbol{u}}^{(k_1,-k_3,\omega)} = (\hat{u}_1^{(k_1,-k_3,\omega)}, \hat{u}_2^{(k_1,-k_3,\omega)}, -\hat{u}_3^{(k_1,-k_3,\omega)}, \hat{p}^{(k_1,-k_3,\omega)})$ and $\hat{\boldsymbol{f}}^{(k_1,k_3,\omega)} = (\hat{f}_1^{(k_1,-k_3,\omega)}, \hat{f}_2^{(k_1,-k_3,\omega)}, -\hat{f}_3^{(k_1,-k_3,\omega)}, 0)$.

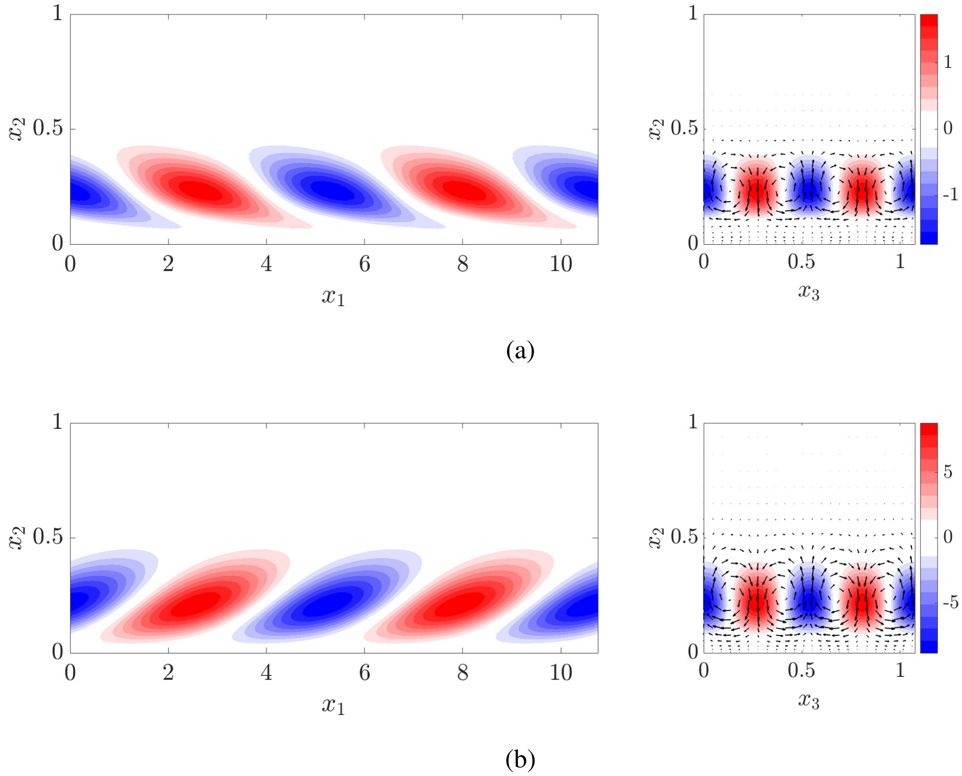

(a)

(b)

Figure 2.2: Principal resolvent (a) forcing and (b) response modes for channel flow at $Re_\tau = 186$, using $(\lambda_1^+, \lambda_3^+, \omega) = (1000, 100, 17.14)$. The modes have been inverse-Fourier transformed in the streamwise and spanwise directions and are plotted in physical space at $x_1 = 0$ and $x_3 = 0$. The contours represent the streamwise component and the black arrows represent the direction of the cross-flow components.

Thus, the resolvent modes in physical space are constructed as

$$\psi_1(x_1, x_2, x_3, t) = 2\mathfrak{Re}\left\{\hat{\psi}_1(x_2)e^{\mathrm{i}k_1x_1+\mathrm{i}k_3x_3-\mathrm{i}\omega t} + \hat{\psi}_1(x_2)e^{\mathrm{i}k_1x_1-\mathrm{i}k_3x_3-\mathrm{i}\omega t}\right\}, \quad (2.11)$$

$$\psi_2(x_1, x_2, x_3, t) = 2\mathfrak{Re}\left\{\hat{\psi}_2(x_2)e^{\mathrm{i}k_1x_1+\mathrm{i}k_3x_3-\mathrm{i}\omega t} + \hat{\psi}_2(x_2)e^{\mathrm{i}k_1x_1-\mathrm{i}k_3x_3-\mathrm{i}\omega t}\right\}, \quad (2.12)$$

$$\psi_3(x_1, x_2, x_3, t) = 2\mathfrak{Re}\left\{\hat{\psi}_3(x_2)e^{\mathrm{i}k_1x_1+\mathrm{i}k_3x_3-\mathrm{i}\omega t} - \hat{\psi}_3(x_2)e^{\mathrm{i}k_1x_1-\mathrm{i}k_3x_3-\mathrm{i}\omega t}\right\}, \quad (2.13)$$

$$\psi_p(x_1, x_2, x_3, t) = 2\mathfrak{Re}\left\{\hat{\psi}_p(x_2)e^{\mathrm{i}k_1x_1+\mathrm{i}k_3x_3-\mathrm{i}\omega t} + \hat{\psi}_p(x_2)e^{\mathrm{i}k_1x_1-\mathrm{i}k_3x_3-\mathrm{i}\omega t}\right\}, \quad (2.14)$$

and

$$\phi_1(x_1, x_2, x_3, t) = 2\mathfrak{Re}\left\{\hat{\phi}_1(x_2)e^{\mathrm{i}k_1x_1+\mathrm{i}k_3x_3-\mathrm{i}\omega t} + \hat{\phi}_1(x_2)e^{\mathrm{i}k_1x_1-\mathrm{i}k_3x_3-\mathrm{i}\omega t}\right\}, \quad (2.15)$$

$$\phi_2(x_1, x_2, x_3, t) = 2\mathfrak{Re}\left\{\hat{\phi}_2(x_2)e^{\mathrm{i}k_1x_1+\mathrm{i}k_3x_3-\mathrm{i}\omega t} + \hat{\phi}_2(x_2)e^{\mathrm{i}k_1x_1-\mathrm{i}k_3x_3-\mathrm{i}\omega t}\right\}, \quad (2.16)$$

$$\phi_3(x_1, x_2, x_3, t) = 2\mathfrak{Re}\left\{\hat{\phi}_3(x_2)e^{\mathrm{i}k_1x_1+\mathrm{i}k_3x_3-\mathrm{i}\omega t} - \hat{\phi}_3(x_2)e^{\mathrm{i}k_1x_1-\mathrm{i}k_3x_3-\mathrm{i}\omega t}\right\}, \quad (2.17)$$

where, $\mathfrak{Re}(\cdot)$ denotes the real component. The modes are similar in shape to those in Moarref et al. (2013)—computed for channel flow at $Re_\tau = 10,000$ using

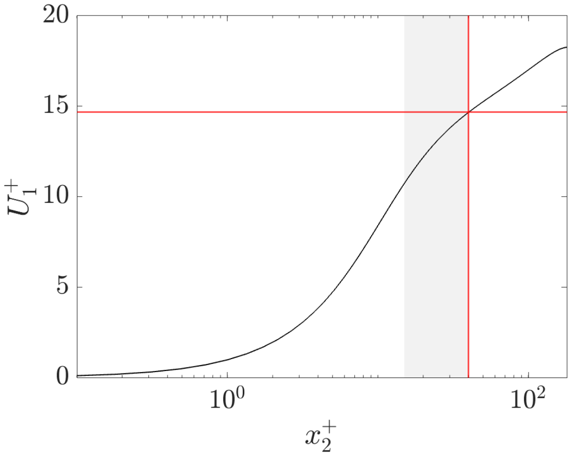

Figure 2.3: Mean channel flow velocity profile $U_1(x_2^+)$ for $Re_\tau = 186$. The vertical red line indicates the location of the peak in $|\hat{\psi}_1|$—the magnitude of the streamwise component of the principal resolvent mode. The horizontal red line indicates the wave speed $c^+ = \omega/k_1 = 14.66$. The shaded region delimits the buffer layer ($15 \leq x_2^+ \leq 40$).

the Cess model for the channel profile (Cess, 1958; Malkus, 1956; Reynolds & Tiederman, 1967)—and McKeon and Sharma (2010)—computed for turbulent pipe flow using an experimentally obtained mean profile. For the principal forcing mode (Figure 2.2(a)), the spanwise and wall-normal components dominate the streamwise one by roughly an order of magnitude. The streamwise perturbations appear as backward-tilted regions elongated in the streamwise direction, and alternate between negative and positive anomalies. These are interspersed with vortical rolls formed by the spanwise and wall-normal components that rotate about the streamwise axis, alternating between the clockwise and anticlockwise directions. The response is structured similarly (Figure 2.2(b)), except that the predominant component is the streamwise one, and the streamwise streaks are forward-tilted. The rolls are roughly an order of magnitude weaker than the streaks.

In addition to having a common shape, these resolvent modes highlight dynamics believed to be responsible for the amplification of perturbations in shear flows. Rolls sweep slow fluid close to the wall (or fast fluid farther away) into the faster (or, respectively, slower) streamwise mean flow above (below) it, which accelerates (or decelerates) it in the streamwise direction (Hwang & Cossu, 2010). Therefore, rolls are believed to be an efficient way of amplifying velocity perturbations, to which resolvent analysis lends support by yielding streamwise rolls as the optimal forcing structure and streamwise streaks as their corresponding response. Moreover, the backward-tilting rolls leading to forward-tilting have been interpreted as indicative of the Orr mechanism (Pickering et al., 2020), another proposed mechanism for efficiently amplifying velocity perturbations (Jiménez, 2013, 2015). More on the Orr mechanism can be found in Chapter 4.1.

Another important property of the computed near-wall modes is that they peak in magnitude at the wall-normal height where their wave speed $c = \omega/k_1$ is equal to the mean streamwise velocity profile (Figure 2.3). This property, described in McKeon (2017, 2019), McKeon and Sharma (2010), and Schmid et al. (2002), allows us to define a critical layer, *i.e.* a region where significant energy amplification can occur by causing the resolvent operator to become near-singular, or even singular in the inviscid limit (or as $Re_\tau \to \infty$), in which case the linear amplification is unbounded. In this region, we expect the flow to be particularly sensitive to perturbations and the linear modes to play a larger role in determining and modeling the behavior of turbulence. One discrepancy we observe outright, however, is that our velocity modes peak slightly above the wall-normal height of $x_2^+ = 15$ associated with high-intensity turbulence in the buffer layer. The inclusion of eddy viscosity in the linearized Navier-Stokes equations remedies this mismatch somewhat (Symon et al., 2023), and causes the modes to peak closer to $x_2^+ = 15$. Accounting for nonlinear effects is therefore important for improving the quantitative accuracy of resolvent-based models of turbulence. For the purpose of analysis, much insight can be gleaned from studying individual resolvent modes. This is emphasized throughout this work, the purpose of which is not to model turbulence accurately, but rather to understand fundamental behaviors of turbulence.

2.2 Harmonic resolvent analysis

Fourier-based resolvent analysis—that is, resolvent analysis that is formulated after the equations governing the velocity fluctuations are Fourier-transformed in time—has been extended to flows where the mean profile is periodic in time (Padovan & Rowley, 2022; Padovan et al., 2020). In such a case, the equations (2.3) can still be Fourier-transformed in time, but additional terms pertaining to the interaction of other time scales with the oscillating mean flow must be taken into account. A resolvent operator can be constructed which, in addition to mapping a forcing vector at a particular frequency to its response at the same frequency, also captures the coupling between different frequencies that is enabled by the time-varying mean. In this section, we expound on this extension, dubbed "harmonic resolvent analysis".

In harmonic resolvent analysis, the construction of the resolvent operator proceeds similarly as in Chapter 2.1 and equations (2.3) are Fourier-transformed in the homogeneous spatial directions and time. Because the mean and shear profiles are periodic in time but not necessarily constant, the transformed and discretized equations are instead

$$\begin{aligned} \widehat{\boldsymbol{D}_t}^{(\omega)} \widehat{\boldsymbol{u}}_i^{(\omega)} + \sum_{\omega'\in\Omega} \widehat{\boldsymbol{u}}_j^{(\omega')} \widehat{\boldsymbol{dU}}_{i,j}^{(\omega-\omega')} + \sum_{\omega'\in\Omega} \widehat{\boldsymbol{U}_j}^{(\omega-\omega')} \widehat{\boldsymbol{D}}_j \widehat{\boldsymbol{u}}_i^{(\omega')} &= -\widehat{\boldsymbol{D}}_i \widehat{\boldsymbol{p}}^{(\omega)} + \frac{1}{Re} \widehat{\boldsymbol{L}} \widehat{\boldsymbol{u}}_i^{(\omega)} + \widehat{\boldsymbol{f}}_i^{(\omega)}, \\ \widehat{\boldsymbol{D}}_i \widehat{\boldsymbol{u}}_i^{(\omega)} &= 0. \end{aligned} \tag{2.18}$$

In the equation above, all quantities have been Fourier-transformed in the homogeneous spatial directions and time, and discretized over the remaining spatial directions. The superscript above vectors marks the frequency used for the Fourier transform in time: $\widehat{\boldsymbol{u}_i}^{(\omega)}$, $\widehat{\boldsymbol{p}}^{(\omega)}$, and $\widehat{\boldsymbol{f}_i}^{(\omega)}$ correspond to a target frequency ω, while $\widehat{\boldsymbol{u}_i}^{(\omega')}$ correspond to a frequency ω'. We denote the time-Fourier transforms of the mean velocity and shear profiles U_i and dU_i/dx_j by $\widehat{U_i}^{(\omega')}$ and $\widehat{dU_i/dx_j}^{(\omega')}$, respectively, with the superscript $(\cdot)^{(\omega')}$ marking the frequency used in the transformation. Matrices $\widehat{\boldsymbol{U}_j}^{(\omega')}$ and $\widehat{\boldsymbol{dU}}_{i,j}^{(\omega')}$ are diagonal matrices whose elements are $\widehat{U_j}^{(\omega')}$ and $\widehat{dU_i/dx_j}^{(\omega')}$ at each spatial grid point. The time derivative is defined as $\widehat{\boldsymbol{D}_t}^{(\omega)} = -\mathrm{i}\omega$.

Thus, each velocity and pressure vector corresponding to a frequency ω is coupled to other frequencies via the mean velocity and shear profiles. Only interactions between frequencies contained in Ω are taken into account. The set Ω at most contains all the resolved frequencies of the mean velocity and shear, though a much smaller subset of frequencies is usually used for computational tractability. In the formulation of traditional resolvent operator (Chapter 2.1), $\widehat{U_i}^{(\omega-\omega')} = 0$ and $\widehat{dU_i/dx_j}^{(\omega-\omega')} = 0$ for $\omega \neq \omega'$. The frequencies are decoupled and we can take Ω to be the singleton $\{\omega\}$ and analyze each frequency independently.

Equations (2.18) can be recast as a linear mapping between forcing terms, and velocity and pressure fluctuations. For systems that are homogeneous in the x_1 and

x_3 directions, we obtain

$$\begin{bmatrix} \hat{\boldsymbol{u}}_1^{(\omega_1)}(x_2) \\ \hat{\boldsymbol{u}}_2^{(\omega_1)}(x_2) \\ \hat{\boldsymbol{u}}_3^{(\omega_1)}(x_2) \\ \hat{\boldsymbol{p}}^{(\omega_1)}(x_2) \\ \hat{\boldsymbol{u}}_1^{(\omega_2)}(x_2) \\ \hat{\boldsymbol{u}}_2^{(\omega_2)}(x_2) \\ \hat{\boldsymbol{u}}_3^{(\omega_2)}(x_2) \\ \hat{\boldsymbol{p}}^{(\omega_2)}(x_2) \\ \cdots \end{bmatrix} = \widehat{\boldsymbol{H}}^{(k_1,k_3,\Omega)} \begin{bmatrix} \hat{\boldsymbol{f}}_1^{(\omega_1)}(x_2) \\ \hat{\boldsymbol{f}}_2^{(\omega_1)}(x_2) \\ \hat{\boldsymbol{f}}_3^{(\omega_1)}(x_2) \\ \mathbf{0}^{N_2\times 1} \\ \hat{\boldsymbol{f}}_1^{(\omega_2)}(x_2) \\ \hat{\boldsymbol{f}}_2^{(\omega_2)}(x_2) \\ \hat{\boldsymbol{f}}_3^{(\omega_2)}(x_2) \\ \mathbf{0}^{N_2\times 1} \\ \cdots \end{bmatrix}, \tag{2.19}$$

where $\Omega = \{\omega_k\}_{k=1}^{N_\Omega}$. The harmonic resolvent operator $\widehat{\boldsymbol{H}}^{(k_1,k_3,\Omega)} \in \mathbb{C}^{4N_2N_\Omega} \times C^{4N_2N_\Omega}$ is subsequently decomposed so that its singular modes and values can be inspected. As an illustrative example, in order to showcase the structure of $\widehat{\boldsymbol{H}}^{(k_1,k_3,\Omega)}$, we choose $\Omega = \{-\omega, 0, \omega\}$ for an arbitrary frequency ω. The resolvent operator for the system is

$$\widehat{\boldsymbol{H}}^{(k_1,k_3,\Omega)} = \begin{bmatrix} \left[\widehat{\boldsymbol{H}}^{(k_1,k_3,-\omega)}\right]^{-1} & \boldsymbol{G}^{(-\omega)} & \mathbf{0}^{4N_2\times 4N_2} \\ \boldsymbol{G}^{(\omega)} & \left[\widehat{\boldsymbol{H}}^{(k_1,k_3,0)}\right]^{-1} & \boldsymbol{G}^{(-\omega)} \\ \mathbf{0}^{4N_2\times 4N_2} & \boldsymbol{G}^{(\omega)} & \left[\widehat{\boldsymbol{H}}^{(k_1,k_3,\omega)}\right]^{-1}, \end{bmatrix}^{-1} \tag{2.20}$$

where $\widehat{\boldsymbol{H}}^{(k_1,k_3,-\omega)}$, $\widehat{\boldsymbol{H}}^{(k_1,k_3,0)}$ and $\widehat{\boldsymbol{H}}^{(k_1,k_3,\omega)}$ are defined according to equation (2.6), and the cross terms $G^{(\omega)} \in \mathbb{C}^{4N_2\times 4N_2}$ are defined as

$$\boldsymbol{G}^{(\omega)} := \begin{bmatrix} \widehat{\boldsymbol{U}_1}^{(\omega)}\boldsymbol{D}_1 + \widehat{\boldsymbol{dU}}_{1,1}^{(\omega)} & \widehat{\boldsymbol{U}_2}^{(\omega)}\boldsymbol{D}_2 + \widehat{\boldsymbol{dU}}_{1,2}^{(\omega)} & \widehat{\boldsymbol{U}_3}^{(\omega)}\boldsymbol{D}_3 + \widehat{\boldsymbol{dU}}_{1,3}^{(\omega)} & \mathbf{0}^{N_2\times N_2} \\ \widehat{\boldsymbol{U}_1}^{(\omega)}\boldsymbol{D}_1 + \widehat{\boldsymbol{dU}}_{2,1}^{(\omega)} & \widehat{\boldsymbol{U}_2}^{(\omega)}\boldsymbol{D}_2 + \widehat{\boldsymbol{dU}}_{2,2}^{(\omega)} & \widehat{\boldsymbol{U}_3}^{(\omega)}\boldsymbol{D}_3 + \widehat{\boldsymbol{dU}}_{2,3}^{(\omega)} & \mathbf{0}^{N_2\times N_2} \\ \widehat{\boldsymbol{U}_1}^{(\omega)}\boldsymbol{D}_1 + \widehat{\boldsymbol{dU}}_{3,1}^{(\omega)} & \widehat{\boldsymbol{U}_2}^{(\omega)}\boldsymbol{D}_2 + \widehat{\boldsymbol{dU}}_{3,2}^{(\omega)} & \widehat{\boldsymbol{U}_3}^{(\omega)}\boldsymbol{D}_3 + \widehat{\boldsymbol{dU}}_{3,3}^{(\omega)} & \mathbf{0}^{N_2\times N_2} \\ \mathbf{0}^{N_2\times N_2} & \mathbf{0}^{N_2\times N_2} & \mathbf{0}^{N_2\times N_2} & \mathbf{0}^{N_2\times N_2} \end{bmatrix}. \tag{2.21}$$

When the mean flow is constant in time, $\boldsymbol{G}^{(\omega)} = \mathbf{0}$ for every $\omega \in \Omega$, and the harmonic resolvent operator becomes block-diagonal. In this case, we can conduct a traditional Fourier-based resolvent analysis for each of the N_Ω frequencies independently. Before computing the SVD of $\widehat{\boldsymbol{H}}^{(k_1,k_3,\Omega)}$, the operator is weighted with the integration weights pertaining to the chosen grid, as in Chapter 3.2.

Harmonic resolvent analysis has been used to analyze the flow past an airfoil tilted at a nonzero angle of attack (Padovan et al., 2020). This particular flow is found to be most sensitive to forcing at the frequency of vortex shedding, and produces principal forcing structures focused in the leading and trailing edges of the airfoil, and response structures in the form of positive and negative velocity anomalies that propagate downstream of the airfoil. The modes match simulations of the flow in which a small perturbation at the vortex shedding frequency is introduced. In Padovan and Rowley (2022), the method is applied to a forced axisymmetric jet in order to investigate the mechanisms of vortex pairing. The authors report diminished vortex pairing when the applied forcing does not have a component in the direction of the principal harmonic forcing mode. This suggests that vortex pairing is a response to linear amplification mechanisms; suppressing these in turn suppresses vortex pairing.

Via harmonic resolvent analysis, the traditional Fourier-based resolvent framework can be expanded to flows with time-periodic mean profiles. Interactions between frequencies are enabled by the oscillating mean flow, though, for the sake of efficiency, only a handful of these are chosen to be represented when formulating the harmonic resolvent operator. Harmonic resolvent analysis can reveal new linear amplification mechanisms that arise from this cross-frequency coupling. Nevertheless, the modes that it produces tend to oscillate over the entire considered time domain. The purpose of this work is to develop a resolvent-based method that can investigate short-lived or time-localized phenomena. Moreover, we aim to extend resolvent analysis to accommodate a wider class of boundary conditions in time; harmonic resolvent analysis is indeed restricted to time-periodic mean flows. With this chapter, we conclude our brief overview of Fourier-based resolvent analysis methods. The rest of the work focuses on introducing, validating, and applying our proposed solution to the boundary condition and time-localization issues of traditional resolvent formulations: wavelet-based resolvent analysis.

Chapter 3

WAVELET-BASED RESOLVENT ANALYSIS

In this chapter, we introduce wavelet-based resolvent analysis, which extends resolvent analysis to statistically non-stationary flows by encoding transient behavior in the mean flow or the fluctuations. Rather than use Fourier modes in time as in Chapter 2.1, we reformulate the resolvent operator in a wavelet basis in time. Wavelets are functions that can be used as basis functions to represent square-integrable functions, much like Fourier modes. The amplitude of each wavelet, however, tends to be concentrated in a subset of its domain, and unlike Fourier modes in time, wavelets can capture information centered at a particular time interval. Resolvent modes formulated in wavelet basis are thus endowed with both time and frequency information.

3.1 A note on wavelets

A wavelet transformation of a square-integrable function projects this function on a complete basis generated by the wavelet. This basis is composed of dilations and shifts of a mother wavelet, which we denote by $\eta(t)$. Wavelet transforms are not unique and are determined by the choice of the mother wavelet. For the remainder of this work, we assume here that $\eta(t)$ is real. The translations and dilations of $\eta(t)$ are given by

$$\eta_{\alpha,\beta}(t) \equiv \frac{1}{\sqrt{\alpha}}\eta\left(\frac{t}{\alpha} - \beta\right), \tag{3.1}$$

where α and β correspond to the scale and shift parameters, respectively. As mentioned, the mass of a wavelet tends to be concentrated in particular time interval; the shift parameter β represents the location of that subset of the domain. Larger values β correspond to later times. The scale parameter α determines the spread of the wavelet's mass, with larger values of α representing wider wavelets. Similarly, α controls the location and spread of the wavelet's time-Fourier spectrum in the frequency domain.

Consider an arbitrary square-integrable function $g(t)$. Its Fourier and wavelet transforms are

$$\hat{g}(\omega) = \int_{-\infty}^{+\infty} g(t)e^{-\mathrm{i}\omega t}dt, \tag{3.2}$$

$$\tilde{g}^{(w)}(\alpha,\beta) = \int_{-\infty}^{+\infty} g(t)\eta_{\alpha,\beta}(t)dt, \tag{3.3}$$

where $\mathrm{i} = \sqrt{-1}$. The wavelet coefficient $\tilde{g}^{(w)}(\alpha,\beta)$ captures information from g centered at a time interval determined by α, and a frequency interval determined by β.

There exists a trade-off between precision in frequency and precision in time; the more localized $g(t)$ is in time, the less $\hat{g}(\omega)$ is in frequency, and vice versa (Mallat, 1999). For any "well-behaved" function g, *i.e.* the function along with its derivatives decay faster than any polynomial as $|t| \longrightarrow \infty$, we can derive the following uncertainty principle governing the spread of the function and its Fourier transform over their respective domains:

$$\begin{aligned}
\left(\int_{-\infty}^{\infty} t^2|g(t)|^2dt\right)\left(\int_{-\infty}^{\infty} \omega^2|\hat{g}(\omega|^2d\omega\right) &= \left(\int_{-\infty}^{\infty} t^2|g(t)|^2dt\right)\left(\int_{-\infty}^{\infty} \left|\widehat{\frac{dg}{dt}}(\omega)\right|^2 d\omega\right) \\
&= \left(\int_{-\infty}^{\infty} t^2|g(t)|^2dt\right) \cdot 2\pi \left(\int_{-\infty}^{\infty} \left|\frac{dg}{dt}(t)\right|^2 dt\right) \\
&\geq 2\pi \left(\int_{-\infty}^{\infty} tg(t)\frac{dg}{dt}(t)dt\right)^2 \\
&\geq 2\pi \left(\int_{-\infty}^{\infty} \frac{t}{2}\frac{dg^2}{dt}(t)dt\right)^2 \\
&\geq \frac{\pi}{2}\underbrace{\left(\int_{-\infty}^{\infty} |g(t)|^2dt\right)^2}_{\text{finite}}.
\end{aligned} \tag{3.4}$$

The second equality is a due to the Plancherel identity, the third line is a consequence of the Cauchy-Schwarz inequality, and the final result is obtained after integration by parts. Though not apparent at first glance, the trade-off is even harsher: the supports of g and $\hat{g}$ cannot be simultaneously compact (Mallat, 1999). Thus, one cannot find a wavelet $\eta(t)$ that simultaneously captures the value of $g(t)$ at a given t and the value of $\hat{g}(\omega)$ at a given ω. As two extreme examples, consider the Dirac delta centered at $t = 1$, which is perfectly localized in time but with an infinite spread in frequency, and the Fourier mode $e^{\mathrm{i}t}$, which is perfectly localized in frequency space at $\omega = 1$ but has infinite spread in time. This trade-off is discussed further in Chapter 3.2.

In practice, we define the wavelet transform on a dyadic grid, *i.e.* $\alpha = 2^{\ell}$, $\beta = m$ for $m,\ \ell \in \mathbb{Z}$. Orthogonal wavelets are often used; these satisfy the following properties:

$$\int_{-\infty}^{\infty} \eta_{\alpha,\beta}\eta_{\alpha',\beta'}\,dt = \begin{cases} 1 \text{ if } \alpha = \alpha' \text{ and } \beta = \beta' \\ 0 \text{ otherwise.} \end{cases} \tag{3.5}$$

This allows us to form a basis $\{\eta(t/2^\ell - m)/\sqrt{2^\ell}\}_{\ell,\, m\in\mathbb{Z}}$ that can be used to construct square-integrable functions. Our arbitrary function g can be expanded as

$$g(t) = \sum_{\ell,m=-\infty}^{+\infty} \tilde{g}^{(w)}(2^\ell, m)\eta_{2^\ell,m}(t). \tag{3.6}$$

To formulate wavelet-based resolvent analysis, we must construct a discrete wavelet transform. Suppose the domain of g is restricted to be $[0,T]$ and N_t is the number of grid points. Suppose without loss of generality that $T = N_t - 1$. Given these limitations, we cannot dilate and shift our function g infinitely, and the expansion (3.6) is truncated. For each choice of mother wavelet η, there exists a corresponding scaling function ζ which captures the residual from the truncation of the expansion:

$$g(t) = \sum_{\ell=1}^{L}\sum_{m=0}^{N_t/2^\ell-1} \frac{1}{\sqrt{2^\ell}}\tilde{g}^{(w)}\eta\left(\frac{t}{2^\ell} - m\right) + \sum_{m=0}^{N_t/2^L-1} \frac{1}{\sqrt{2^L}}\tilde{g}^{(s)}\zeta\left(\frac{t}{2^L} - m\right), \tag{3.7}$$

where $L \in \mathbb{N}$ represents the largest scale captured by the wavelet expansion, and

$$\tilde{g}^{(s)}(2^L, m) := \int_{-\infty}^{+\infty} \frac{1}{\sqrt{2^L}} g(t)\zeta\left(\frac{t}{2^L} - m\right) dt. \tag{3.8}$$

We note that L satisfies $2^L \leq N_t$. When the wavelets are orthogonal, the scaling functions satisfy:

$$\int_{-\infty}^{\infty} \zeta\left(\frac{t}{2^L} - m\right)\zeta\left(\frac{t}{2^L} - m'\right) dt = \begin{cases} 1 \text{ if } m = m' \\ 0 \text{ otherwise.} \end{cases} \tag{3.9}$$

Shifts of scaling functions of the same scale are pairwise orthogonal, but scaling functions at different scales are not.

Discrete wavelet transform

To construct the discrete wavelet transform on uniform dyadic grid, we first assume that the time step $\Delta t := T/N_t$ is small enough so that $\zeta(t/\Delta t - m)/\Delta t$—the smallest possible scaling of the mother function for the chosen grid and its shifts—approximate Dirac deltas:

$$g(t) \approx \sum_{m=0}^{N_t} g(m\Delta t)\zeta\left(\frac{t}{\Delta t} - m\right). \tag{3.10}$$

Assuming $L = 1$, the wavelet and scaling function coefficients can be obtained as

$$\tilde{g}^{(s)}(2, m) \approx \sum_{k=0}^{N_t} g(k\Delta t) \left[\frac{1}{\sqrt{2}} \int_{-\infty}^{+\infty} \zeta(t-k)\zeta\left(\frac{t}{2} - m\right) dt \right], \tag{3.11}$$

$$\tilde{g}^{(w)}(2, m) \approx \sum_{k=0}^{N_t} g(k\Delta t) \left[\frac{1}{\sqrt{2}} \int_{-\infty}^{+\infty} \zeta(t-k)\eta\left(\frac{t}{2} - m\right) dt \right]. \tag{3.12}$$

Thus, gathering the values of g at each time step into a vector $\boldsymbol{g}$, and the coefficients $\tilde{g}^{(s)}(2, m)$ and $\tilde{g}^{(w)}(2, m)$ into a vector $\tilde{\boldsymbol{g}}^T = [\tilde{\boldsymbol{g}}^{(s)^T}, \tilde{\boldsymbol{g}}^{(w)^T}]^T$ of size N_t, we express the discrete wavelet transform as

$$\tilde{\boldsymbol{g}} = \boldsymbol{W}\boldsymbol{g}, \tag{3.13}$$

where the m^{th} row and k^{th} column of $\boldsymbol{W}$ contains the precomputed values of $\int_{-\infty}^{+\infty} \zeta(t-k)\zeta\left(t/2 - m\right) dt/\sqrt{2}$, and the $(m + N_t/2)^{\text{th}}$ row and k^{th} column of $\boldsymbol{W}$ contains the precomputed values of $\int_{-\infty}^{+\infty} \zeta(t-k)\eta\left(t/2 - m\right) dt/\sqrt{2}$, for $m,\ k = 0, \ldots, N_t/2$. When $L = 1$, this wavelet transformation is referred to as "single-stage".

In order to perform a higher-stage ($L = 2$) expansions in the wavelet basis, we can simply express the residuals in terms of $\eta(t/2^2 - m)/\sqrt{2^2}$ and $\zeta(t/2^2 - m)/\sqrt{2^2}$. In other words, we repeat a single-stage transformation on the vector $\tilde{\boldsymbol{g}}^{(s)}$ of size $N_t/2$, noticing that, after a change of variables $t' = t/2$,

$$\frac{1}{\sqrt{2}}\frac{1}{\sqrt{4}} \int_{-\infty}^{+\infty} \zeta\left(\frac{t}{2} - k\right)\zeta\left(\frac{t}{4} - m\right) dt = \frac{1}{\sqrt{2}} \int_{-\infty}^{+\infty} \zeta(t'-k)\zeta\left(\frac{t'}{2} - m\right) dt', \tag{3.14}$$

$$\frac{1}{\sqrt{2}}\frac{1}{\sqrt{4}} \int_{-\infty}^{+\infty} \zeta\left(\frac{t}{2} - k\right)\eta\left(\frac{t}{4} - m\right) dt = \frac{1}{\sqrt{2}} \int_{-\infty}^{+\infty} \zeta(t'-k)\eta\left(\frac{t'}{2} - m\right) dt'. \tag{3.15}$$

Here, $m, k = 0, \ldots, N_t/4$. In other words, the second-stage of the transformation of $\tilde{\boldsymbol{g}}^{(s)}$ contains the same elements of the single-stage transform. Thus, the expansion (3.7) is performed efficiently and recursively up to $L \leq \log_2(N_t)$. For the rest of the work, $\boldsymbol{W}$ refers to the full discrete wavelet transform, and not just the single-stage transform.

Defined such, the discrete transform $\tilde{\boldsymbol{g}}$ contains N_t elements. The first $N_t/2^L$ approximate the coefficients $\tilde{g}^{(s)}(2^L, m)$, for $m = 0, \ldots, (N_t/2^L - 1)$; the subsequent $N_t/2^L$ elements approximate the coefficients $\tilde{g}^{(w)}(2^L, m)$, for $m = 0, \ldots, (N_t/2^L - 1)$, which are followed by $N_t/2^{L-1}$ elements representing $\tilde{g}^{(w)}(2^{L-1}, m)$, for $m = 0, \ldots, (N_t/2^{L-1} - 1)$, etc. (Figure 3.1) For each ℓ and m, the coefficients roughly captures a portion of the frequency content of g, centered in a time interval determined by m. The coefficients $\tilde{g}^{(w)}(2^\ell, m)$ terms approximate $g(t)$ at scales $-\infty < 2^\ell \leq 2^L$,

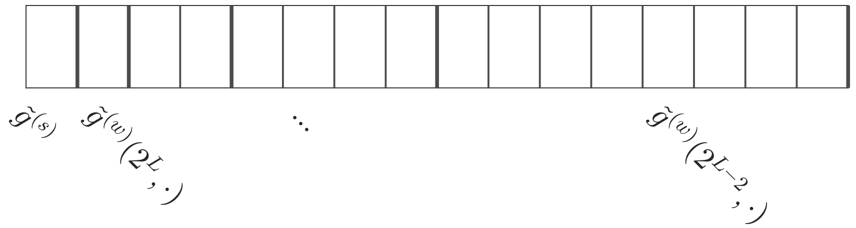

Figure 3.1: Representation of a discrete wavelet transform vector for $N_t = 16$ and $L = 4$. Each box represents an element of the vector. The leftmost vertical line in bold separates the scaling function coefficients from the wavelet coefficients; the rest delimit the scales $\ell = 1, 2, \ldots, L$.

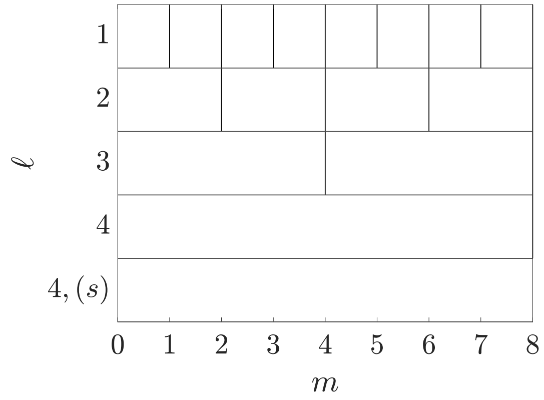

Figure 3.2: Scalogram grid for $N_t = 16$ and $L = 4$. Each box represents an element of a discrete transform vector. '4, (s)' denotes the residual scale captured by the $(\cdot)^{(s)}$ coefficient.

and the $\tilde{g}^{(s)}(2^L, m)$ terms capture the residual at scales $2^\ell > 2^L$. Larger ℓ corresponds to a narrower band of frequencies closer to zero, while larger k corresponds to later times. The wavelet coefficients are often plotted in the time-frequency plane on a scalogram (Mallat, 1999; Najmi, 2012). A scalogram with visible grid lines is shown in Figure 3.2. The scalogram showcases the trade-off between frequency and time localization: larger scales (lower frequencies) have lower resolution in time, and vice versa.

The choice of the largest scale $L \leq \ell$ depends on the band of frequencies we wish to study with our wavelet-based resolvent operator: narrower bands closer to zero will require larger L. To illustrate this, consider the Shannon wavelet, which as a perfect bandpass filter (Mallat, 1999; Najmi, 2012). The Shannon wavelet indeed allows the separation of the frequency content of a function into distinct non-overlapping bands, covering frequency band $N_t/2^\ell([-2\pi, -\pi] \cup [\pi, 2\pi])$ for each ℓ (Figure 3.3). Its scaling function covers the remainder of the resolved frequency spectrum:

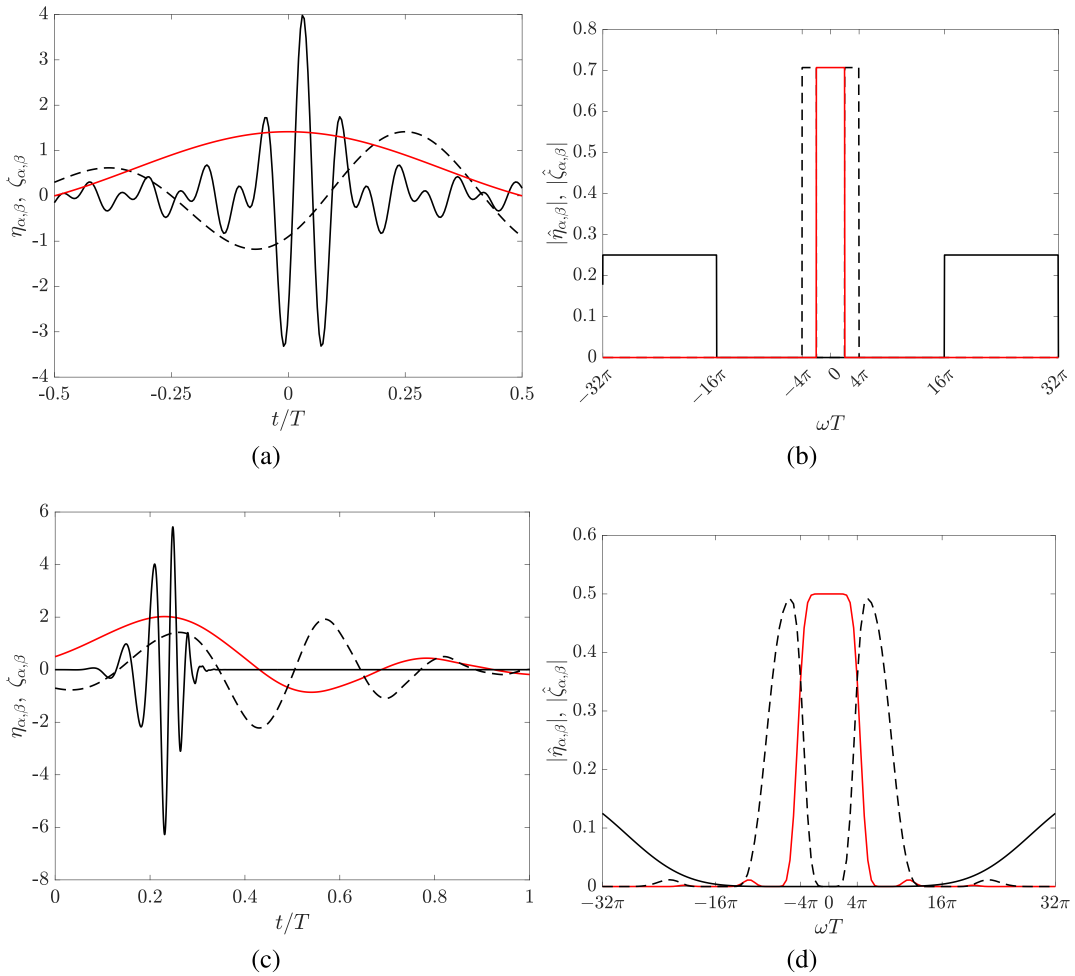

(a) (b)

(c) (d)

Figure 3.3: Shannon wavelets (black) and scaling function (red) in (a) time and (b) frequency (b) domains. Daubechies-16 wavelets (black) and scaling function (red) in (c) time and (d) frequency domains. The functions shown are two wavelets for $\alpha = 2^L = N_t$ (black $--$) and $\alpha = 2^{L-3}$ (black $--$), and a scaling function for $\alpha = 2^L$ (red $-$) for arbitrary shift parameters. T represents the size of the time domain.

$N_t/2^L[-\pi, \pi]$. Increasing L permits us to extract the low frequency content of g with more precision.

The choice of wavelet-scaling-function pair determines the properties of the transform operator $\boldsymbol{W}$. For compactly supported wavelets and scaling function, elements $\int_{-\infty}^{+\infty} \zeta(t-k)\zeta\,(t/2 - m)\;dt/\sqrt{2}$ and $\int_{-\infty}^{+\infty} \zeta(t-k)\eta\,(t/2 - m)\;dt/\sqrt{2}$ are zero for large values of m and k, yielding a sparse banded matrix $\boldsymbol{W}$. For orthonormal wavelets and scaling functions, $\boldsymbol{W}$ is unitary (Ballouz, Lopez-Doriga, et al., 2024; Mallat, 1999; Najmi, 2012). We note that since the spectrum of the Shannon wavelet and its scaling function is compactly supported, the functions themselves must have infinite spread in time, which yields a dense discrete wavelet transform matrix.

3.2 Formulation of wavelet-based resolvent analysis

The benefit of the wavelet transform in time is that it preserves both time and frequency information. The wavelet transforms are functions of time shift and scale, respectively associated with time and frequency information, whereas the Fourier transform is a function of only frequency. To endow our resolvent modes with a dependency on time while preserving some information about their frequency content, we perform a wavelet transform on equations (2.3) after Fourier-transforming them in homogeneous spatial directions.

We discretize the spatially Fourier-transformed equations in both time and the remaining spatial dimensions. Let $[0, T]$ define the time domain, which we discretize using N_t points. We then apply a discrete wavelet transform $\boldsymbol{W}$ to the left of the discrete equations:

$$\widetilde{\boldsymbol{D}_t}\widetilde{\boldsymbol{u}}_i + \widetilde{\boldsymbol{u}}_j\widetilde{\boldsymbol{dU}_{i,j}} + \widetilde{\boldsymbol{U}_j}\widetilde{\boldsymbol{D}_j}\widetilde{\boldsymbol{u}}_i = -\widetilde{\boldsymbol{D}}_i\widetilde{\boldsymbol{p}} + \frac{1}{Re}\widetilde{\boldsymbol{L}}\widetilde{\boldsymbol{u}}_i + \widetilde{\boldsymbol{f}}_i, \quad \widetilde{\boldsymbol{D}}_i\widetilde{\boldsymbol{u}}_i = 0. \tag{3.16}$$

Here, $\widetilde{\boldsymbol{u}}_i$, $\widetilde{\boldsymbol{f}}_i$, and $\widetilde{\boldsymbol{p}}$ respectively denote the discretized and transformed u_i, f_i, and p. For a system that is homogeneous in the x_1 and x_3 directions, these quantities are discretized over x_2, ℓ and m. The wavelet-transformed vectors also have a resolution of N_t in the space of wavelet parameters ℓ and m. We introduce $\widetilde{\boldsymbol{U}_j} := \boldsymbol{W}\boldsymbol{U}_i\boldsymbol{W}^{-1}$ and $\widetilde{\boldsymbol{dU}_{i,j}} := \boldsymbol{W}\boldsymbol{dU}_{i,j}\boldsymbol{W}^{-1}$, where $\boldsymbol{U}_i$ and $\boldsymbol{dU}_{i,j}$ are the diagonal matrices whose diagonal terms are respectively U_i and $\partial U_i/\partial x_j$ evaluated at x_2 and t grid points. Thus, the mean velocity and shear profiles are allowed to vary in time.

For a system that is homogeneous in the x_1 and x_3 directions, $\boldsymbol{U}_2 = \boldsymbol{dU}_{i,1} = \boldsymbol{dU}_{i,3} = \boldsymbol{0}$, and for a streamwise and spanwise wave number pair (k_1, k_3), $\widetilde{\boldsymbol{D}}_1 = \widehat{\boldsymbol{D}}_1 = \mathrm{i}k_1$, $\widetilde{\boldsymbol{D}}_2 = \widehat{\boldsymbol{D}}_2 = \boldsymbol{D}_2$, $\widetilde{\boldsymbol{D}}_3 = \widehat{\boldsymbol{D}}_3 = \mathrm{i}k_3$, and $\widetilde{\boldsymbol{L}} = \widehat{\boldsymbol{L}} = -k_1^2 + \boldsymbol{D}_2^2 - k_3^2$. We define the transformed time derivative operator $\widetilde{\boldsymbol{D}_t} := \boldsymbol{W}\boldsymbol{D}_t\boldsymbol{W}^{-1}$, where $\boldsymbol{D}_t$ refers to the discrete time differentiation matrix. Similarly to the Fourier-based resolvent analysis, the equations can be written in matrix form as

$$\begin{bmatrix} \widetilde{\boldsymbol{u}}_1(x_2, \ell, m) \\ \widetilde{\boldsymbol{u}}_2(x_2, \ell, m) \\ \widetilde{\boldsymbol{u}}_3(x_2, \ell, m) \\ \widetilde{\boldsymbol{p}}(x_2, \ell, m) \end{bmatrix} = \widetilde{\boldsymbol{H}}^{(k_1,k_3)} \begin{bmatrix} \widetilde{\boldsymbol{f}}_1(x_2, \ell) \\ \widetilde{\boldsymbol{f}}_2(x_2, \ell, m) \\ \widetilde{\boldsymbol{f}}_3(x_2, \ell, m) \\ 0 \end{bmatrix}, \tag{3.17}$$

where the functional dependence on x_2, ℓ and m represents the discretization over the wall-normal spatial dimension, and the wavelet shifts and scales, and the wavelet-based resolvent operator $\tilde{\boldsymbol{H}} \in \mathbb{C}^{4N_t \times N_2} \times \mathbb{C}^{4N_t \times N_2}$ is defined as

$$\widetilde{\boldsymbol{H}}^{(k_1,k_3)} = \left[\left(\widetilde{\boldsymbol{D}_t} - \frac{1}{Re}\boldsymbol{L} + \mathrm{i}k_1 \widetilde{\boldsymbol{U}_1} + \widetilde{\boldsymbol{U}_2}\boldsymbol{D}_2 + \mathrm{i}k_3 \widetilde{\boldsymbol{U}_3} \right) \begin{pmatrix} \boldsymbol{I} & \mathbf{0} & \mathbf{0} & \mathbf{0} \\ \mathbf{0} & \boldsymbol{I} & \mathbf{0} & \mathbf{0} \\ \mathbf{0} & \mathbf{0} & \boldsymbol{I} & \mathbf{0} \\ \mathbf{0} & \mathbf{0} & \mathbf{0} & \mathbf{0} \end{pmatrix} + \begin{pmatrix} \mathbf{0} & \widetilde{\boldsymbol{dU}}_{1,2} & \mathbf{0} & \mathrm{i}k_1\boldsymbol{I} \\ \mathbf{0} & \widetilde{\boldsymbol{dU}}_{2,2} & \mathbf{0} & \boldsymbol{D}_2 \\ \mathbf{0} & \widetilde{\boldsymbol{dU}}_{3,2} & \mathbf{0} & \mathrm{i}k_3\boldsymbol{I} \\ \mathrm{i}k_1\boldsymbol{I} & \boldsymbol{D}_2 & \mathrm{i}k_3\boldsymbol{I} & \mathbf{0} \end{pmatrix} \right]^{-1} . \qquad (3.18)$$

Before computing the SVD of the wavelet-based resolvent operator, we pre- and post-multiply by diagonal matrices that contain the integration weights in time and x_2 and that zero-out the pressure component in order to maximize the x_2–integrated action of the forcing term. We denote the principal forcing and response modes obtained under this formulation by $\tilde{\boldsymbol{\phi}}(x_2, \ell, m) = [\tilde{\boldsymbol{\phi}}_1^T, \tilde{\boldsymbol{\phi}}_2^T, \tilde{\boldsymbol{\phi}}_3^T, \mathbf{0}^T]^T$ and $\tilde{\boldsymbol{\psi}}(x_2, \ell, m) = [\tilde{\boldsymbol{\psi}}_1^T, \tilde{\boldsymbol{\psi}}_2^T, \tilde{\boldsymbol{\psi}}_3^T, \tilde{\boldsymbol{\psi}}_p^T]^T$ respectively. We denote their respective inverse wavelet-transforms by $\breve{\boldsymbol{\phi}}(x_2, t) := \boldsymbol{W}^{-1}\tilde{\boldsymbol{\phi}}$ and $\breve{\boldsymbol{\psi}}(x_2, t) := \boldsymbol{W}^{-1}\tilde{\boldsymbol{\psi}}$. These are normalized such that integrated kinetic energy satisfies

$$\frac{1}{T}\frac{1}{L_2}\int_0^T \int_0^{L_2} |\breve{\phi}_1|^2 + |\breve{\phi}_1|^2 + |\breve{\phi}_3|^2 dx_2 dt = 1, \qquad (3.19)$$

$$\frac{1}{T}\frac{1}{L_2}\int_0^T \int_0^{L_2} |\breve{\psi}_1|^2 + |\breve{\psi}_2|^2 + |\breve{\psi}_3|^2 dx_2 dt = 1. \qquad (3.20)$$

We denote the inverse Fourier transforms of the modes to the physical domain by $\boldsymbol{\phi}(x_1, x_2, x_3, t)$ and $\boldsymbol{\psi}(x_1, x_2, x_3, t)$, respectively.

Wavelet-based resolvent analysis with windowing

The principal forcing mode of the full operator $\widetilde{\boldsymbol{H}}^{(k_1,k_3)}$ is the perturbation that maximizes the integrated action of the velocity fluctuations over the entire time domain, which is useful for capturing response structures that tend to persist in time. Additionally, one might be interested in studying the linear amplification properties of a particular time interval in the time progression of the mean flow profile, or the behavior of a particular group of waves traveling at a desired velocity. Under the wavelet-based formulation, we can construct a resolvent map between forcing and response terms at specific time shifts and scales by defining a windowed resolvent operator:

$$\begin{bmatrix} \widetilde{\boldsymbol{u}}_1(x_2,\ell,m) \\ \widetilde{\boldsymbol{u}}_2(x_2,\ell,m) \\ \widetilde{\boldsymbol{u}}_3(x_2,\ell,m) \\ \widetilde{\boldsymbol{p}}(x_2,\ell,m) \end{bmatrix} = \boldsymbol{C}\widetilde{\boldsymbol{H}}^{(k_1,k_3)}\boldsymbol{B} \begin{bmatrix} \widetilde{\boldsymbol{f}}_1(x_2,\ell,m) \\ \widetilde{\boldsymbol{f}}_2(x_2,\ell,m) \\ \widetilde{\boldsymbol{f}}_3(x_2,\ell,m) \\ 0 \end{bmatrix}, \tag{3.21}$$

where $\boldsymbol{B}$ and $\boldsymbol{C}$ are windowing matrices that select a subset of the forcing and response modes, respectively. Spatial windowing matrices have been used to study phenomena that tend to occur in a specific region of the spatial domain (Jeun et al., 2016; Kojima et al., 2020). Windowing can also isolate the forcing or response to a particular flow variable, and by windowing the forcing to controllable flow variables and to regions reachable by actuators, one can compute linearly optimal forcing modes that are physically realizable.

The wavelet-based formulation introduced in this chapter extends this localizability to the temporal and frequency domains. For example, to select a desired scale and shift parameter (ℓ_d, m_d) for the forcing mode, we set

$$\boldsymbol{B} = \operatorname{diag}\big(\mathbb{1}(\ell = \ell_d)\mathbb{1}(m = m_d)\big), \tag{3.22}$$

where $\mathbb{1}(\cdot)$ is an indicator function. Here, $\boldsymbol{B}$ selects the relevant columns of $\boldsymbol{W}^{-1}$ corresponding to the wavelet scales and shifts to which we wish to restrict our forcing. Analogously, $\boldsymbol{C}$ selects the rows of $\boldsymbol{W}$ corresponding to the wavelet scales and shifts to which we restrict our response modes. The SVD of the windowed resolvent operator, $\boldsymbol{C}\widetilde{\boldsymbol{H}}^{(k_1,k_3)}\boldsymbol{B}$, allows us to identify forcing and response modes restricted to frequency and time intervals determined by the selected wavelet coefficients.

We can view windowing as analogous to restricting the harmonic resolvent operator to a set of interacting frequencies Ω (Chapter 2.2). The windowed wavelet-based formulation also allows us to study a band of interacting frequencies, but additionally gives us the flexibility to focus on a time interval of interest. The ability of wavelet-based formulation to study the amplification properties of time- or frequency-localized greatly events expands the use cases of resolvent analysis. The method can also shed new light on cases where the mean profile is constant in time and that are usually studied using the traditional Fourier-based formulation. Intermittent and transient phenomena are of interest even in stationary turbulent flows, and under the new formulation, with the help of windowing, the linear analysis of such transient phenomena becomes possible, as will be explored in Chapter 4.1.

When making use of windowing, our choice of wavelets impacts the physical interpretation of the windowed modes. For example, in the channel flow case where critical layer dynamics are important, the Shannon wavelet would allow us to study wave speeds of interest with more precision due to its being a perfect bandpass filter (Ballouz, Lopez-Doriga, et al., 2024; Ballouz et al., 2023). Constraining the resolvent modes to a particular dilation of the Shannon wavelet would highlight waves of frequencies strictly contained in the frequency band of the chosen wavelet. If more precision is required in the time domain to study time-localized phenomena, a wavelet that is compactly supported in time is more pertinent. This is the case, for example, in Ballouz, Dawson, and Bae, 2024, which studies how a compactly supported resolvent forcing function affects a turbulent channel beyond its time support. In some cases, both properties can be combined through the use of wavelets that are compactly supported in time but whose frequency Fourier spectra decay quickly outside a certain frequency band, making them quasibandpass filters. The Daubechies or the Fejér-Korovkin wavelets satisfy these properties, and in the case of turbulent channel flow (Chapter 4.1), produce similar results as when a Shannon wavelet-transform is used. The physical interpretation of constraining forcing and/or response modes to a specific wavelet, along with the numerical cost of using a sparse wavelet transform over a dense one, both inform our selection of wavelet transform.

3.3 Notes on improving efficiency

The construction of $\tilde{\boldsymbol{H}}$ requires the inversion of a $4N_2N_t \times 4N_2N_t$ matrix, assuming the x_1 and x_3 are the homogeneous directions. This computation costs $O(N_2^3N_t^3)$ operations when solved directly, and the full SVD of $\tilde{\boldsymbol{H}}$ would also require $O(N_2^3N_t^3)$ operations. Indeed, relaxing the assumption of homogeneity in any dimension would nominally increase the computational cost of the method by the cube of the corresponding grid size. For example, using a grid of size N_1 to discretize the x_1-direction increases the complexity of resolvent analysis by a factor of N_1^3. Thus, with a direct solve, the wavelet-based resolvent analysis would nominally cost $O(N_t^2)$-times more than performing N_t separate Fourier-based resolvent for each temporal scale, though the latter would fail to capture the interactions between the different time scales. In this section, we discuss some methods to reduce the computational cost and memory storage requirements of the method.

One method for reducing the memory and computational cost of wavelet-based resolvent analysis is to use sparse finite difference operators and wavelet transforms when constructing $\widetilde{\boldsymbol{H}}^{-1}$, which reduces the memory storage costs of the matrix. For example, in Chapters 3.6, 4.1, and 5, we use Daubechies wavelets, which trade the perfect bandpass property of Shannon wavelets for a compact support in time, thus yielding a sparse discrete wavelet transform matrix. Daubechies wavelets are a family of wavelets characterized by their support width: higher index wavelets—Daubechies-8 *versus* Daubechies-4—behave more closely to perfect bandpass filters in exchange for larger temporal supports and more dense transform matrices (Mallat, 1999; Najmi, 2012).

The matrix is not inverted directly, but is rather factored using specialized packages like MATLAB's 'decomposition' function. The factors—usually LU factors—are stored, to be later used to efficiently solve a series of linear equations of the form $\widetilde{\boldsymbol{H}}^{-1}\boldsymbol{v} = \boldsymbol{w}$, where $\boldsymbol{v}$ and $\boldsymbol{w}$ are arbitrary vectors, without having to explicitly invert $\widetilde{\boldsymbol{H}}$. This is useful in the context of iterative methods for computing the SVD of $\widetilde{\boldsymbol{H}}^{-1}$. Though there are no sparsity guarantees for the factors, they still exhibit significant sparsity in practice.

For the SVD, we take advantage of the sparse precomputed factors of $\widetilde{\boldsymbol{H}}^{-1}$ and opt for an iterative method. In this work, we use a one-sided Lanczos bidiagonalisation (Simon & Zha, 2000), which additionally allows us to compute a truncated SVD and accurately estimate a number $q < 4N_2N_t$ of the most significant singular input and output modes. In practice, we find that $q = O(10^{1\sim 2})$ yields sufficiently converged leading modes for a system of size $4N_2N_t = O(10^{5\sim 6})$; truncating the SVD is thus an excellent cost-saving method.

Other efficient SVD algorithms rely on randomized approaches, in particular by sub-sampling the high-dimensional matrix and performing the SVD on the lower-dimensional approximation (Drineas & Mahoney, 2016; Halko et al., 2011; Tropp et al., 2017). Modifications of randomized SVD algorithms, notably randomized block Krylov methods (Musco & Musco, 2015), have been additionally developed for matrices with slow-decaying singular values, a property exhibited by the resolvent operator in Chapter 3.6. A randomized SVD of a high-dimensional discrete resolvent operator is used in Ribeiro et al. (2020) and Yeh et al. (2020).

Another option that would avoid the direct inversion of $\widetilde{\boldsymbol{H}}^{-1}$ involves taking the SVD of $\widetilde{\boldsymbol{H}}^{-1}$ first. The left and right singular vectors of $\widetilde{\boldsymbol{H}}^{-1}$ are respectively the right and left singular vector of $\widetilde{\boldsymbol{H}}$. However, since we are typically looking for the largest singular values of $\widetilde{\boldsymbol{H}}$ and their corresponding singular vectors, we would have to compute the full SVD of $\widetilde{\boldsymbol{H}}^{-1}$ to find its smallest singular values and corresponding singular vectors. Though this method avoids the inversion of $\widetilde{\boldsymbol{H}}^{-1}$, it does not preserve the efficiency gains of a (heavily) truncated SVD, and should only be used if the factorization of $\widetilde{\boldsymbol{H}}^{-1}$ remains the costliest operation. Suppose for example that $\tilde{\boldsymbol{H}}^{-1}$ has $n_{nz} \leq (4N_2N_t)^2$ non-zero elements, and that the LU-factorization of $\widetilde{\boldsymbol{H}}$ has at most $m_{nz} \leq (4N_2N_t)^2$ non-zero elements. Suppose that n_{nz} is small enough that the cost of the LU-factorization is small. A full iterative SVD of $\widetilde{\boldsymbol{H}}^{-1}$ has complexity $O(4N_2N_tn_{nz})$, whereas a q-truncated SVD of $\tilde{\boldsymbol{H}}$ has complexity $O(m_{nz}q)$. Thus, if $n_{nz}/m_{nz} < q/(4N_2N_t)$, it is more efficient to compute an SVD of $\tilde{\boldsymbol{H}}^{-1}$ without computing an LU-factorization. For the turbulent Stokes boundary layer problem considered in Chapter 3.6, $q = 400$ modes are calculated and $q/(4N_2N_t) \approx 0.001$. Using a second-order finite difference operator in time and Daubechies-8 wavelet transform, $n_{nz}/m_{nz} \approx 0.24$, making the factorization and truncated SVD method more efficient. In general, since we compute a heavily truncated SVD, $q/(4N_2N_t) << 1$ and we find that a factorization of the sparse system prior to the SVD is more advantageous.

Resolvent analysis can also be performed more efficiently for the windowed systems described in Chapter 3.2. Indeed, $\boldsymbol{B}\tilde{\boldsymbol{H}}\boldsymbol{C} = (\boldsymbol{B}^\dagger\tilde{\boldsymbol{H}}^{-1}\boldsymbol{C}^\dagger)^\dagger$, where the superscript $\dagger$ indicates the Moore-Penrose pseudoinverse. Rather than form the resolvent operator $\tilde{\boldsymbol{H}}$ first through an inversion, we can reduce the dimension of the system by windowing the linearized Navier-Stokes operator *prior* to taking the pseudoinverse of the windowed system. The matrix pseudoinversion and SVD would be applied to a lower-dimensional matrix of size defined by the non-zero block of $\boldsymbol{BC}$.

3.4 Convergence

When augmenting resolvent analysis with the additional temporal dimension, issues of robustness arise. Particular attention must be given to the choice of the discrete time differentiation operator $\boldsymbol{D}_t$. Using a sparse finite difference matrix for $\boldsymbol{D}_t$ is usually desirable, for it increases the sparsity of the resolvent operator and heavily reduces the memory and complexity cost of computing of the resolvent modes. However, it also distorts the time differentiation for high-frequency waves and can lead to SVD modes that do not converge to the correct structure, even when the resolution in time is increased.

To illustrate this, we study the spectra of two time-derivative matrices on a uniform grid of resolution N_t: $\boldsymbol{D}_{t,2}$, a second-order centered finite difference matrix, and $\boldsymbol{D}_{t,F}$, a Fourier derivative matrix. Suppose without loss of generality that N_t is even. The eigenvalues of the Fourier derivative matrix $\boldsymbol{D}_{t,F}$ are $\{\pm \mathrm{i}\omega_k\}$ for $k = 0, 1, ..., (N_t/2 - 1)$, where $\omega_k = 2\pi k/T$ represent the resolved frequencies. The eigenvalues of the second-order centered difference matrix $\boldsymbol{D}_{t,2}$ are $\{\pm \mathrm{i}\breve{\omega}_k\}$, where $\breve{\omega}_k = \sin(2\pi k/N_t)N_t/T$ represent the modified frequencies. The eigenvectors of both operators are the discrete Fourier modes. Frequencies ω_k and $\breve{\omega}_k$ are shown in Figure 3.4(a). We notice that $\breve{\omega}_k$ converges pointwise to ω_k as N_t increases, but not uniformly. Indeed, we note that, for a fixed k,

$$\lim_{N_t \to +\infty} \sin\left(\frac{2\pi k}{N_t}\right)\frac{N_t}{T} = \frac{2\pi k}{T}, \tag{3.23}$$

and our modified frequency converges to the correct value. Now consider the maximum $k = N_t/2 - 1$. The modified frequency can be Taylor-expanded about a small time step T/N_t as

$$\sin\left(\frac{2\pi}{N_t}\left(\frac{N_t}{2} - 1\right)\right)\frac{N_t}{T} = \frac{2\pi}{T} - \frac{4\pi^3}{3TN_t^2} + \ldots \tag{3.24}$$

The gap between the largest (correct) frequency $2\pi(N_t/2 - 1)/T$ and its modified counterpart thus grows as $O(N_t)$. Now consider an arbitrary matrix $\boldsymbol{A}$, which can represent the spatial portion of the linearized Navier-Stokes equations. The following approximation holds:

$$\begin{aligned}(\boldsymbol{D}_{t,2} + \boldsymbol{A})^{-1} &= (\boldsymbol{D}_{t,F} + \boldsymbol{A} + \boldsymbol{D}_{t,2} - \boldsymbol{D}_{t,F})^{-1} \\ &\approx (\boldsymbol{D}_{t,F} + \boldsymbol{A})^{-1} - (\boldsymbol{D}_{t,F} + \boldsymbol{A})^{-1}(\boldsymbol{D}_{t,2} - \boldsymbol{D}_{t,F})(\boldsymbol{D}_{t,F} + \boldsymbol{A})^{-1} + \ldots .\end{aligned} \tag{3.25}$$

Thus,

$$\|(\boldsymbol{D}_{t,2} + \boldsymbol{A})^{-1} - (\boldsymbol{D}_{t,F} + \boldsymbol{A})^{-1}\|_2 \leq O(N_t)\ \|(\boldsymbol{D}_{t,F} + \boldsymbol{A})^{-1}\|_2^2. \tag{3.26}$$

The lack of convergence as N_t increases suggests that the use of a finite difference operator rather than a Fourier derivative can significantly distort the SVD of the resolvent operator. The error between $D_{t,F}$ and $D_{t,2}$ is shown in Figure 3.4(b) to indeed grow as $O(N_t)$. To benefit from the advantages of a sparse temporal finite difference operator while avoiding spurious SVD modes, we propose using the windowing procedure described in Chapter 3.2 to filter-out the wavelet scales associated with the high-frequency frequencies more susceptible to distortion. Specifically, rather than choose the windowing matrices $\boldsymbol{B}$ and $\boldsymbol{C}$ to highlight a physically interesting range of the frequency spectrum, we use them to exclude the frequencies above a threshold $k_{\max} < N_t/2$. The maximum error between the eigenvalues of $\boldsymbol{D}_{t,2}$ and $\boldsymbol{D}_{t,F}$ is given by the Taylor expansion

$$\sin\left(\frac{2\pi k_{\max}}{N_t}\right)\frac{N_t}{T} - \frac{2\pi k_{\max}}{T} = \frac{4\pi^3 k_{\max}^3}{3N_t^2 T} + O\left(\frac{k_{\max}^5}{N_t^4}\right). \tag{3.27}$$

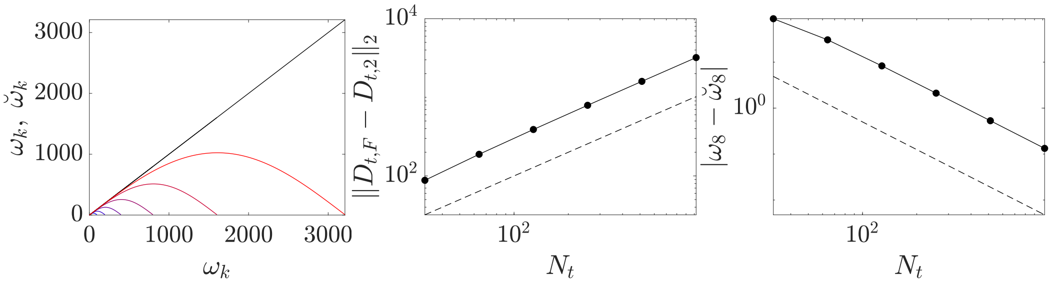

(a) (b) (c)

Figure 3.4: (a) Exact (black) and modified (colored) frequencies for N_t = 32, 64, 128, 256, 512, 1024. The colors range from blue, which corresponds to the lowest N_t, to red, which corresponds to the highest N_t; (b) operator error between the Fourier derivative matrix and the second-order-accurate centered finite difference matrix (●–); (c) Error between the eighth exact and modified frequencies (●–). The dashed lines in (b) and (c) represent trend lines of slope N_t^2, and $1/N_t^2$ respectively.

Thus, assuming the chosen wavelet transform $\boldsymbol{W}$ is unitary,

$$\|\boldsymbol{B}\boldsymbol{W}\left(\boldsymbol{D}_{t,2}+\boldsymbol{A})^{-1}-(\boldsymbol{D}_{t,F}+\boldsymbol{A})^{-1}\right)\boldsymbol{W}^{-1}\boldsymbol{C}\|_2 \leq O\left(\frac{k_{\max}^3}{N_t^2}\right)\ \|(\boldsymbol{D}_{t,F}+\boldsymbol{A})^{-1}\|_2^2. \tag{3.28}$$

The error between the SVD of the two operators decreases as $1/N_t^2$ provided $k_{\max}$ remains fixed. We confirm the trend of the pointwise error between $D_{t,F}$ and $D_{t,2}$ Figure 3.4(c). In Chapter 3.6, we employ this filtering approach.

3.5 Validation I: channel flow

We now validate wavelet-based resolvent analysis against traditional Fourier-based resolvent analysis by applying both methods to turbulent channel flow, which is statistically stationary. Wavelet-based resolvent analysis is equivalent to simultaneously conducting the Fourier-based resolvent analysis for each frequency that is resolved by the chosen temporal grid. The leading time-Fourier-transformed wavelet-based modes indeed have only one non-zero Fourier component, which is shown to be equivalent to the principal Fourier-based mode corresponding to the same frequency.

When the mean velocity and shear profiles are constant, the elements of $\boldsymbol{U}_i$ and $\boldsymbol{dU}_{i,j}$ corresponding to the same spatial point are the same across all temporal grid points. This means that $\widetilde{\boldsymbol{U}_i} = \boldsymbol{W}\boldsymbol{U}_i\boldsymbol{W}^{-1} = \boldsymbol{U}_i$ and $\widetilde{\boldsymbol{dU}_{i,j}} = \boldsymbol{W}\boldsymbol{dU}_{i,j}\boldsymbol{W}^{-1} = \boldsymbol{dU}_{i,j}$. In

Case	Section	L^*	u^*
Channel flow	§3.5	δ^* (channel half-height)	u_τ^* (friction velocity)
Turbulent Stokes boundary layer	§3.6	δ_Ω^* (laminar boundary layer thickness)	$U_{\max}^*$ (max wall velocity)

Table 3.1: Length and velocity used to non-dimensionalize the Navier-Stokes equations for each case considered in this work.

such cases, the discretized and transformed equations used to construct the wavelet-based and harmonic resolvent operators (equations (3.16) and (2.18)) only differ by their respective time differentiation matrices, $\widetilde{\boldsymbol{D}_t}$, described in Chapter 3.2, and $\widehat{\boldsymbol{D}}_{t,F}$, the diagonal matrix with diagonal terms $(\widehat{\boldsymbol{D}}_{t,F})_{\ell\ell} = -\mathrm{i}\omega_\ell = \mathrm{i}(2\pi\ell)/T$ for $\ell = -N_t/2, \cdots, N_t/2-1$. Denoting the Fourier transform in time as $\boldsymbol{F}$, the time derivative matrices satisfy $\boldsymbol{W}^{-1}\widetilde{\boldsymbol{D}_t}\boldsymbol{W} = \boldsymbol{F}^{-1}\widehat{\boldsymbol{D}}_{t,F}\boldsymbol{F} = \boldsymbol{D}_t$. The SVD is unique up to multiplication by a unitary matrix, and provided that we use a unitary wavelet transform, we expect the singular values of $\widetilde{\boldsymbol{H}}^{(k_1,k_3)}$ to be the same as those for

$$\widehat{\boldsymbol{H}}^{(k_1,k_3)} = \begin{pmatrix} \widehat{\boldsymbol{H}}^{(k_1,k_3,\omega_1)} & & & \\ & \widehat{\boldsymbol{H}}^{(k_1,k_3,\omega_2)} & & \\ & & \widehat{\boldsymbol{H}}^{(k_1,k_3,\omega_3)} & \\ & & & \ddots \end{pmatrix}, \tag{3.29}$$

where each $\widehat{\boldsymbol{H}}^{(k_1,k_2,\omega_\ell)}$ is defined according to equation (2.6). This is also equivalent to the harmonic resolvent operator (Chapter 2.2) with $\Omega = \{(2\pi\ell)/T\}_{\ell=0}^{N_t/2-1}$ Moreover, we expect the response and forcing modes of both systems to be related by the unitary transform given by the Fourier and inverse-wavelet transform in time, $\boldsymbol{F}\boldsymbol{W}^{-1}$. For the Fourier-based approach, we produce the modes of $\widehat{\boldsymbol{H}}^{(k_1,k_3)}$ by computing the SVD of each $\widehat{\boldsymbol{H}}^{(k_1,k_3,\omega_\ell)}$ independently for every ω_ℓ, as the time scales of the non-stationary formulation are decoupled. Under the wavelet-based formulation, the SVD of the full operator, which includes all resolved frequencies, must be computed.

The flow variables are non-dimensionalized using the channel half-height δ^* and the friction velocity u_τ^* so that $Re = Re_\tau$. The non-dimensionalization parameters are shown in Table 3.1. We obtain the mean profile of turbulent channel flow at friction Reynolds number $Re_\tau \approx 186$ from Bae and Lee (2021), as in Chapter 2.1.

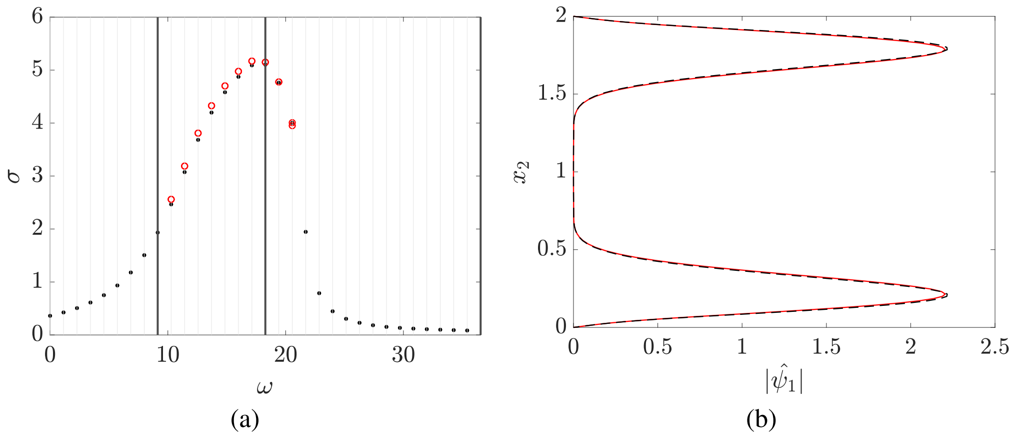

Figure 3.5: (a) First 10 singular values for the wavelet-based resolvent (red) and the largest singular value of the Fourier-based resolvent operator (black) computed for each ω_ℓ. The vertical gray lines indicate the frequencies resolved by the chosen temporal grid, and the vertical black lines delimit the frequency band covered by each of the wavelet scales used in the wavelet expansion. (b) Magnitude of the streamwise component of the principal resolvent mode corresponding to $\omega \approx 17.14$. The red line represents the nonzero Fourier coefficient of $\boldsymbol{F}\breve{\boldsymbol{\psi}}_1$—the principal wavelet-based resolvent response mode after a Fourier transformation in time—and the black line represents $\hat{\boldsymbol{\psi}}_1$—the principal response mode obtained from traditional Fourier-based resolvent analysis. The mode $\boldsymbol{F}\breve{\boldsymbol{\psi}}_1$ is only composed of one nonzero Fourier coefficient corresponding to $\omega \approx 17.14$; for both methods, $\lambda_1^+ = 1000$ and $\lambda_3^+ = 100$.

The computational details of the DNS are described in Chapter 2.1 and in Bae and Lee (2021). We note that $\boldsymbol{U}_3$, $\boldsymbol{U}_2$, $\boldsymbol{dU}_{2,2}$, and $\boldsymbol{dU}_{3,2}$ are zero due to the absence of a spanwise and wall-normal contribution to the mean velocity profile.

For both the Fourier- and wavelet-based resolvent analyses, the wall-normal direction is discretized using a Chebyshev collocation method using $N_2 = 128$, and the mean streamwise velocity profile and its wall-normal derivative from the DNS are interpolated to the Chebyshev collocation points. For the wavelet-based resolvent analysis, we uniformly discretize the temporal domain, $[0, T)$, where $T = 5.5$ ($T^+ = 1023$), with a temporal resolution of $N_t = 128$. The superscript $(\cdot)^+$ denotes wall units, which are defined to be $(\cdot)^+ := (\cdot)Re_\tau$ for length and time scales and $(\cdot)^+ := (\cdot)$ for velocity scales. The matrices $\boldsymbol{U}_1$ and $\boldsymbol{dU}_{1,2}$ are constructed by repeating the values of U_1 and dU_1/dx_2 at every temporal grid point.

We impose periodic boundary conditions at the edges of the time window. These temporal boundary conditions are encoded in the choice of time differentiation matrix $\boldsymbol{D}_t$, which we choose to be a Fourier differentiation matrix $\boldsymbol{F}^{-1}\widehat{\boldsymbol{D}}_{t,F}\boldsymbol{F}$. For spatial derivatives in the wall-normal direction, we use first- and second-order Chebyshev differentiation matrices, and impose no-slip and no-penetration boundary conditions at the wall. In choosing k_1 and k_3, we target spanwise and streamwise wavelengths of $\lambda_1^+ \approx 1000$ and $\lambda_3^+ \approx 100$ in wall units, which are the typical length scales for near-wall streaks and correspond to the peaks in the streamwise spectrum.

For our wavelet transform, we choose a two-stage ($L = 2$) Shannon wavelet transform, *i.e.* the state vectors in the resulting system described by equation (3.17) contain terms covering the following three intervals in frequency domain: $N_t/4[-\pi, \pi]$ and $N_t/2^\ell[-2\pi, -\pi] \cup [-2\pi, -\pi]$ for $\ell = 1,\ 2$. We note that, for this application, the resolvent modes converge despite the relatively low dimension of the resolvent operator. This permits us to use the aforementioned dense differentiation matrices. Sparse finite difference matrices may be used in higher-dimensional problems to improve efficiency. The results for the Fourier-based cases were computed by applying traditional resolvent analysis using $\omega_\ell = 2\pi\ell/T$ for $\ell = 0, \ldots, , N_t/2$ to capture all the frequencies resolved by our temporal grid, while the wavelet-based resolvent modes were computed by solving the full space-time system at once. We consider the results from wavelet-based resolvent analysis to be converged: the singular values obtained for $(N_t, N_2) = (128, 128)$, and for $(N_t, N_2) = (64, 128)$ produced the same leading singular values. These are not shown in this work. As implied by equation (3.29), a single wavelet-based resolvent analysis would yield the modes corresponding to all time scales captured by the temporal grid.

In Figure 3.5(a), we show the 10 leading singular values of the wavelet-based resolvent operator, along with the first singular value for the Fourier-based operator for each frequency parameter ω_ℓ. In order to associate the singular values obtained from the wavelet-based method with their frequencies, we Fourier-transform each wavelet-based response mode in time, and identify the index of the non-zero component. The first 10 singular values obtained differ by at most 3%, with the largest differing by 1.3%, which matches our expectation. The discrepancy can be explained by numerical and truncation errors. Though Shannon wavelet transforms are unitary in the continuous setting, Shannon wavelets do not have compact support in time. The discrete Shannon transform is thus not a unitary matrix due to the truncation of the wavelet in time, and exhibits a condition number of approximately 1.6 in this case. Using wavelets that are compactly supported in time, such as the Daubechies wavelets, reduces the discrepancy, as the resulting wavelet transform matrix $\boldsymbol{W}$ is a unitary operator with a condition number of 1 that better preserves the singular values of $\widehat{\boldsymbol{H}}^{(k_1,k_3)}$. Increasing the time resolution also reduces the gap between the singular values. Due to the symmetry of the domain about the centerline, the singular values appear in equal pairs (McKeon & Sharma, 2010), which is only visible in Figure 3.5(a) for $\omega = 20.56$, where the pair of singular values deviate slightly for each other due to numerical error. This property is discussed in more detail in Chapter 2.1: the modes corresponding to the pair of equal singular values form two-dimensional singular forcing and response planes, which respectively contain the combined effect of the forcing and response on the two channel halves. In other words, the two sister modes can be linearly combined to isolate the forcing or response in one of the channel halves.

In figure 3.5(b), we compare the two methods further by plotting the streamwise component of the most amplified resolvent response mode that they each produce. For the Fourier-based method, this corresponds to the frequency $\omega \approx 17.14$. For the wavelet-based method, we first Fourier-transform the principal mode in time, and though not shown, observe that the Fourier modes associated with $\omega \approx 17.14$ is the only non-zero component. This matches our expectation that the wavelet-based resolvent analysis is, in this case, equivalent to performing the traditional Fourier-based resolvent analysis for each frequency ω_ℓ independently, and that each SVD mode corresponds to an individual ω_ℓ. Figure 3.5(b) shows that the modes from the two methods match. Despite the slight discrepancy in the singular values, both methods yield the same resolvent modes associated with the maximum singular value.

Although not shown, the streamwise component of the modes dominate for the principal modes computed with the two methods, and the modes form alternating low- and high-speed streamwise streaks. The principal forcing mode is in the form of streamwise rolls, with a negligible streamwise component. The shape of the modes is thus in line with the previous analysis of the self-sustaining process of wall turbulence (Bae et al., 2021; Farrell et al., 2017; Hamilton et al., 1995; Jiménez & Moin, 1991; Jiménez & Pinelli, 1999; Schoppa & Hussain, 2002; Waleffe, 1997). Additionally, resolvent response modes, both formulated traditionally and using the wavelet basis in time, peak at the critical layer located where $U(x_2) = \omega/k_1$, at $x_2^+ \approx 40$.

The results presented in this section confirm the validity of the wavelet-based formulation. As expected, it produces the same response and forcing modes as traditional resolvent analysis. For each wall-normal height, the wavelet-based modes are

Fourier modes in time, despite us not having imposed this shape restriction upon formulating the wavelet-based resolvent operator. For this problem, traditional Fourier-based resolvent analysis is obviously more efficient, since it decouples the time scales: inverting and decomposing a $4N_2 \times 4N_2$-sized matrix N_t times is cheaper than inverting and decomposing a $4N_2N_t \times 4N_2N_t$-sized matrix once. Wavelet-based resolvent analysis is indeed destined to study problems to which traditional (and harmonic) Fourier-based resolvent analysis are not applicable. But before tackling such problems, we validate our method against harmonic resolvent analysis, which we present in the following section.

3.6 Validation II: turbulent Stokes boundary layer

Here, we apply both wavelet-based and harmonic resolvent analyses to a problem with a time-periodic mean velocity and shear: the Stokes turbulent boundary layer. In light of the results of the previous section, this may seem redundant, but this validation step led us to key insights on the convergence properties of the wavelet-based resolvent operator. In particular, the frequency content of the computed modes becomes distorted if a finite difference operator in time is used to construct the resolvent operator (Chapter 3.4). Using dense but accurate derivatives, such as the Fourier derivative matrix in time, is one solution. However, in our attempt to develop an efficient implementation of wavelet-based resolvent analysis, we insist on the use of sparse operators, which greatly reduces the costs of computation and storage. For high-dimensional problems where the forcing and response states must encode temporal and spatial information at sufficient resolutions, this advantage is key. In Chapter 3.2, we proposed a solution that is compatible with a sparse formulations of the resolvent operator: filtering-out high frequency content using wavelet windowing matrices. The results of section demonstrate the validity of this approach.

To generate the mean profile and second-order statistics, the Stokes boundary layer is first simulated through a channel flow with the lower and upper walls oscillating in tandem at a velocity of $U_w^*(t) = U_{\max}^* \cos(\Omega^* t^*)$ with no imposed pressure gradient. We non-dimensionalize velocities by $U_{\max}^*$ and lengths by $\delta_\Omega^* := \sqrt{2\nu^*/\Omega^*}$, which defines the laminar Stokes boundary layer thickness. Though time and frequency are both non-dimensionalized with $U_{\max}^*$ and δ_Ω^*, we use $t\Omega$ as our preferred time variable—where Ω denotes the non-dimensionalized wall oscillation frequency—for a clearer comparison with the period, and ω/Ω as our preferred frequency variable as it represents temporal wave number. The relevant non-dimensional number is

$Re_\Omega = U^*_{\max}\delta^*_\Omega/\nu^*$. For the current case, we consider $Re_\Omega = 1500$, which lies within the intermittently turbulent regime (Akhavan et al., 1991; Costamagna et al., 2003; Hino et al., 1976; Verzicco & Vittori, 1996; Vittori & Verzicco, 1998). This problem has been well-studied numerically and experimentally (Akhavan et al., 1991; Blondeaux & Vittori, 1994; Carstensen et al., 2010; Costamagna et al., 2003; Hino et al., 1976; Jensen et al., 1989; Ozdemir et al., 2014; Sarpkaya, 1993; Spalart & Baldwin, 1989; Verzicco & Vittori, 1996; Vittori & Verzicco, 1998; Von Kerczek & Davis, 1974).

The DNS uses a second-order staggered finite-difference (Orlandi, 2000) and a fractional-step method (J. Kim & Moin, 1985) with a third-order Runge-Kutta time-advancing scheme (Wray, 1990). Periodic boundary conditions are imposed in the streamwise and spanwise directions, while the no-slip and no-penetration are imposed at the top and bottom walls. The code has been validated in previous studies in turbulent channel flows (Bae et al., 2018, 2019; Lozano-Durán & Bae, 2019) and flat-plate boundary layers (Lozano-Durán et al., 2018), though we note that, for this problem, we modify the boundary conditions to accommodate the oscillating walls. The domain size of the channel for the DNS is given by $6\pi \times 80 \times 3\pi$. The domain is discretized uniformly in the x_1- and x_3-directions using 64 points, which corresponds to non-dimensionalized spacings of $\Delta x \approx 0.29$ and $\Delta x_3 \approx 0.15$. For the x_2-direction, we use a hyperbolic tangent grid with 385 points, resulting in $\min(\Delta x_2) \approx 0.01$ and $\max(\Delta x_2) \approx 0.91$. We compute the mean velocity profiles by averaging in homogeneous directions and phase. Figure 3.6 shows the mean and the streamwise root-mean-square (rms) velocity profiles at different times. We note that $U_1(t\Omega + \pi) = -U(t\Omega)$ and $U_{i,rms}(t\Omega + \pi) = U_{i,rms}(t\Omega)$. The turbulent energy peak occurs near the wall at $x_2 = 1.43$ and $t\Omega = 2.65$, and propagates away from the wall thereafter.

To construct the resolvent operator, we first choose the spatial scales for the homogeneous directions. Using the DNS data, we calculate the streamwise energy spectrum at $x_2 = 1.43$ and $t\Omega = 2.65$, the wall-normal location and phase of the peak $U_{1,rms}$. The most energetic streamwise and spanwise scales at that location are $k_1 = 0.67$ and $k_3 = 4.22$, which we choose as the spatial Fourier parameters for the resolvent operator. For the remaining dimensions, we use a Chebyshev grid of size $N_2 = 80$ in the wall-normal direction that extends from $x_2 == 0$ (the bottom wall) to $x_2 = 40$ (the centerline) and a uniform temporal grid of size $N_t = 1600$ over the time domain, chosen to be $[0, T\Omega]$ where $T\Omega = 2\pi$ (*i.e.* one period). The mean

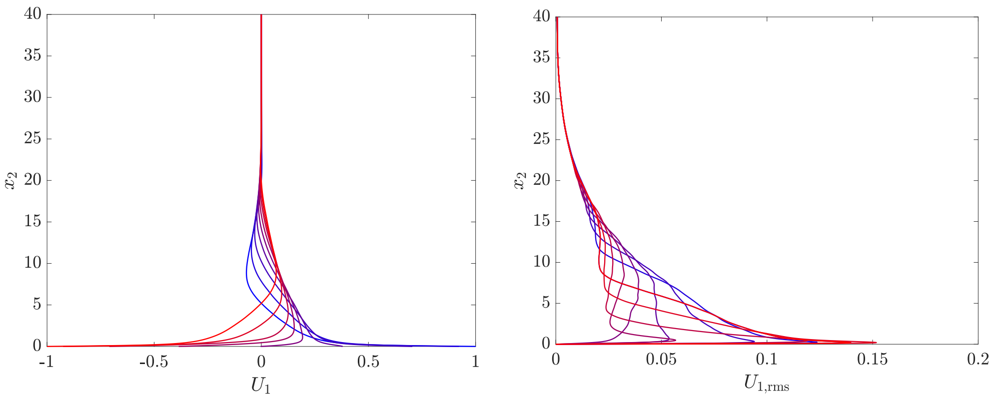

(a) (b)

Figure 3.6: (a) Mean streamwise velocity profile and (b) streamwise r.m.s. velocity from $t\Omega = 0$ (blue) to $t\Omega = \pi$ (red). The profiles shown are at $t\Omega = n\pi/8$, $n = 0, 1, \ldots 8$.

velocity and shear profiles are projected onto this new grid by interpolation. As in the previous section, $\boldsymbol{U}_3$, $\boldsymbol{U}_2$, $\boldsymbol{dU}_{2,2}$, and $\boldsymbol{dU}_{3,2}$ are zero.

We choose the time derivative matrix $\boldsymbol{D}_t$ and the wall-normal spatial derivative matrices to be second-order-accurate centered finite difference matrices. We enforce a no-slip and no-penetration boundary condition at the wall, a free-slip and no-penetration boundary condition at the centerline, and periodic boundary conditions at the start and end of the time domain.

Because $\boldsymbol{D}_t$ is a finite difference matrix rather than a Fourier differentiation matrix, we must implement a filtering step, detailed in Chapter 3.4, to exclude the high temporal wavenumbers. To apply this filtering step, we must assume that the high-frequency waves are not physically significant for the turbulent Stokes boundary layer problem. We use a two-stage Daubechies-16 wavelet transform, which is a sparse unitary operator. We note that the Daubechies-16 operator is not a perfect bandpass filter, and the numerical filtering operation simply attenuates the high-frequency waves that produce spurious SVD modes instead of excluding them outright. Nevertheless, due to the high dimensionality of the problem, it remains advantageous to use sparse transforms. We choose to constrain the forcing and response modes to the scaling functions and their shifts, which roughly cover the first quarter of all temporal wavenumbers $\omega/\Omega = 0\ldots, N_t/8$.

We compare the results obtained with the wavelet-based resolvent modes with the results from harmonic resolvent analysis (Padovan et al., 2020). The latter is similar

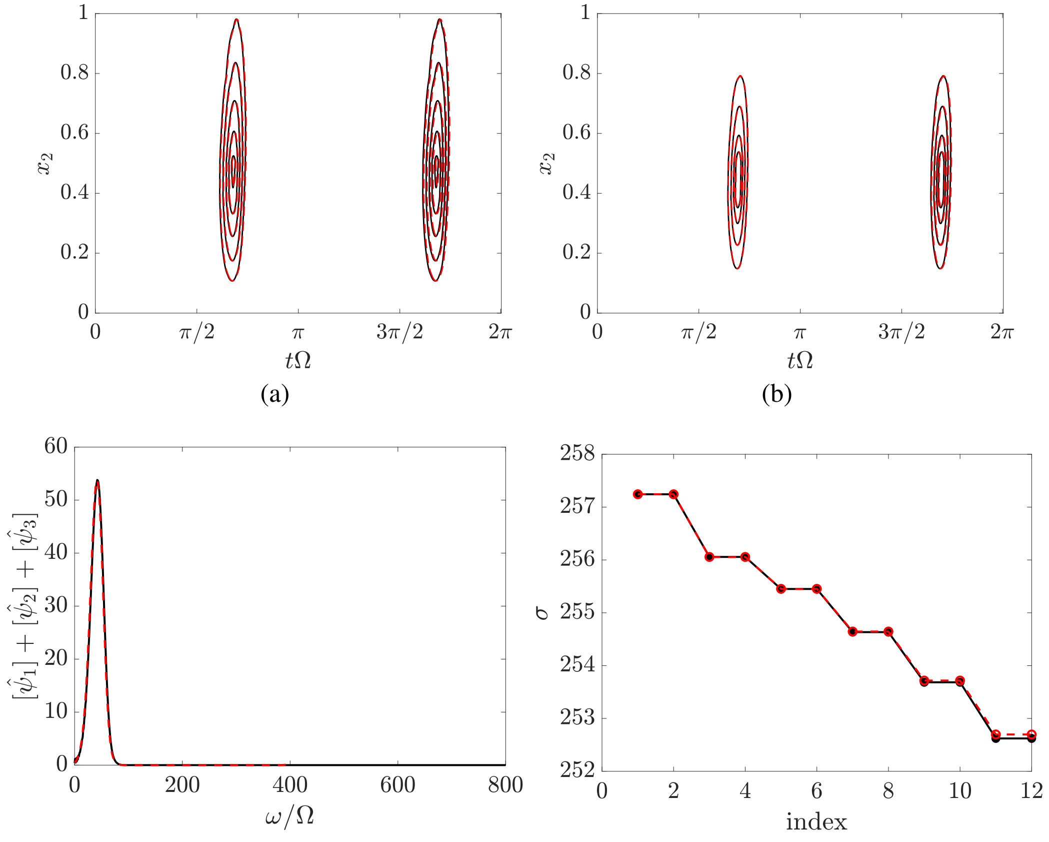

(a) (b)

(c) (d)

Figure 3.7: Magnitude contours (25%, 50%, 75%, and 90% of the maximum value) of (a) the wall-normal component of the principal resolvent forcing mode and (b) the streamwise component of the principal resolvent response mode for the turbulent Stokes boundary layer; (c) x_2–integrated Fourier spectrum in time for the principal response modes; (d) singular values from the SVD of the resolvent operators. Results from harmonic resolvent analysis are shown in red, and those from wavelet-based resolvent analysis in black.

to a combined Fourier-based resolvent analysis for multiple frequencies, and includes the interactions between them; the frequencies are indeed coupled by the time-varying mean profile (see Chapter 2.2 for more detail). For the harmonic resolvent analysis, we use the same Chebyshev grid as in the wavelet-based method, with $N_2 = 80$. For the sake of comparing with the wavelet-based method and to account for the filtering step, we choose a frequency resolution of $N_t = 1600/4 = 400$. We expect the two methods to produce similar singular values and modes. The singular values and modes would be equivalent in both cases if we use a Fourier differentiation operator for the wavelet-based method as in Chapter 3.5.

The modes obtained from harmonic resolvent analysis agree well with those obtained from wavelet-based resolvent analysis. They occur at the same x_2 location, and time (Figures 3.7(a, b)), and exhibit roughly the same frequency content (Figure 3.7(c)). Moreover, the SVD of the wavelet-based and harmonic resolvent operators yield similar singular values. The first twenty singular values are shown in Figure 3.7(d). Despite Daubechies-16 wavelets being imperfect bandpass filters, filtering-out high-frequency waves using the sparse wavelet transform succeeds in producing resolvent modes that match the leading modes from harmonic resolvent analysis. We consider that the results for harmonic resolvent analysis shown in Figure 3.7 are converged: the ones that use a coarser grid with $N_2 = 80$ and $N_t = 300$ produced the same 10 leading singular values up to 10^{-4}. Despite the larger dimension of the wavelet-based system, the windowed wavelet-based resolvent operator can be computed efficiently due its significant sparsity. Indeed, the harmonic and wavelet-based resolvent analyses run in similar wall times.

The principal input and output modes corresponding to the chosen spatial scales and boundary conditions in time are shown in Figure 3.8(a). We observe that the modes are located at roughly the same wall normal height as the peaks in $U_{1,rms}$, *i.e.* $x_2 \approx 0.5$. We also observe that the principal input and output modes are synchronized with the peaks in $U_{1,rms}$, though the modes tend to peak slightly earlier than $U_{1,rms}$. This suggests that linear amplification might provoke the transition to turbulence. The results presented in Figure 3.8 suggest that the study of energy amplification in the Stokes boundary layer is a good candidate for the use of linearized methods, similarly to the turbulent channel flow (Jiménez, 2013).

We also observe that the principal input mode precedes the principal output mode in time, with the peak of the former occurring $\Delta t\Omega \approx 0.063$ before the peak of the latter. Wavelet-based resolvent analysis is able to capture the natural response time

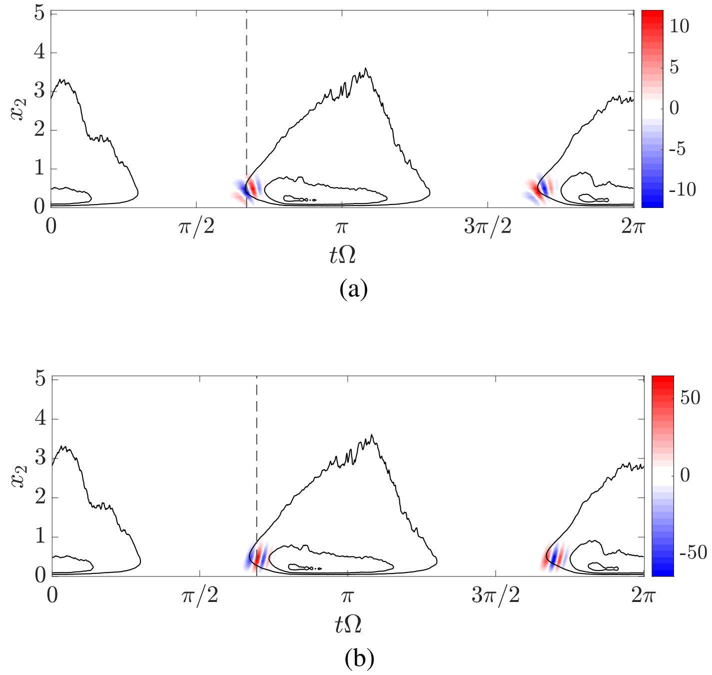

Figure 3.8: Real part of (a) $\breve{\phi}_1$, and (b) $\breve{\psi}_1$ for the turbulent Stokes boundary layer. The black contour lines are $U_{1,rms}$ with the levels indicating $50\%, 75\%, 95\%$ of its maximum value. The vertical dashed lines show the times of the amplitude peak for the input mode ($t\Omega = 2.11$) and output mode ($t\Omega = 2.18$).

between forcing and response terms under the dynamics of the linearized Navier-Stokes equations. This time delay is also in line with a physical interpretation of the modes in which the input modes cause the output modes and must thus occur earlier. In future works, it would be interesting to project flow fields onto these time-separated resolvent forcing and response modes to test whether better correlations can be obtained between them in the transformed bases.

Because of the windowing step described above, we expect the wavelet coefficients of the modes corresponding to the three highest bands of frequencies to be zero, which is confirmed in the scalograms in Figures 3.9(a). We also see in Figure 3.9(a) that the frequency content of the principal modes varies with time. The principal forcing mode is initially composed of lower-frequency waves, whose frequencies are centered in a band $[0, 25\Omega]$; these waves are gradually shifted up to frequencies centered in $[25\Omega, 50\Omega]$. Likewise, the waves composing the principal response mode, initially at frequencies centered in $[25\Omega, 50\Omega]$ are also shifted up to higher frequencies. We propose that this frequency shift is due to the time-varying mean

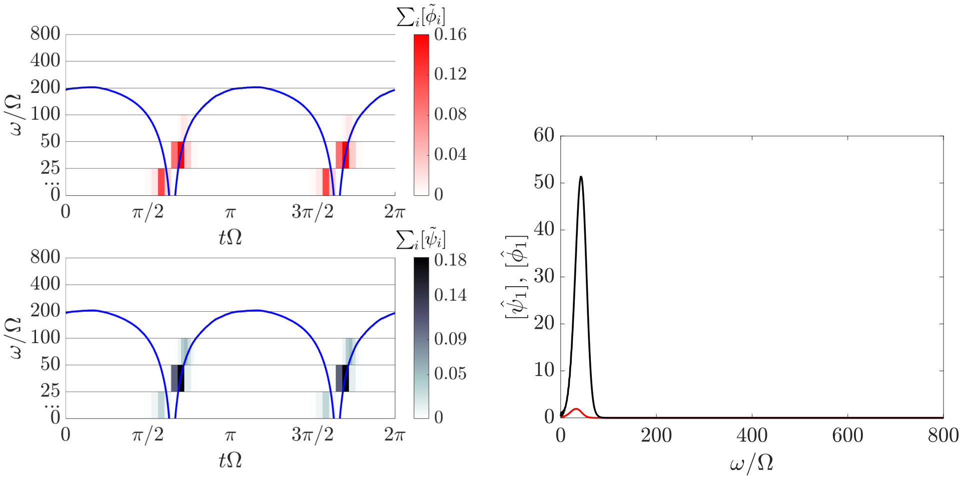

(a)

(b)

Figure 3.9: (a) Principal forcing (red, top panel) and response (black, bottom panel) modes in the time-frequency plane; the blue line indicates $U_1 k_1/\Omega$ at $x_{2,\text{avg}}^{\text{resp.}} = x_{2,\text{avg}}^{\text{forc.}} \approx 0.46$; (b) x_2–integrated frequency content in the streamwise component of the forcing (red) and response (black) modes.

streamwise velocity U_1, which acts as a convection velocity and accelerates the resolvent forcing and response waves. Thus, we expect the frequency content of the forcing and response modes to vary in tandem with the changing mean streamwise velocity profile. We define the average location of the streamwise modes as

$$x_{2,\text{avg}}^{\text{resp.}} := \frac{\int_0^T \int_0^1 x_2 |\breve{\psi}_1|^2 dx_2 dt}{\int_0^T \int_0^1 |\breve{\psi}_1|^2 dx_2 dt}, \tag{3.30}$$

and

$$x_{2,\text{avg}}^{\text{forc.}} := \frac{\int_0^T \int_0^1 x_2 |\breve{\phi}_1|^2 dx_2 dt}{\int_0^T \int_0^1 |\breve{\phi}_1|^2 dx_2 dt}, \tag{3.31}$$

and plot the frequency shift due to the mean convection $U_1 k_1/\Omega$ at the average mode locations in Figure 3.9(a). We observe a good correlation between the shift in the frequency content of the forcing and response modes and the change in the mean velocity.

In addition to the frequency shifts occurring within the forcing and response modes individually, the changing mean velocity profile explains the frequency content difference between the forcing and response modes. This is due to the lag of the response with respect to the forcing. Since the modes occur at difference phases of the oscillating mean profile, they are convected at different velocities. To verify this, we first Fourier-transform $\breve{\boldsymbol{\phi}}$ and $\breve{\boldsymbol{\psi}}$ in time to extract their frequency content with better precision, and observe in Figure 3.9(b) that the average frequency shift between the forcing and response modes is

$$\Delta\omega := \frac{\int_0^{\Omega N t/2} \omega[\hat{\psi}_1] d\omega}{\int_0^{\Omega N t/2} [\hat{\psi}_1] d\omega} - \frac{\int_0^{\Omega N t/2} \omega[\hat{\phi}_1] d\omega}{\int_0^{\Omega N t/2} [\hat{\phi}_1] d\omega} \approx 10.2\ \Omega. \tag{3.32}$$

We then define the average temporal location of the modes as

$$t_{\text{avg}}^{\text{resp.}} := \frac{\int_0^T t[\breve{\psi}_1] dt}{\int_0^T [\breve{\psi}_1] dt}, \tag{3.33}$$

and

$$t_{\text{avg}}^{\text{forc.}} := \frac{\int_0^T t[\breve{\phi}_1] dt}{\int_0^T \int_0^1 [\breve{\phi}_1] dt}. \tag{3.34}$$

Assuming that both the optimal forcing and response prefer the same natural frequency ω_0 with a corresponding streamwise wave speed $c_0 = \omega_0/k_1$, we estimate the shift with

$$\left(|U(x_{2,\text{avg}}^{\text{resp.}}, t_{\text{avg}}^{\text{resp.}})| - |U(x_{2,\text{avg}}^{\text{forc.}}, t_{\text{avg}}^{\text{forc.}}|) \right) k_1/\Omega \approx 10.5, \tag{3.35}$$

which roughly matches the observed shift. We repeat this analysis for two other sets of spatial parameters, $(k_1, k_3) = (0.67, 2.67)$ and $(k_1, k_3) = (1.33, 2.67)$, though the plots are not shown. For the first set, the estimated frequency shift is found to be $\Delta\omega/\Omega \approx 27$ using equation (3.35), roughly matching the measured mean frequency shift of $\Delta\omega/\Omega \approx 26$ computed using a Fourier transform of the response and forcing modes. Similarly, for the second set of these length scales, the estimated frequency shift due to convection by the mean flow is $\Delta\omega/\Omega \approx 14.6$ and the measured mean frequency shift is $\Delta\omega/\Omega \approx 13.4$.

Wavelet-based resolvent analysis and harmonic resolvent analysis agree for the Stokes boundary layer problem. By filtering out the high frequencies, the windowing step solves issues of numerical distortion introduced by the use of finite difference operators in time. The optimal forcing and response modes are close in both space and time to the peaks of streamwise r.m.s. velocity, which hints at the role that linear amplification mechanisms are playing in determining the behavior of turbulence for this system. Both methods reveal how a time-varying mean profile affects the linear amplification of perturbations. The mean velocity profile not only determines the spatial structure of the modes as in Chapter 2.1, but also their transient behavior, in this case acting as a convection velocity that modulates the optimal forcing and response wave speeds.

Though the two methods are equivalent in the application above, wavelet-based resolvent analysis possesses additional qualities. In particular, the wavelet-based formulation makes time-localized analyses much wieldier. The windowing framework, used here to filter out the frequencies prone to numerical distortion, can just as well be used to focus on time intervals of interest, such as the relaminarization portion of the oscillation cycle, with the hope that time-localized changes in the energy amplification mechanisms would explain these other aspects of the turbulence. Unfortunately, this use case is not explored in this work. In the next chapters, we do, however, apply wavelet-based resolvent analysis to other problems to which Fourier-based methods are not suited, and use it to shed light on key transient phenomena observed in wall-bounded turbulence.

Chapter 4

APPLICATION I – ANALYSIS OF CANONICAL FLOWS

In this chapter, we apply wavelet-based resolvent analysis to flows that were previously not amenable to traditional Fourier-based methods. In Chapter 4.1, we revisit channel flow, and though the mean velocity and shear profiles do not vary in time, we apply the windowed wavelet-based framework to study transient bursting phenomena believed to trigger turbulence in the fully nonlinear system. In Chapter 4.2, the mean profile is obtained from channel flow subjected to a sudden, sustained spanwise pressure gradient; the mean velocity and shear respond by gradually developing spanwise components as time progresses. Wavelet-based resolvent analysis reveals new insights on how changing flow conditions modulate energy amplification mechanisms of perturbations, which in turn sheds light on the time-varying statistics of the turbulent flow. The systems considered in this chapter are all non-dimensionalized and the non-dimensionalization scales are shown in Table 4.1.

4.1 Bursting in channel flow

The added advantage of wavelet-based resolvent analysis lies in its ability to preserve temporal localization. The states in equation (3.21) encode time and frequency information, which allows us to study transient problems even when the mean profile is statistically stationary. One such transient phenomenon is the Orr mechanism, a linear mechanism first described by Orr (1907) that has been proposed to explain

Case	Section	L^*	u^*
Bursting in channel flow	§4.1	δ^* (channel half-height)	u_τ^* (friction velocity)
Channel flow with spanwise pressure gradient	§4.2	δ^* (channel half-height)	$u_{\tau,0}^*$ (friction velocity at $t = 0$)

Table 4.1: Length and velocity used to non-dimensionalize the Navier-Stokes equations for each case considered in Chapter 4

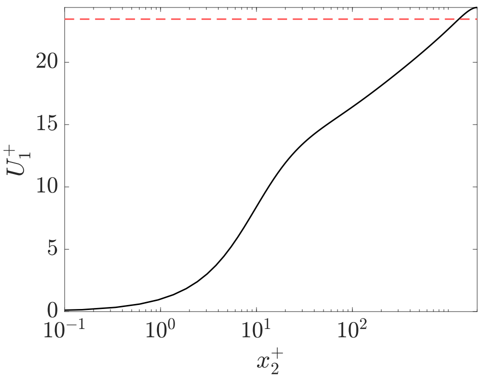

Figure 4.1: Mean streamwise velocity profile for channel flow at $Re_\tau = 2000$. The dashed line corresponds to the upper bound of the frequency band covered by the chosen wavelet, mapped to streamwise velocities using $U_1 = \omega/k_1$.

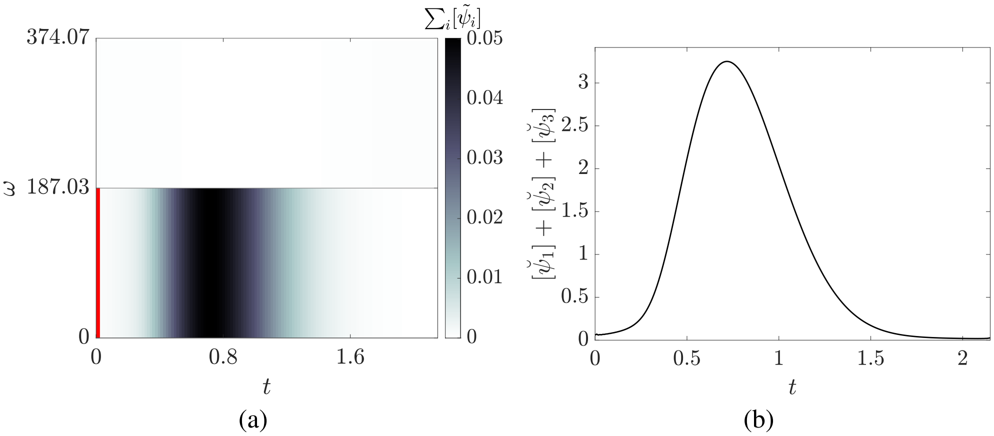

Figure 4.2: (a) Inverse wavelet-transformed principal response mode for channel flow at $Re_\tau = 2000$ and $k_1 = k_3 \approx 8.98$ under windowed forcing, in the frequency–time plane. The forcing window is highlighted in red. (b) x_2-integrated total energy of the inverse wavelet-transformed principal response mode.

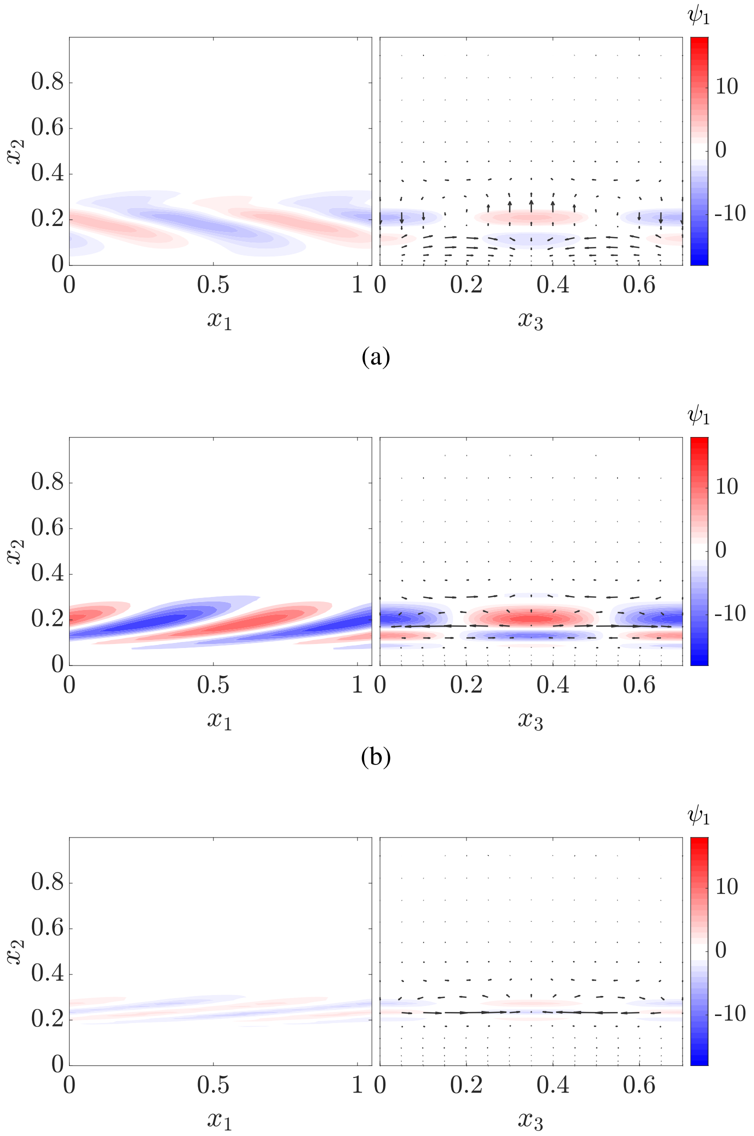

(a)

(b)

(c)

Figure 4.3: Principal response mode for the channel flow at $Re_\tau = 2000$ and $k_1 = k_3 \approx 8.98$ under transient forcing. The modes are shown at (a) $t = 0.25$, (b) $t = 0.71$, and (c) $t = 1.56$. The left and right panels respectively correspond to half-wavelength locations of $x_3/\delta = \pi/k_3\delta$ and $x_1/\delta = \pi/k_1\delta$.

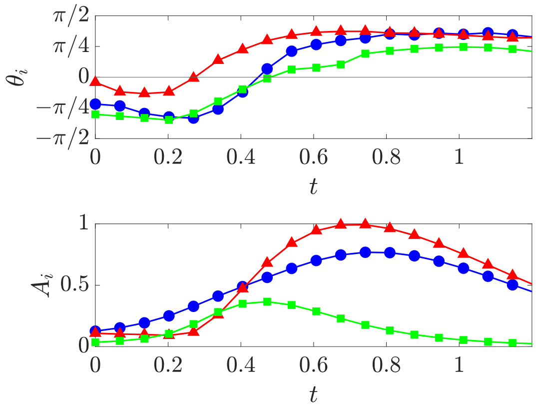

Figure 4.4: Mode angle (top) and magnitude (bottom) of the principal response mode as a function of time. The streamwise component of the mode is represented by −● (blue), the wall-normal component by −■ (green) and the spanwise component by −▲ (red).

transient energy amplification in shear flows (Encinar & Jiménez, 2020; Jiménez, 2013, 2015, 2018; Landahl, 1975). A two-dimensional physical description is given in Jiménez (2013, 2018): the mean shear profile rotates backward-tilting velocity structures forward (in the positive x_1- direction), effectively extending the wall-normal distances between structures; to compensate, continuity imposes larger wall-normal fluxes, *i.e.* larger wall-normal velocity perturbations. This effect amplifies the velocity perturbations until the velocity structures are tilted past the normal to the wall, after which the mechanism is reversed and the perturbations are attenuated. The tilting angle of the velocity perturbations does not affect the streamwise or spanwise velocities directly, and after those components are amplified by the growth of the wall-normal component through lift-up, they decay slowly through viscous effects (Jiménez, 2013). Thus, due to the long-lasting effects on the streamwise component of a brief amplification of the wall-normal velocity perturbation, it is proposed that these Orr bursts are involved in the generation of persistent near-wall streaks (Encinar & Jiménez, 2020; Jiménez, 2013, 2015).

Because of its possible role in regenerating near-wall streaks, the Orr mechanism in linearized wall-bounded flows has been examined in Jiménez (2013, 2015, 2018) and Encinar and Jiménez (2020). These studies rely on computing optimal growth trajectories for the linearized equations with viscosity as well as solutions to the inviscid linearized equations The optimal trajectories are defined as those emanating from the optimal initial condition which maximizes the growth of kinetic energy under the linearized dynamics (Butler & Farrell, 1993; Schmid et al., 2002). The linear trajectories exhibit the characteristic forward tilting of velocity structures in conjunction with the transient amplification of velocity perturbations, suggesting that the Orr-mechanism is a dominant energy amplification mechanism in the linearized system.

Optimal growth trajectories compute the singular modes for the linearized flow map between an initial condition and velocity perturbations at a later time; the question we wish to answer is whether optimal external forcing upon the linearized system, which could originate from nonlinear interactions, also exploits the Orr mechanism. For this, we use the wavelet-based resolvent analysis formulation. We note that traditional resolvent analysis has been used to reveal some evidence of the Orr mechanism in turbulent jets, where it is identified by the tilt of the optimal forcing structures against the jet shear (Pickering et al., 2020; Schmidt et al., 2018; Tissot et al., 2017). In an attempt to capture the Orr mechanism in channel flow at $Re_\tau = 2000$ as in Encinar and Jiménez (2020), we use the mean profile for channel flow at $Re_\tau = 2000$ (Hoyas & Jiménez, 2008). Lengths are non-dimensionalized with the channel half-height δ^*, and velocities with the friction velocity u_τ^*. We use the same grid in the wall-normal direction as Chapter 3.5 with $N_2 = 128$ collocation points. Transient bursts outside the buffer layer are found in Jiménez (2018) to be most energetic for structures that satisfy $\lambda_1 \approx \lambda_3$. For the streamwise and spanwise wavenumbers used in the Fourier transforms of the linearized fluctuations, we choose those used Encinar and Jiménez (2020), $\lambda_1 = \lambda_3 = 0.7$. We use a uniform temporal grid of size $N_t = 256$. As in Chapter 3.5, the base flow as a function of time is constructed by repeating the mean channel flow velocity and shear profiles for each temporal grid point. We define the time domain to be $[0, T)$, where the total time of $T = 2.15$.

The choice of T depends on the critical layer dynamics that we wish to highlight. From traditional resolvent analysis applied to turbulent stationary channel flow, we know that the resolvent Fourier modes tend to peak in magnitude at the critical layer, *i.e.* where $U(x_2) = \omega / k_1$ (McKeon, 2017, 2019; McKeon & Sharma, 2010; Schmid et al., 2002). In this section, we study the effect of a time-localized forcing on a region $x_2^+ \in [0, 500]$ which contains the inner region of the boundary layer (Hoyas & Jiménez, 2006). This maps to a frequency interval $[0, U(x_2^+ = 500)]k_1 = [0, \omega_{\max}] \approx [0, 185]$ according to the mean profile for turbulent channel flow (Figure 4.1). Thus, using a total time $T = 2.15$ and a Shannon wavelet transform with $L = 1$, the Shannon scaling functions $\zeta(t/2^L - k)$ would cover the frequency interval $N_t/(2T)[-\pi, \pi] \approx [-187, 187]$. To restrict our forcing term to this frequency band while localizing it time time, we use the windowed wavelet-based resolvent analysis framework from Chapter 3.2. We set $\boldsymbol{C}$ to the identity matrix, allowing the response modes to cover the entire time and frequency range. We choose $\boldsymbol{B}$ to select the forcing terms corresponding to the relevant the Shannon scaling function. Without loss of generality, we select the shift parameter $m = 0$ so that the forcing term is concentrated at a time interval centered at $t = 0$.

The principal resolvent response mode obtained from the SVD of $\tilde{\boldsymbol{H}}\boldsymbol{B}$ represents the maximally amplified response to a transient forcing term aligned with the selected wavelet, under the dynamics of the linearized Navier-Stokes equations. Though not forcibly restricted to a frequency band via the response windowing matrix $\boldsymbol{C}$, the resulting principal response mode is confined to the frequency band determined by the forcing, as shown in Figure 4.2(a). This result is expected: in resolvent analysis of statistically stationary flows, the time scales are decoupled (equation (3.29)), and the velocity fluctuations can only extract energy from the mean flow, which is solely composed of a steady-state component. The response mode can thus only contain the frequencies injected by the forcing mode. Figure 4.2(b) shows that the spatially integrated energy of the response mode first grows transiently, peaks at $t = 0.72$, and then decays. This is a consequence of the non-normality of the linearized channel flow system (Schmid et al., 2002). The response modes at three different times are shown in Figure 4.3. We note that the modes are concentrated in a region $x_2 < 0.4$, where the Corrsin shear parameter is approximately 10, which justifies the use of a linearized method to analyze the full system (Jiménez, 2013).

The transient behavior of the modes displays characteristics of the Orr mechanism, mainly a synchronization between the amplification of the wall-normal component of the response mode and its forward tilting. To measure the forward tilting of velocity structures in the response mode, we define the tilt angles as in Jiménez (2015), *i.e.*

$$\theta_i(x_2, t) = -\tan^{-1}\left(\frac{\partial_{x_2} \angle \breve{\boldsymbol{\psi}}_i(x_2, t)}{k_1}\right), \tag{4.1}$$

where $\angle(\cdot)$ represents the complex angle. The phase angle of the complex quantity $\breve{\boldsymbol{\psi}}_i(x_2, t)$ determines the shift of the Fourier mode in the homogeneous directions, with $\angle \breve{\boldsymbol{\psi}}_i / k_1$ representing the displacement in the x_1–direction. Differentiating the streamwise displacement with respect to x_2 yields a ratio between the streamwise displacement and wall-normal displacements, *i.e.* the tangent of the angle with the vertical. A value of $\theta_i = 0$ indicates that the mode is upright, while $\theta_i = -\pi/2$ or $\pi/2$ indicates that the mode is tilted backward or forward, respectively, so that it is horizontal. In Jiménez (2015), the angle defined above is averaged over a region of interest. We define the energy-weighted average tilt as

$$\theta_i^{[y_a^+, y_b^+]}(t) = \frac{\int_{y_a}^{y_b} \|\breve{\boldsymbol{\psi}}_i\|^2 \theta_i dx_2}{\int_{y_a}^{y_b} \|\breve{\boldsymbol{\psi}}_i\|^2 dx_2}, \tag{4.2}$$

and the amplitude as

$$A_i^{[y_a^+, y_b^+]} = \left(\int_{y_a}^{y_b} \|\breve{\boldsymbol{\psi}}_i\|^2 dx_2 \right)^{\frac{1}{2}}, \tag{4.3}$$

and pick $y_a^+ = 0$ and $y_b^+ = 2000$ to capture the half-channel. The results (Figure 4.4) show that the amplitude of the wall-normal velocity component of $\breve{\boldsymbol{\psi}}_2$ indeed peaks roughly when $\theta_2^{[0,2000]} \approx 0$ at $t \approx 0.45$, and decays as $\theta_2^{[0,2000]}$ tilts past zero until it vanishes for $\theta_2^{[0,2000]} = \pi/4$.

We note that the spanwise component tilts forward much faster than the streamwise and wall-normal components (Figure 4.4). This faster tilt has been attributed to the spanwise component's placement closer to the wall where the shear is stronger (Encinar & Jiménez, 2020), and we do indeed find that $\breve{\boldsymbol{\psi}}_{\mathbf{3}}$ is closer to the wall compared with $\breve{\boldsymbol{\psi}}_{\mathbf{2}}$. However, we also find that $\breve{\boldsymbol{\psi}}_{\mathbf{1}}$ is located at the same wall-normal height as $\breve{\boldsymbol{\psi}}_{\mathbf{3}}$, and hypothesize that it tilts forward at the same rate as $\breve{\boldsymbol{\psi}}_{\mathbf{2}}$ because of the more direct coupling between the two components via the $u_2 dU_1/dx_2$ term in the linearized momentum equations.

Moreover, both the streamwise and spanwise components of the mode peak at $t \approx 0.75$, *i.e.* after $\theta_1^{[0,2000]}$ and $\theta_3^{[0,2000]}$ cross the zero threshold and approximately $t \approx 0.35$ later than the amplitude peak for the wall-normal component. The streamwise and spanwise components also decay more slowly than the wall-normal component, even as their tilt is relatively constant at $\theta_1^{[0,2000]} = \theta_3^{[0,2000]} = \pi/4$ and after the wall-normal component vanishes. The delayed growth of the streamwise and spanwise perturbations and their slow decay can be explained by considering the linearized advection–diffusion equation for the wall-normal vorticity v_2, where the wall-normal velocity perturbation acts as a forcing term:

$$\left(\partial_t + U_1 \partial_{x_1} - \frac{1}{Re}(\partial_{x_1}^2 + \partial_{x_2}^2 + \partial_{x_3}^2) \right) v_2 = -\frac{\mathrm{d}U_1}{\mathrm{d}x_2} \frac{\partial u_2}{\partial x_3}. \tag{4.4}$$

Even if the u_2–dependent forcing in the right-hand side disappeared, the streamwise and spanwise velocity components would continue their downstream advection via the mean velocity U_1 and would only decay due to viscous dissipation (Jiménez, 2013). This acts at a slower time scale than the mean shear in the near-wall region for the length scales considered. The non-normality of the Squire system (Schmid et al., 2002) explains the delayed growth of the spanwise component after being forced by the wall-normal component. The amplitude streamwise component rises in tandem with the wall-normal component, possibly due their tighter coupling via the presence of the $u_2 dU_1/dx_2$ term in the linearized streamwise momentum equation. The tilt of the streamwise and spanwise components does not directly drive or suppress their amplitudes, since forward-tilting only affects their wall-normal gradients which do not appear in the equations of motion. This allows them to grow even after they attain their maximum positive tilt.

The lifetime of the wall-normal component $\breve{\boldsymbol{\psi}}_2$ of the principal resolvent response mode differs significantly from the bursting time scales in Jiménez (2013, 2015) and Encinar and Jiménez (2020), which argue that the Orr-mechanism is a linear inviscid process whose period scales with the local mean shear. Defining the location of the wall-normal velocity fluctuation as its energy-weighted center of gravity

$$x_{2,g} := \frac{\int_0^1 \|u_2(t_{\max})\|^2 x_2 dx_2}{\int_0^1 \|u_2(t_{\max})\|^2 dx_2}, \tag{4.5}$$

where $t_{\max}$ is the time of maximum amplitude for u_2, we find that $x_{2,g} \approx 0.21$, further away from the wall than the inviscid and optimal growth solutions in Jiménez (2013) and Encinar and Jiménez (2020) located at $x_{2,g} \approx 0.16\lambda_1 \approx 0.11$. Defining a shear time scale S^{-1} as

$$S := \frac{dU_1}{dx_2}(x_2 = x_{2,g}), \tag{4.6}$$

we find that the mode grows and decays in $tS \approx 13$ local shear units, much more slowly than the inviscid and optimal growth solutions, which grow and decay in $tS \approx 1$ and $tS \approx 3.5$ respectively. Moreover, the Orr mechanism studied in Encinar and Jiménez (2020) is linked more broadly to energetic bursting events, which have been considered in Jiménez (2015), and which exhibit a bursting period of $t = 0.2$ for the wall-normal mode corresponding to $(\lambda_x, \lambda_z) = (0.7, 0.7)$, again faster than the growth time scale for $\breve{\boldsymbol{\psi}}_2$. In an attempt to explain the discrepancies between the optimal growth solution in (Encinar & Jiménez, 2020) and the principal resolvent mode, we note that the measures of optimality differ between the optimal growth and wavelet-based resolvent analysis frameworks: while the optimal growth framework measures energy amplification as a ratio between the initial condition and the solution at a given time, wavelet-based resolvent analysis maximizes the integrated kinetic energy of the entire time interval considered. This may better capture energetic structures that persist in time. Resolvent analysis additionally provides the optimal forcing that produces the response in the velocity field, which is helpful in studying mechanisms that drive linear transient growth in turbulent flows.

Encinar and Jiménez (2020) also measure bursting time scales directly using turbulent channel flow data. These better match the growth and decay time scale of our principal resolvent mode, despite the discrepancies with the optimal linear growth solution. Using an average shear time scale defined as

$$S_\Lambda := \frac{(U_1(x_2 = y_b) - U_1(x_2 = y_a))}{y_b - y_a}, \;\; y_a = 0.7, \;\; y_b = 0.25, \tag{4.7}$$

where $\Lambda = [y_a, y_b]$ captures a section of the logarithmic region, we find that $\breve{\boldsymbol{\psi}}_{\mathbf{2}}$ takes $tS_\Lambda \approx 1.87$ average shear units to grow to half its maximum amplitude, compared with $tS_\Lambda \approx 1$ in Encinar and Jiménez (2020). The amplitude and timescale of the process captured by $\breve{\boldsymbol{\psi}}$ can be further compared with other studies of bursting in the near-wall region of turbulent channel flow at moderate Re_τ. In Flores and Jiménez (2010), turbulent energy is found to peak at time intervals of approximately $6x_2$, and given that our resolvent modes are centered at $x_2 \approx 0.2$, the trend would predict a bursting period of $t = 1.2$. This roughly matches the timescale $t \approx 1.5$ for the growth and decay of $\breve{\boldsymbol{\psi}}_{\mathbf{2}}$. Likewise, in Hwang and Bengana (2016), which studies bursting in the logarithmic region of the channel, the relation $t = 2\lambda_3$ is found to describe the bursting period. For our case where $\lambda_3 = 0.7$, this would correspond to a bursting period of $t = 1.4$, again matching the lifetime of $\breve{\boldsymbol{\psi}}_{\mathbf{2}}$.

Thus, by using the windowed wavelet-based resolvent analysis framework described in Chapter 3.2, we obtain a time-localized forcing mode that maximizes the integrated action of its response. The wall-normal component of the response mode exhibits the coupling between tilt angle and magnitude characteristic of the Orr mechanism. The streamwise and spanwise components of the mode, first driven by the wall-normal one, outlive it and decay at a slower time scale determined by viscous dissipation. The Orr mechanism is therefore the most efficient method of generating energetic and persistent perturbations in the linearized setting. The relevance of this transient principal response mode (and the Orr mechanism) to near-wall turbulence is suggested by the close similarity between its lifetime and bursting time scales detected in turbulent channel flow.

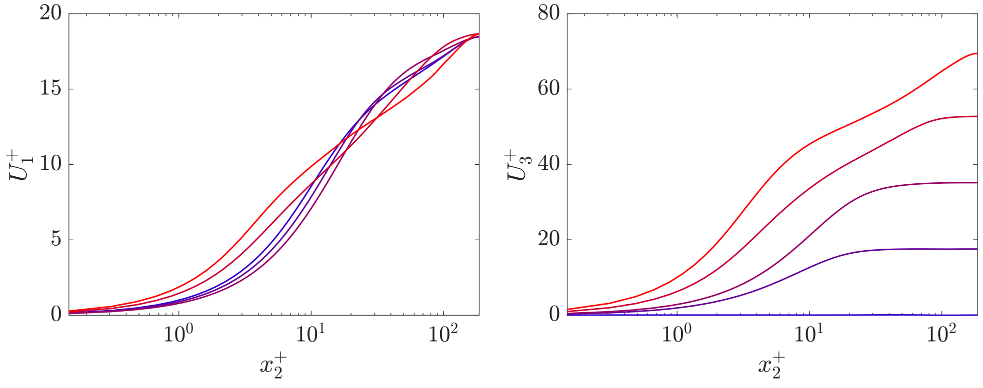

(a) (b)

Figure 4.5: Mean (a) streamwise and (b) spanwise velocity profile from $t = 0$ (blue) to $t = 2.34$ (red). The times shown are $t = 0$, 0.58, 1.17, 1.76, 2.34. Data taken from Lozano-Durán et al. (2020). Time t is non-dimensionalized with $u_{\tau,0}/\delta$

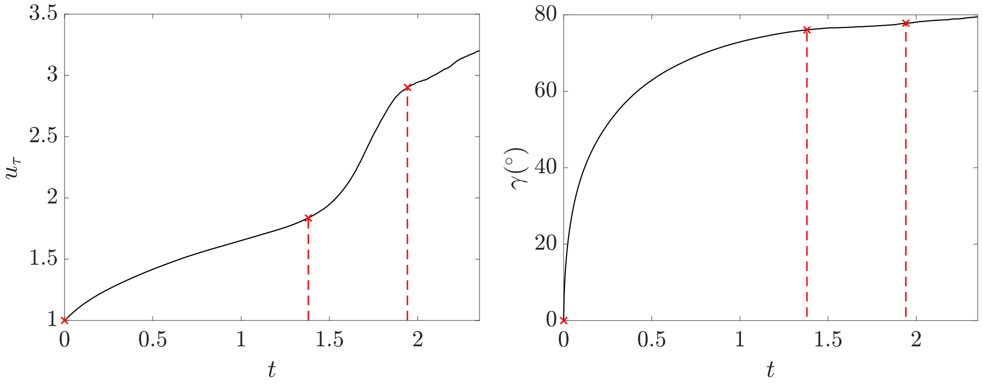

(a) (b)

Figure 4.6: (a) Friction velocity u_τ and (b) wall shear-stress angle $\gamma = \tan^{-1}(\tau_3/\tau_1)$ as a function of time. Data taken from Lozano-Durán et al. (2020). The vertical dashed lines are at $t = 0, 1.38, 1.94$, and correspond to the choice of λ_1^+ and λ_3^+ for the modes plotted in Figure 4.7

4.2 Channel flow under a sudden spanwise pressure gradient

In this section, we use wavelet-based resolvent analysis to tackle a problem with a time-varying mean profile that is not periodic in time. We consider a fully developed turbulent channel flow at $Re_\tau = 186$ that is subjected to a sudden lateral pressure gradient $dP/dx_3 = \Pi dP/dx_1$ at $t = 0$ with $\Pi = 30$ (Lozano-Durán et al., 2020; Moin et al., 1990). Under the influence of the spanwise pressure gradient, the flow, commonly referred to as a three-dimensional (3-D) channel flow, gradually reorients itself to point in the $(dP/dx_1, dP/dx_3)$ direction parallel to the wall. Before reaching its new steady state, the flow passes through an initial transient period during which the tangential Reynolds stress—the correlation between the velocity fluctuation in the instantaneous direction of the flow and the velocity fluctuation normal to the wall—counterintuitively decreases before increasing linearly, with the depletion and growth rate scaling as $\Pi x_2/\delta$ (Lozano-Durán et al., 2020). Wavelet-based resolvent analysis is uniquely equipped to study this non-stationary, non-periodic problem. We use the method to shed light on how the linear amplification properties of the flow change with time and lead to the suppression of velocity perturbations, a phenomenon reflected in the depletion of Reynolds stresses in the turbulent statistics.

The mean velocity $\boldsymbol{U}(x_2, t) = (U_1, 0, U_3)$ and shear $d\boldsymbol{U}/dx_2(x_2, t) = (dU_1/dx_2, 0, dU_3/dx_2)$ profiles represent averages in the spanwise and streamwise directions and are obtained from Lozano-Durán et al. (2020). Both the mean velocity and the mean shear have non-zero streamwise and spanwise components that vary with time. The streamwise and spanwise components of the mean velocity are shown in Figure 4.5. Velocities are non-dimensionalized by the initial friction velocity $u^*_{\tau,0}$. We indeed note that the friction velocity indeed increases as the spanwise component of the flow develops (Figure 4.6(a)). Lengths are non-dimensionalized by the channel half-height δ^*, and time by $\delta^*/u^*_{\tau,0}$. All of the non-dimensionalization scales are summarized in Table 2.1. The Reynolds number for this problem is $Re = Re_{\tau,0} := u^*_{\tau,0}\delta^*/\nu^*$. The time domain of the simulation is $[0, T)$, where $T = 2.34$.

To construct the discrete resolvent operator, we use a Chebyshev grid of size $N_2 = 65$ in the x_2- direction extending from $x_2 = 0$ to $x_2 = 1$. For the spatial derivatives in the x_2- direction, we choose second-order-accurate finite difference matrices. We enforce a no-slip and no-penetration boundary condition at the wall and a free-slip and no-penetration condition at the centerline.

The time derivative matrix $\boldsymbol{D}_t$ is a first-order backward difference operator and is made to enforce a Neumann-type condition, $\partial_t(\cdot)|_{t=0} = \partial_t(\cdot)|_{t=T} = 0$. To reduce the impact of the boundary condition on the modes at $t = 0$ we extend U_1 and U_3 to the time interval $t \in [-0.58, T]$ and assume $U_i(t \leq 0, y) = U_i(t = 0, y)$ and $dP/dx_3(t < 0) = 0$. When the modes are plotted, we only show the original time domain $t \in [0, T]$ and exclude the contribution from negative times. We use a temporal resolution of $N_t = 1000$ for the extended time frame. Despite the use of a finite difference operator in time, we note that the leading modes are not spuriously distorted (see Chapter 3.4) and that filtering-out the high frequency waves as in

Chapter 3.6 has little effect on the results.

For the spatial scales in the homogeneous directions, we choose wavelengths that capture the streamwise and spanwise spacing of near-wall streaks, traditionally $(\lambda^+_{1,0}, \lambda^+_{3,0}) = (1000, 100)$ in channel flow at $Re_\tau = 186$ with no spanwise component, as in Chapter 3.5. Since the non-equilibrium flow gradually develops a strengthening spanwise component, we must take into account the orientation and magnitude of the mean shear profile. To capture the relevant aspect ratio at a time t, we must multiply the traditional length scales of $(\lambda^+_{1,0}, \lambda^+_{3,0}) = (1000, 100)$ by a factor of $Re_\tau(t)/Re_{\tau,0} = u^*_\tau(t)/u^*_{\tau,0} = u_\tau$, plotted in Figure 4.6(a). To account for the new orientation of the streaks, we apply a rotation by the wall-shear stress angle $\gamma(t) = \tan^{-1}(\tau_3/\tau_1)$, where τ_i is the instantaneous wall-shear stress in the x_i direction (Figure 4.6(b)). We can thus tune wavelet-based resolvent analysis to flow conditions at time t by modifying the target wavelengths using the following expressions:

$$\lambda^+_1 = \left(\lambda^+_{1,0}\cos(\gamma(t)) - \lambda^+_{3,0}\sin(\gamma(t))\right) u_\tau(t) \tag{4.8}$$

$$\lambda^+_3 = \left(\lambda^+_{1,0}\sin(\gamma(t)) + \lambda^+_{3,0}\cos(\gamma(t))\right) u_\tau(t). \tag{4.9}$$

Here, $(\cdot)^+$ indicates the wall scaling with $Re_{\tau,0}$, before the lateral pressure gradient is applied. In this section, we focus on three times: $t = 0$, 1.3 and 1.94. For $t = 0$, we perform a wavelet-based resolvent analysis using the traditional $(\lambda^+_1, \lambda^+_3) = (\lambda^+_{1,0}, \lambda^+_{3,0}) := (1000, 100)$, preferred by the near-wall streaks at $Re_\tau = 186$ prior to the lateral pressure gradient. For times $t = 1.3$ and $t = 1.94$, we compute the modes using spatial parameters $(\lambda^+_1, \lambda^+_3) = (264, 1827)$ and $(\lambda^+_1, \lambda^+_3) = (329, 2898)$, respectively.

The principal resolvent modes for the first wavelength pair $(\lambda^+_1, \lambda^+_3) = (1000, 100)$ are shown in Figures 4.7(a, b). The magnitude of the modes in the frequency-time domain is also plotted in Figures 4.8(a, b). The resolvent modes, which exhibit a predominant streamwise component, are centered around $t = 0$ and located in a region $x_2 < 0.25$ or $x^+_2 < 45$, *i.e.* within the buffer layer. The principal modes thus capture the near-wall streaks. Their subsequent decay in time can be explained by the changing flow conditions. As the spanwise wall-shear stress τ_3 grows and causes u_τ to increase and the wall shear stress tensor to rotate in the x_3–direction, the length scales $(\lambda^+_1, \lambda^+_3) = (1000, 100)$ are no longer the linearly most amplified structures. The near-wall streaks would indeed stretch and orient themselves in the direction of the adapting mean profile.

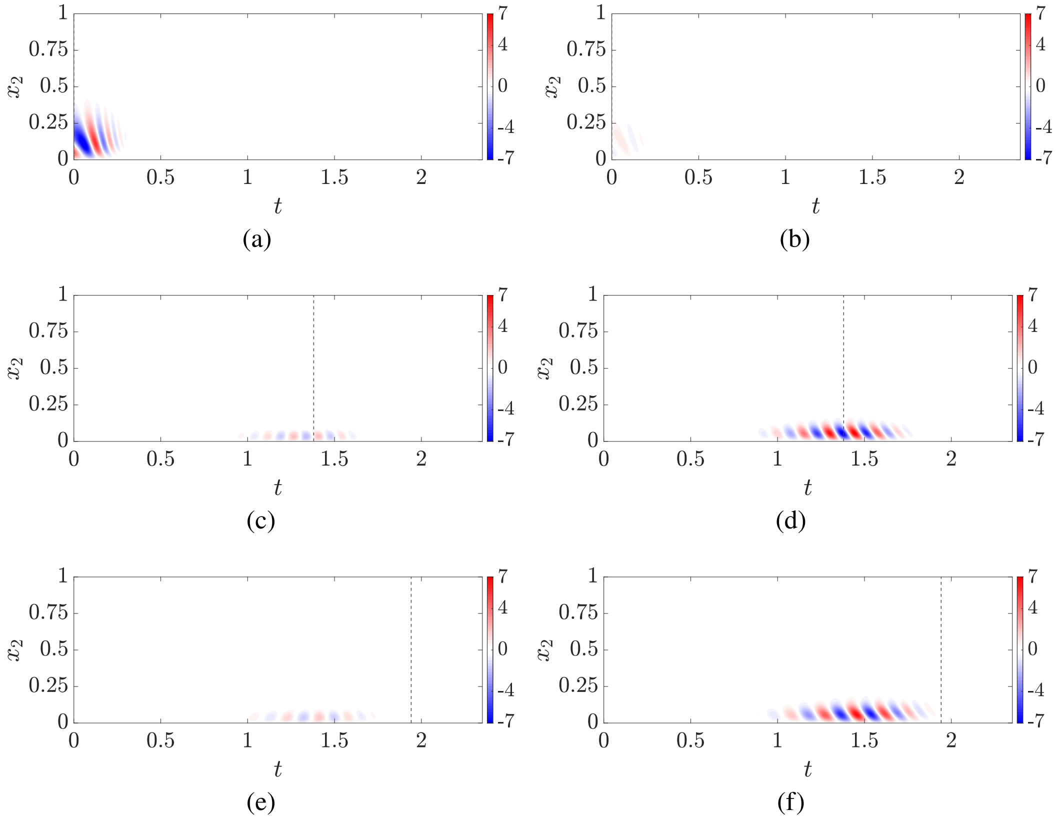
(a) (b) (c) (d) (e) (f)

Figure 4.7: Real part of $\check{\psi}_1$ (left) and $\check{\psi}_3$ (right) for the turbulent channel subject to a spanwise pressure gradient. The chosen spatial scales are (a, b) $\lambda_1^+ = 1000$, $\lambda_3^+ = 100$, (c, d) $\lambda_1^+ = 264$, $\lambda_3^+ = 1827$, and (e, f) $\lambda_1^+ = 329$, $\lambda_3^+ = 2898$. The vertical dashed lines mark (a, b) $t = 0$, (c, d) $t = 1.38$, and (e, f) $t = 1.94$.

The principal resolvent response mode for the second pair of spatial scales, $(\lambda_1^+, \lambda_3^+) = (264, 1827)$ is plotted in Figures 4.7(c, d). The frequency-time map of the modes is shown in Figure 4.8(c, d). The wavelengths of the modes were chosen to match the expected length scales of near-wall streaks at $t = 1.38$, and we indeed observe that the modes are centered around the target $t = 1.38$. Moreover, the spanwise component of the response mode is much more dominant than the streamwise component, which reflects the new wall-shear angle $\gamma = 75.7°$. Wavelet-based resolvent analysis is thus able to reflect non-equilibrium effects and capture near-wall streaks that transiently stretch and rotate under the influence of time-varying mean flow conditions.

For the third case, $(\lambda_1^+, \lambda_3^+) = (329, 2898)$, tuned to conditions at $t = 1.94$, the modes (Figures 4.7(e, f) and Figures 4.8(e, f)) are not centered around the target time. We speculate that this is due to the incompatibility between the Neumann

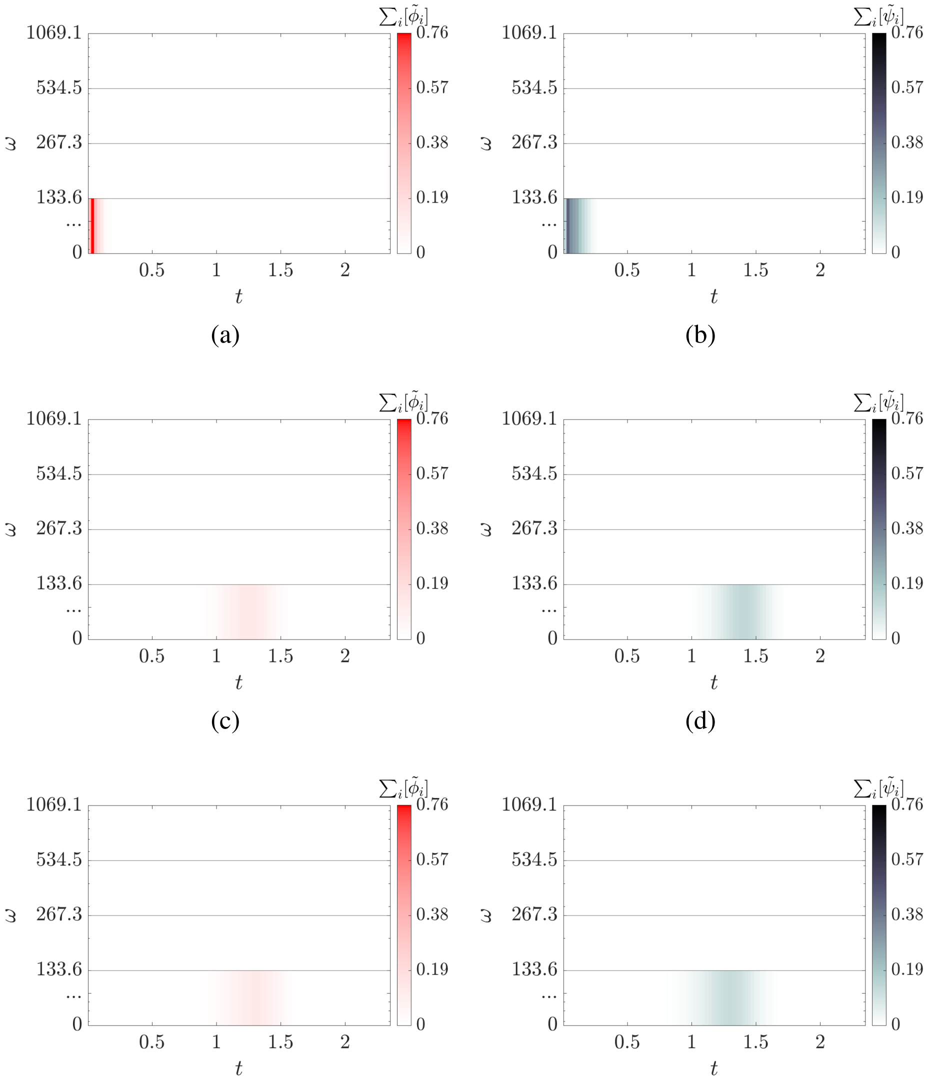

(a) (b)

(c) (d)

(e) (f)

Figure 4.8: Principal forcing (left) response (right) modes in the frequency-time plane for the turbulent channel subject to a spanwise pressure gradient, for (a, b) $\lambda_1^+ = 1000$, $\lambda_3^+ = 100$, (c, d) $\lambda_1^+ = 264$, $\lambda_3^+ = 1827$, and (e, f) $\lambda_1^+ = 329$, $\lambda_3^+ = 2898$.

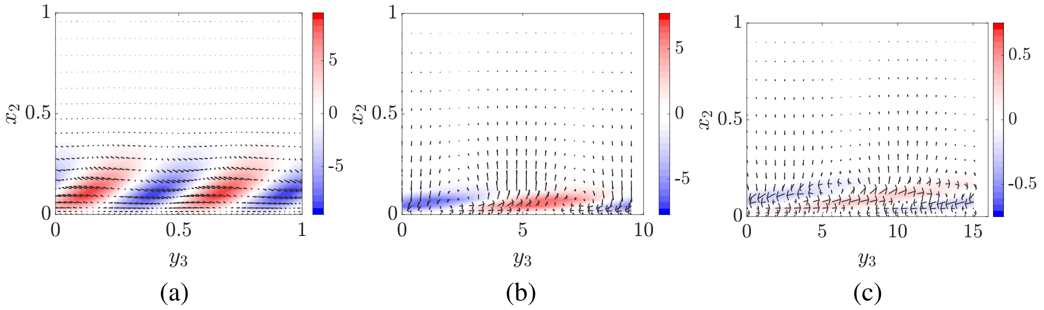

(a) (b) (c)

Figure 4.9: Principal response mode in the reference frame rotated about x_2 by an angle γ, at (a) $t = 0$, (b) $t = 1.38$, and (c) $t = 1.94$. The contours represent the streamwise component; the arrows represent the velocity field in the wall-parallel plane.

boundary condition imposed at $t = 2.34$, and the mean flow conditions which have not reached a statistically steady state by that time. Due to the boundary condition, the modes cannot grow beyond the temporal boundary and are artificially damped near the end of the time domain.

Figure 4.9 shows the principal response mode in the physical domain for the three target length scale pairs, in the reference frame rotated by γ about the x_2–axis. We denote the streamwise and spanwise directions in the rotated reference frame by y_1 and y_3, respectively, with $y_1 = x_1\cos(\gamma) - x_3\sin(\gamma)$, and $y_3 = x_1\sin(\gamma) + x_3\cos(\gamma)$ The modes resemble each other qualitatively, and capture elongated near-wall streaks in the direction of the rotated flow. The length and spanwise spacing of the streaks increases with wall shear stress, as expected. Moreover, the response modes for $(\lambda_1^+, \lambda_3^+) = (264, 1827)$ and $(\lambda_1^+, \lambda_3^+) = (329, 2898)$ (Figure 4.9(b)) are concentrated closer to the wall than for $(\lambda_1^+, \lambda_3^+) = (1000, 100)$ (Figure 4.9(a)), which indicates that the region of high-sensitivity to forcing moves closer to the wall as Re_τ increases. This is in line with the behavior of near-wall turbulence: for higher Re_τ, the buffer and logarithmic layers, which contain the bulk of turbulent energy in channel flow, are closer to the wall. We note, however, that the mode corresponding to $(\lambda_1^+, \lambda_3^+) = (329, 2898)$ is expected to be located at an even lower wall-normal height than the mode corresponding to $(\lambda_1^+, \lambda_3^+) = (264, 1827)$, and attribute its higher location to the effect of the temporal boundary condition at the end of the time domain.

We can compute flow and shear angles from the principal resolvent mode and compare them to the wall shear stress angle γ extracted from DNS. We define the mode shear angle as

$$\breve{\gamma}(x_2, t) = \left| \tan^{-1} \left(\frac{\mathrm{d}\psi_3/\mathrm{d}x_2}{\mathrm{d}\psi_1/dx_2} \right) \right|_{x_1 = x_{1,\max}, x_3 = x_{3,\max}}, \tag{4.10}$$

where ψ_i denotes the inverse Fourier and wavelet transform of the i^{th} mode component, and $(x_{1,\max}, x_{3,\max})$ denotes the location in the x_1–x_3 plane where the amplitude of the response mode $\boldsymbol{\psi}$ is maximal at each x_2. We plot the results for the three spatial parameters at their respective target times (Figure 4.10). For the mode corresponding to $(\lambda_1^+, \lambda_3^+) = (1000, 100)$, the mode shear angle $\breve{\gamma}$ matches the wall shear angle of zero from DNS at a wall-normal location slightly farther from the wall than the location of peak amplitude. For $(\lambda_1^+, \lambda_3^+) = (264, 1827)$ and $(\lambda_1^+, \lambda_3^+) = (329, 2898)$, we observe that $\breve{\gamma}$ matches γ well at the amplitude peaks. For all three sets of spatial parameters, the mode angles at the wall itself differ significantly from the wall shear angle from DNS, though this is expected since the modes obtained are lifted from the wall and decay to match the wall boundary condition.

The amplification of the response mode given by the leading singular value of the resolvent operator differs across the chosen spatial parameters. The energy of the principal response mode corresponding to $(\lambda_1^+, \lambda_3^+) = (1000, 100)$, which peaks for $t < 0$, is amplified by a factor of $\sigma_1^2 \approx 8$, while the energy of the modes corresponding to $(\lambda_1^+, \lambda_3^+) = (264, 1827)$ and $(\lambda_1^+, \lambda_3^+) = (329, 2898)$, respectively peaking at $t = 1.34$ and $t = 1.94$, are respectively amplified by a factor of $\sigma_1^2 \approx 0.4$ and $\sigma_1^2 \approx 0.6$. This indicates an effective energy suppression. In the fully turbulent system simulated in Lozano-Durán et al. (2021), a decrease in Reynolds stresses is similarly observed during the development of the spanwise mean flow, even when the $x_1 - x_3$ plane is rotated about the x_2–axis to account for the new direction of the wall shear stress. The authors propose that the developing spanwise mean flow generates smaller transverse structures close to the wall which disrupt the coherence of the dominant streamwise rolls and inhibit them from vertically transporting momentum upward from the near-wall region.

The behavior of the wavelet-based resolvent modes allows us to expand this proposed explanation. The optimal forcing for the mean flow conditions at a time t is in the form of rolls approximately pointing in the direction $\gamma(t)$, and its corresponding response mode eventually aligns itself with the forcing angle after a period of transient growth, as shown in Figures 4.11 (a) and (b). Due to the non-normality of the linearized system, the optimal forcing peaks before the target time t, and thus the optimal forcing may be instantaneously misaligned with the rotating mean

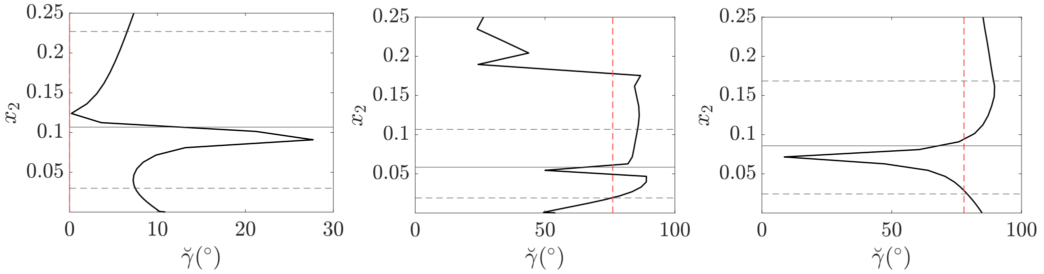

(a) (b) (c)

Figure 4.10: Shear angle of the principal response mode for (a) $(\lambda_1^+, \lambda_3^+) = (1000, 100)$ at $t = 0$, (b) $(\lambda_1^+, \lambda_3^+) = (264, 1827)$ at $t = 1.38$, and (c) $(\lambda_1^+, \lambda_3^+) = (329, 2898)$ at $t = 1.94$. The red vertical line (- -) indicates the wall shear-stress angle at the chosen times; the horizontal black line indicates the location of the peak of kinetic energy $|\breve{\psi}_1|^2 + |\breve{\psi}_2|^2 + |\breve{\psi}_3|^2$ at the target times, and the dashed horizontal lines indicate where the mode energy is at 10% of the peak.

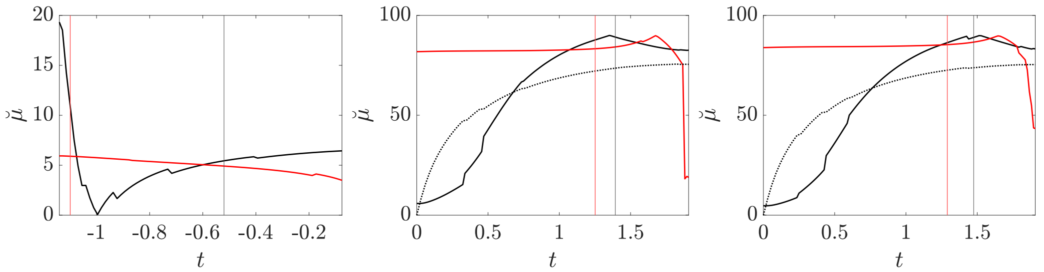

(a) (b) (c)

Figure 4.11: Flow angle of the principal forcing (red) and response (black) modes for (a) $(\lambda_1^+, \lambda_3^+) = (1000, 100)$, (b) $(\lambda_1^+, \lambda_3^+) = (264, 1827)$, and (c) $(\lambda_1^+, \lambda_3^+) = (329, 2898)$. The vertical lines indicates the amplitude peaks for the forcing (red) and response (black) modes, and the dotted black line represents $\gamma(t)$.

flow during the transient growth period of the response. Indeed, the forcing mode is not computed to maximize the instantaneous kinetic energy amplification, but maximizes instead the time-integrated kinetic energy of the response over the entire temporal domain.

More insight can be gained by considering the linearized equation governing the wall-normal vorticity v_2

$$\left(\partial_t + U_1\partial_{x_1} + U_3\partial_{x_3} - \frac{1}{Re}(\partial^2_{x_1} + \partial^2_{x_2} + \partial^2_{x_3})\right) v_2 = \left(-\frac{\mathrm{d}U_1}{\mathrm{d}x_2}\partial_{x_3} + \frac{\mathrm{d}U_3}{\mathrm{d}x_2}\partial_{x_1}\right) u_2 + g_2, \tag{4.11}$$

where $g_2 := \partial_{x_3} f_1 - \partial_{x_1} f_3$ denotes the external forcing. We note that in this problem, the mean wall-normal flow U_2, and the wall-normal gradients $\mathrm{d}U_1/\mathrm{d}x_2$

and $\mathrm{d}U_3/\mathrm{d}x_2$ are zero. Introducing a flow angle $\mu := \tan^{-1}(U_3/U_1)$ and a shear angle $\upsilon := \tan^{-1}((\mathrm{d}U_3/\mathrm{d}x_2)/(\mathrm{d}U_1/\mathrm{d}x_2))$, we can rewrite equation (4.11) in the reference frame locally rotated by μ as

$$\left(\partial_t + (U_1^2 + U_3^2)^{\frac{1}{2}}\partial_{x_1'} - \frac{1}{Re}(\partial^2_{x_1'} + \partial^2_{x_2} + \partial^2_{x_3'})\right) v_2 = \\ \left(\frac{\mathrm{d}U_1}{\mathrm{d}x_2}^2 + \frac{\mathrm{d}U_3}{\mathrm{d}x_2}^2\right)^{\frac{1}{2}} \left(-\cos(\mu - \upsilon)\partial_{x_3'} + \sin(\mu - \upsilon)\partial_{x_1'}\right) u_2 + g_2, \quad (4.12)$$

where (x_1', x_2, x_3') denote the coordinates rotated anticlockwise by angle μ in the $x_1 - x_3$ plane. The left-hand side of equation (4.12) is identical to the classical Squire equation for perturbations about a one-dimensional streamwise mean flow, with an effective advection velocity of $(U_1^2 + U_3^2)^{1/2}$. The right-hand side includes a lift-up term modified by the misalignment between the mean shear and velocity profiles. If the mean flow is at equilibrium and $\mu = \upsilon$, we obtain an identical lift-up term to the classical Squire equation, with an effective mean shear of $\left((\mathrm{d}U_1/dx_2)^2 + (\mathrm{d}U_3/\mathrm{d}x_2)^2\right)^{1/2}$. The lift-up term in the Squire equation constitutes a way for the wall-normal velocity perturbations to force the streamwise and spanwise components, as discussed in Chapter 4.1, Jiménez (2013, 2018). Through this coupling, the streamwise and spanwise velocity components can be efficiently forced by f_2 along with f_1 and f_3. However, in a non-equilibrium rotating flow, the mean shear profile lags behind the mean velocity, *i.e.* $\mu \neq \upsilon$, causing a misalignment between the two profiles which is particularly pronounced for regions farther away from the wall. The term pertaining to the misalignment in equation (4.12) damps the effect of the wall-normal velocity perturbation u_2 on the wall-normal vorticity, and consequently, the streamwise and spanwise velocity perturbations. This is illustrated by Figure 4.12: for the initial one-dimensional mean flow configuration in Figure 4.12(a), the optimal forcing mode exploits the lift-up mechanism via a strong wall-normal component; for the rotated configurations in Figures 4.12(b) and (c), the wall-normal component of the optimal forcing is significantly attenuated.

Thus, the lag of the mean shear profile disrupts the coupling between the wall-normal, and the streamwise and spanwise velocity perturbations. In a non-equilibrium rotating mean flow, wall-normal velocity perturbations are less efficient at producing slow-decaying streaks in the flow direction (than in the case discussed in Chapter 4.1, for example), and the mean flow selects rolls with a much weaker wall-normal component. Evidence of this effect is shown in Figure 4.13. The DNS-averaged tangential Reynolds stress and the misalignment between the mean velocity and shear

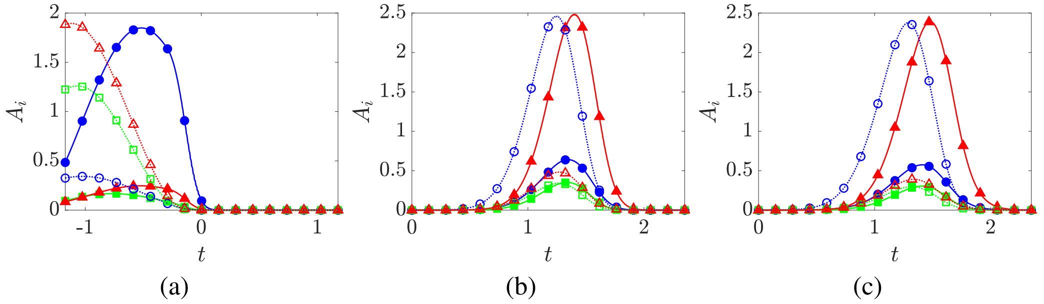

(a) (b) (c)

Figure 4.12: Amplitudes for the streamwise (blue ●), spanwise (red ▲), and wall-normal (green ■) components of the principal forcing (dotted line, hollow markers) and response (solid line, filled markers) modes, for (a) $(\lambda_1^+, \lambda_3^+) = (1000, 100)$, (b) $(\lambda_1^+, \lambda_3^+) = (264, 1827)$, and (c) $(\lambda_1^+, \lambda_3^+) = (329, 2898)$.

profiles are indeed anti-correlated. Interestingly, the misalignment at $x_2^+ = 40$ peaks roughly $t^+ \approx 100$ before the minimum in the tangential Reynolds stress. Though not shown, this time lag is more-or-less consistent for all wall-normal heights $x_2^+ > 11$ ($x_2 > 0.06$), though the peaks of $\mu - \nu$ and troughs of $-\overline{u_1 u_2}^+$ themselves occur earlier at locations closer to the wall. This may due to non-normal effects; responses to perturbations tend to occur later after a period of transient growth. This is true for the principal resolvent forcing and response modes: the response mode computed using $(\lambda_1^+, \lambda_3^+) = (1000, 100)$ and peaking in amplitude at $t = 0$ also lags about $t^+ \approx 100$ behind its corresponding forcing; the response mode computed using $(\lambda_1^+, \lambda_3^+) = (329, 2898)$ and peaking in amplitude at $t = 1.38$ is faster and peaks $t^+ \approx 30$ after its corresponding forcing.

To close this chapter, we emphasize the potential of wavelet-based resolvent analysis to deepen our understanding of non-equilibrium effects on turbulence. The wavelet-based modes reflect the instantaneous morphological changes that near-wall streaks undergo during the development of the mean flow profile. They additionally reveal changes to the linear amplification mechanisms that produce the streaks. When computed for transient 3-D channel flow, the modes indicate a collapse of the lift-up mechanism, which we attribute to the misalignment between the mean velocity and shear profiles and which greatly reduces the maximum linear amplification attainable in the buffer layer. This new description expands on the explanations in Lozano-Durán et al. (2020) for the counterintuitive and transient depletion of tangential Reynolds stresses in simulations of the turbulent flow.

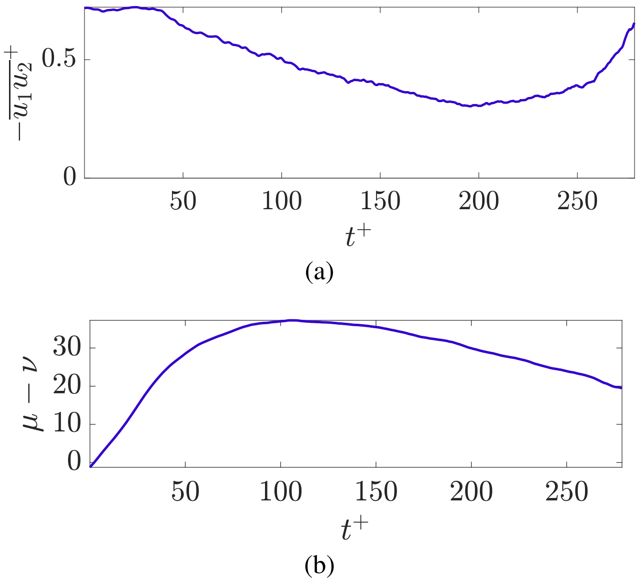

Figure 4.13: (a) Average tangential Reynolds stress at $x_2^+ \approx 40$; (b) Difference between the average flow and shear angles at $x_2^+ \approx 40$. Results are from the DNS conducted in Lozano-Durán et al. (2020).

Chapter 5

APPLICATION II – FLOW ACTUATION

The previous chapters showcase how wavelet-based resolvent analysis can be used to study linear amplification phenomena in turbulent flows. Resolvent analysis is also commonly used to aid in the design of controllers by either identifying regions to which the flow is particularly sensitive to actuation via resolvent forcing modes (Kojima et al., 2020), or providing a cheap model over which to optimize forcing parameters (Liu et al., 2021; Luhar et al., 2014; Toedtli et al., 2019; Yeh et al., 2020). All these methods are built on the assumption that resolvent modes are indeed representative of the turbulent systems for which they are computed. In this chapter, we test the efficacy of linearly optimal resolvent modes at forcing a turbulent system.

The experiments presented in this chapter and published in Ballouz, Dawson, and Bae (2024) and Ballouz et al. (2025) are inspired by Bae et al. (2021), which examines the role that structures aligned with the Fourier-based resolvent forcing modes played in sustaining buffer layer turbulence in the minimal channel. The authors show that removing these contributions at every time step greatly suppresses the turbulent kinetic energy. However, with the physical control of turbulent flows as the ultimate goal, we cannot rely on such high-frequency actuation, and it would thus be valuable to determine a time horizon over which the resolvent forcing is effective. In Chapter 5.1, we used a windowed version of the wavelet-based resolvent operator —first presented in Chapter 3.2— to compute a time-localized, resolvent forcing mode with a compact support in time, which we inject into the minimal flow unit (Chapter 5.2).

The corresponding principal resolvent response mode grows and decays as is expected for non-normal systems. This will allow us to measure the instantaneous discrepancy between the actuated turbulent and linearized flows. By comparing the response of the turbulent system to the principal response mode, we identify the time scales during which the turbulent system responds similarly to the optimal linear response mode (Chapter 5.3) and probe the mechanisms that erode the effects of the injected mode, especially the nonlinear interactions that transfer energy from the actuated scale to secondary ones (Chapter 5.4). We note that computing a time-localized forcing modes and a transient response mode—made possible by the wavelet-based formulation of resolvent analysis—are essential to these objectives.

5.1 Base flow and parameters for resolvent analysis

In this chapter, length scales are normalized by δ^*, the channel half-height, and velocities are normalized by friction velocity u_τ^*. The Reynolds number is friction Reynolds number $Re_\tau = \delta^* u_\tau^* / \nu^* \approx 186$, where ν^* is the kinematic viscosity. x_1, x_2, and x_3 denote the streamwise, wall-normal and spanwise directions, respectively. We study turbulent flow in the minimal flow unit of streamwise length $L_1 = 1.72$, wall-normal height $L_2 = 2$ and spanwise width $L_3 = 0.86$. We take the flow to be periodic in the streamwise and spanwise directions; the no-slip and no-penetration conditions hold at the walls of the channel. We denote the velocity fluctuation field by $\boldsymbol{u} = (u_1, u_2, u_3)$, where u_1, u_2, and u_3 are the streamwise, wall-normal, and spanwise components, respectively.

To compute the base flow—or mean velocity profile—we discretize the streamwise and spanwise directions uniformly using $N_1 = N_3 = 32$ grid points, which results in streamwise and spanwise grid spacings of $\Delta x_1^+ \approx 10$ and $\Delta x_3^+ \approx 5$. In the wall-normal direction, the grid is of size $N_2 = 128$ and stretched according to a hyperbolic tangent distribution, which results in a wall-normal spacing of $\min(\Delta x_2^+) \approx 0.17$ near the wall and $\max(\Delta x_2^+) \approx 7.6$ at the centerline. As in previous chapters, the superscript $(\cdot)^+$ denotes wall units: time and length scales are scaled as $(\cdot)^+ = (\cdot)Re_\tau$. To solve the incompressible Navier-Stokes equations numerically, we use a staggered, second-order accurate, central finite difference method in space (Orlandi, 2000), and a fractional step method is used to compute pressure (J. Kim & Moin, 1985). Integration in time is performed with an explicit third-order-accurate Runge-Kutta method (Wray, 1990). The DNS code has been validated in previous studies of turbulent channel flows (Bae et al., 2018, 2019; Lozano-Durán & Bae, 2016). We compute the mean velocity profile $\boldsymbol{U}(x_2) = (U_1(x_2), 0, 0)$ by averaging DNS results of the unforced system in the streamwise and spanwise directions and time.

Since we aim to inject the modes into a DNS, we use the same staggered x_2–grid as the DNS to compute the resolvent modes to ensure that these modes—which satisfy the linearized incompressible Navier-Stokes equations—are also divergence-free during the simulations. For the same reason, we use the modified wavenumbers $\check{k}_1$ and $\check{k}_3$ that match the discretization scheme of the DNS when defining the spatial derivative operators $\widetilde{\boldsymbol{D}_1}$, $\widetilde{\boldsymbol{D}_3}$, and $\tilde{\boldsymbol{L}}$. These are defined as $\check{k}_1 := 2\sin(k_1 \Delta x_1/2)/\Delta x_1$

and $\breve{k}_3 := 2\sin(k_3\Delta x_3/2)/\Delta x_3$. The minimal flow unit is only large enough to contain one low- and high-speed streak pair, which appears to stretch the entire streamwise length of the unit and repeats only once in the spanwise direction. This configuration corresponds to the Fourier mode defined by the streamwise and spanwise wavenumbers of $k_1 = 0$ and $k_3L_3/(2\pi) = 1$, respectively. These length scales also correspond to a peak in the spectral energy content for the minimal flow unit (Bae et al., 2021).

We choose a periodic time domain $[0, T]$, and choose $T = 22$, which is long enough to allow the resolvent modes to decay to zero. The discretization in time is uniform, with a grid size of $N_t = 128$ corresponding to a spacing of $\Delta t \approx 0.17$. The time derivative operator $\boldsymbol{D}_t$ is a second-order-accurate central finite difference matrix in time. In this chapter, $\boldsymbol{W}$ is a single-stage Daubechies-8 wavelet transform, which is orthonormal and banded. The Daubechies-8 wavelet and scaling functions are compactly supported in time, and restricting the forcing modes to a Daubechies wavelet ensures that they appear as pulses with a finite extent in time. Traditional resolvent analysis in which the Navier-Stokes equations are Fourier-transformed in time reveals that a temporal frequency of $\omega = 0$ produces the modes with the largest kinetic energy amplification (Bae et al., 2021). To target this frequency, we constrain the forcing term to the scaling function of arbitrary shift m (Figure 5.1(a)) by using a windowing matrix $\boldsymbol{B}$ to select the corresponding elements of $\widetilde{\boldsymbol{f}}$. The Fourier spectrum of the scaling function shown in Figure 5.1(b), indeed encompasses the target frequency. Since the scaling function is compactly-supported in time, wavelet-based resolvent analysis will not be able to target $\omega = 0$ uniquely but will capture a wide range of frequencies (see the discussion on the uncertainty principle in Chapter 3). We note that the simulation detailed in above resolves temporal wavenumbers up to $\omega \approx 55{,}000$. The scaling function satisfies $\left(\int_{-\infty}^{+\infty} |\zeta(t)|^2 \mathrm{d}t\right) = 1$.

We weight the resolvent operator so that the principal modes of the SVD maximize the integrated action of the response mode. We define this seminorm for an arbitrary vector $\tilde{\boldsymbol{b}} = [\tilde{b}_1, \tilde{b}_2, \tilde{b}_3, \tilde{b}_p]^T$ as

$$||\tilde{\boldsymbol{b}}||^2 = \frac{1}{L_1(2\delta)L_3} \int_0^{L_1} \int_0^{2} \int_0^{L_3} \int_0^{T} (|b_1|^2 + |b_2|^2 + |b_3|^2)\, \mathrm{d}t\, \mathrm{d}x_3\, \mathrm{d}x_2\, \mathrm{d}x_1, \quad (5.1)$$

where $\boldsymbol{b} = [b_1, b_2, b_3, b_p]^T$ is the inverse transform of $\tilde{\boldsymbol{b}}$. For all j, $\boldsymbol{\phi}_j$, the inverse transform of $\tilde{\boldsymbol{\phi}}_j$, is shaped in time according to the wavelet or scaling function chosen by $\boldsymbol{B}$. As in Chapter 2.1, the resolvent modes occur in equivalent pairs of equal singular values due to the symmetry of the channel geometry. We can linearly

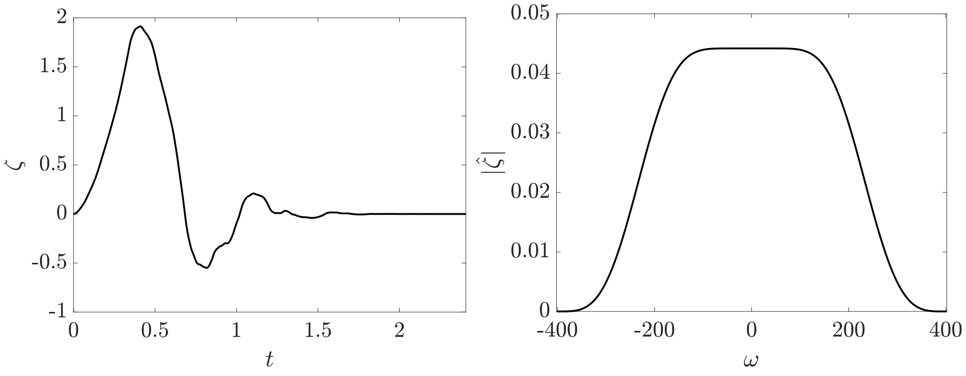

(a) (b)

Figure 5.1: Daubechies-8 scaling function ζ in time (a) and frequency (b) domain.

combine the two singular vectors that correspond to the same singular value to form a new one in the singular plane acting primarily on the bottom half of the channel. Thus, upon injecting this mode into the DNS of the forced Navier-Stokes equations, only the bottom of half of the channel is subject to the forcing, allowing us to use the top half as a control system (Bae et al., 2021). For the remainder of this chapter, $\tilde{\boldsymbol{\phi}}_\mathbf{1}$ refers to the linear combination of the first two equivalent forcing modes that concentrates the forcing in the bottom-half of the channel, re-normalized to satisfy $||\tilde{\boldsymbol{\phi}}_\mathbf{1}|| = 1$, and $\tilde{\boldsymbol{\psi}}_\mathbf{1}$ denotes the corresponding response mode. The modes $\tilde{\boldsymbol{\phi}}_\mathbf{3}$ and $\tilde{\boldsymbol{\psi}}_\mathbf{3}$ are defined similarly with regards to the third and fourth resolvent forcing and response modes. We use $\breve{\boldsymbol{\psi}}_{\boldsymbol{i}}$ and $\breve{\boldsymbol{\phi}}_{\boldsymbol{i}}$ to denote the inverse wavelet-transform in time of $\tilde{\boldsymbol{\psi}}_{\boldsymbol{i}}$ and $\tilde{\boldsymbol{\phi}}_{\boldsymbol{i}}$, respectively.

The obtained resolvent modes are shown in Figure 5.2. Notably, the response modes exhibit transient energy growth and decay as seen in Figures 5.2(a, b). The inverse transforms of the modes are shown in Figures 5.2(c, d). The modes share many similarities with the Fourier-based modes computed for $\omega = 0$ in Bae et al. (2021): the optimal transient nonlinear forcing mode appears in the shape of streamwise rolls, and the optimal velocity fluctuation response appears as predominantly streamwise streaks with alternating signs of the same magnitude. This supports the extensively examined claim that streamwise streaks can be linearly generated by a linear lift-up mechanism, whereby slower moving fluid close to the wall is swept upwards into the faster moving mean flow farther away from the wall. The streak-shaped response mode grows in intensity before fading, showcasing the transient growth that is characteristic of non-normal systems.

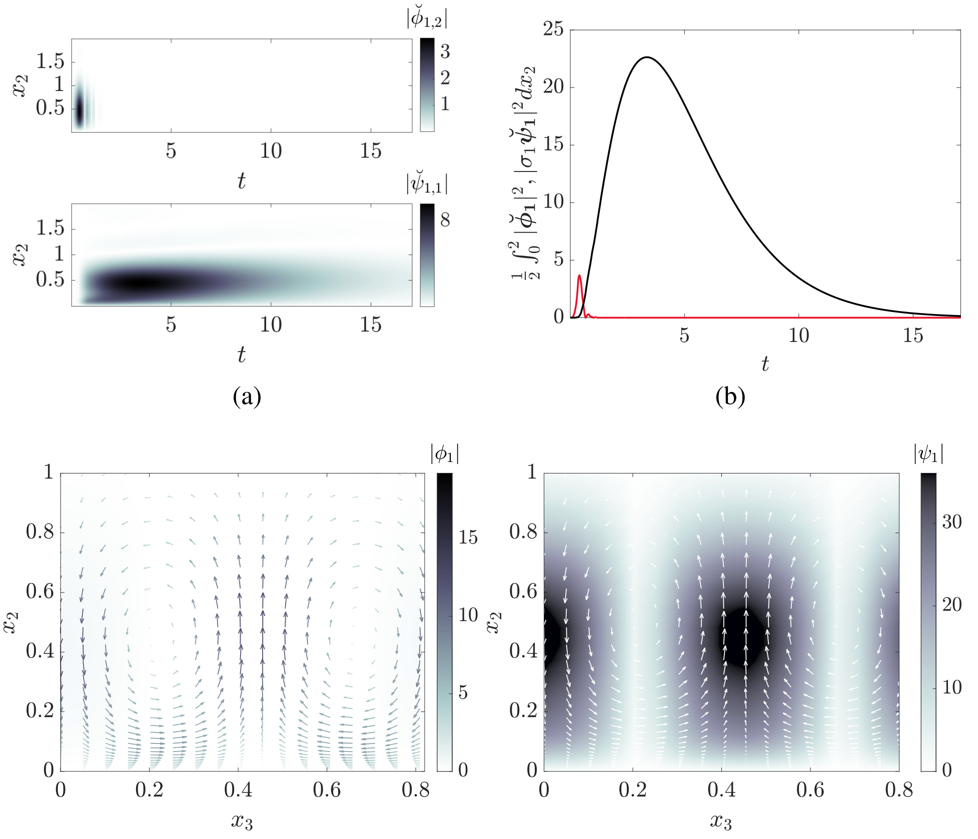

(a) (b)

(c) (d)

Figure 5.2: (a) Magnitudes of the wall-normal component of the principal forcing mode (top) and the streamwise component of the principal response mode (bottom). (b) Integrated energy of the principal forcing (red) and response (black) modes. (c) Principal forcing mode shown at peak amplitude ($t \approx 0.40$). (d) Principal response modes at peak amplitude ($t \approx 2.41$). In (c, d), the contours represent the streamwise magnitude; the arrows, which show the direction of the cross flow components, are colored according to their magnitudes $\sqrt{|\phi_{1,2}|^2 + |\phi_{1,3}|^2}$ in (c), or $\sqrt{|\psi_{1,2}|^2 + |\psi_{1,3}|^2}$ in (d).

5.2 Forced DNS

In this section, we present the details of our numerical experiments, *i.e.* the introduction of the forcing mode obtained in the previous section into an already turbulent state of the minimal flow unit. The turbulent initial condition contains energy at varying scales, and the injection of the mode triggers cross-scale interactions that interfere with the linearly driven transient growth of the response mode.

To initialize the ensemble of the forced simulations, we first perform a DNS of the non-actuated minimal flow unit, fixing the mean profile to be $\boldsymbol{U} = (U_1(x_2), 0, 0)$, used in Chapter 5.1 to calculate the resolvent modes. Snapshots from this simulation serve as the initial conditions to the forced simulations. Freezing the mean profile ensures that the DNS mean profile matches the one used to compute the resolvent modes for all time. We do this by initializing the flow to have the desired mean streamwise profile of U_1, then by removing the steady-state contribution of the right-hand side of the Navier-Stokes equations. The initial snapshots from the fixed-mean simulation are separated by $3.8 \leq \Delta t \leq 19.2$, and amount to ensemble sizes ranging from 1000 to 4000, in order to ensure statistically convergence. For each initial condition, we also obtain a corresponding unforced fixed-mean time series. We denote the velocity fluctuations for the unforced simulations by $\boldsymbol{u}_0(x_1, x_2, x_3, t)$.

Before injecting the forcing mode into the DNS of the minimal flow unit, the mode is normalized so that $||\tilde{\boldsymbol{\phi}}_{\mathbf{1}}||^2 = 1$ and scaled by a complex constant κ with magnitude

$$|\kappa| := \gamma \left(\frac{1}{L_1 (2\delta) L_3} \int_{-\infty}^{+\infty} \int_0^{L_1} \int_0^{2} \int_0^{L_3} \left| \frac{\partial \boldsymbol{u}_{\mathbf{0}}}{\partial t} \right|_{t=0}^2 \zeta(t)^2 \mathrm{d}x_3 \, \mathrm{d}x_2 \, \mathrm{d}x_1 \, \mathrm{d}t \right)^{1/2}, \quad (5.2)$$

where $\gamma \in \{1\%, 2\%, 5\%, 10\%\}$ such that the resolvent forcing mode is increasing the initial energy of the right-hand side by γ. Thus, $|\kappa|^2$ determines the integrated energy injected into the system by the forcing. We choose

$$\angle \kappa = \angle \int_0^2 \int_0^{+\infty} \partial_t \hat{\boldsymbol{u}}_0^{(0,1)} \breve{\boldsymbol{\phi}}_{\mathbf{1}}^* dt dx_2, \quad (5.3)$$

so that the forcing mode is in phase with the right-hand side of the unforced flow field. In the limiting case where the nonlinear interactions are negligible, this provision ensures that the added forcing maximally increases the energy of the target $(0, 1)$–mode.

The forced DNS is the solution to the full incompressible Navier-Stokes equations with the additional right-hand side forcing terms shown below:

$$\frac{\partial u_i}{\partial t} + U_j \frac{\partial u_i}{\partial x_j} + u_j \frac{\partial U_i}{\partial x_j} = -\frac{\partial p}{\partial x_i} + \frac{1}{Re}\frac{\partial^2 u_i}{\partial x_j \partial x_j} + 2\mathfrak{Re}\left(\kappa \breve{\phi}_{1,i}(x_2,t) e^{\mathrm{i}\frac{2\pi x_3}{L_3}}\right) + \mathcal{F}_i, \tag{5.4}$$

$$\frac{\partial u_i}{\partial x_i} = 0. \tag{5.5}$$

The term $\mathcal{F} = (\mathcal{F}_1, 0, 0)$ enforces the condition that the mean streamwise profile of the forced simulation stay fixed and equal to U_1 as in the unforced simulation (Chapter 5.1). We remind the reader that $\boldsymbol{u}(x_1,x_2,x_3,0) = \boldsymbol{u}_0(x_1,x_2,x_3,0)$ for each ensemble member, where $\boldsymbol{u}_0$ is obtained from the unforced DNS. We run the forced DNS for a total time of $T = 5.69$. To test the optimality of $\boldsymbol{\phi_1}$ at forcing the turbulent channel, we repeat the case for $\gamma = 5\%$ using $\boldsymbol{\phi_3}$ and a forcing term with a randomly generated spatial component $\boldsymbol{\phi_{\mathrm{rand}}} = \hat{\boldsymbol{\phi}}_{\mathbf{rand}}(x_2)\zeta(t)$, which we normalize and scale the same way.

5.3 Response of the turbulent minimal flow unit

To characterize how the turbulent system reacts to actuation of varying strength, we track the ensemble-averaged transient response of the simulated minimal flow unit and measure the energy growth of the targeted mode. The optimal resolvent response mode serves as a benchmark for the achievable energy amplification caused by the injected mode. The notation $\widehat{(\cdot)}^{(n_1,n_3)}$ denotes the Fourier transform in the streamwise and spanwise directions corresponding to the streamwise and spanwise wave numbers $k_1 = 2\pi n_1/L_1$ and $k_3 = 2\pi n_3/L_3$, respectively. We define the deviation operator Δ as the difference between the forced and unforced simulations, *e.g.* $\Delta\hat{u}_1^{(0,1)} = \hat{u}_1^{(0,1)} - \hat{u}_{0,1}^{(0,1)}$. We denote the ensemble average by $\overline{(\cdot)}$.

Transient energy growth and decay of streaks in the forced DNS

We define the instantaneous streak energy as

$$\hat{E}_1^{(0,1)}(t) = \left[\frac{|\hat{u}_1^{(0,1)}|^2}{2}\right], \tag{5.6}$$

where $[\cdot] := \int_0^2 (\cdot) dx_2/(2)$ denotes the wall-normal average. Figure 5.3(a) shows the streak energy contained in the $(0,1)$-mode as a function of time, for different resolvent-forcing amplitudes. For all cases, the energies grow and peak before decaying and reverting back to non-forced levels. We observe that the peak energy deviation $\Delta\hat{E}_1^{(0,1)}$ scales sub-quadratically with the forcing amplitudes and is proportional to $|\gamma|^{1.44}$ (Figure 5.3b). For a linear system, the energy peaks would scale

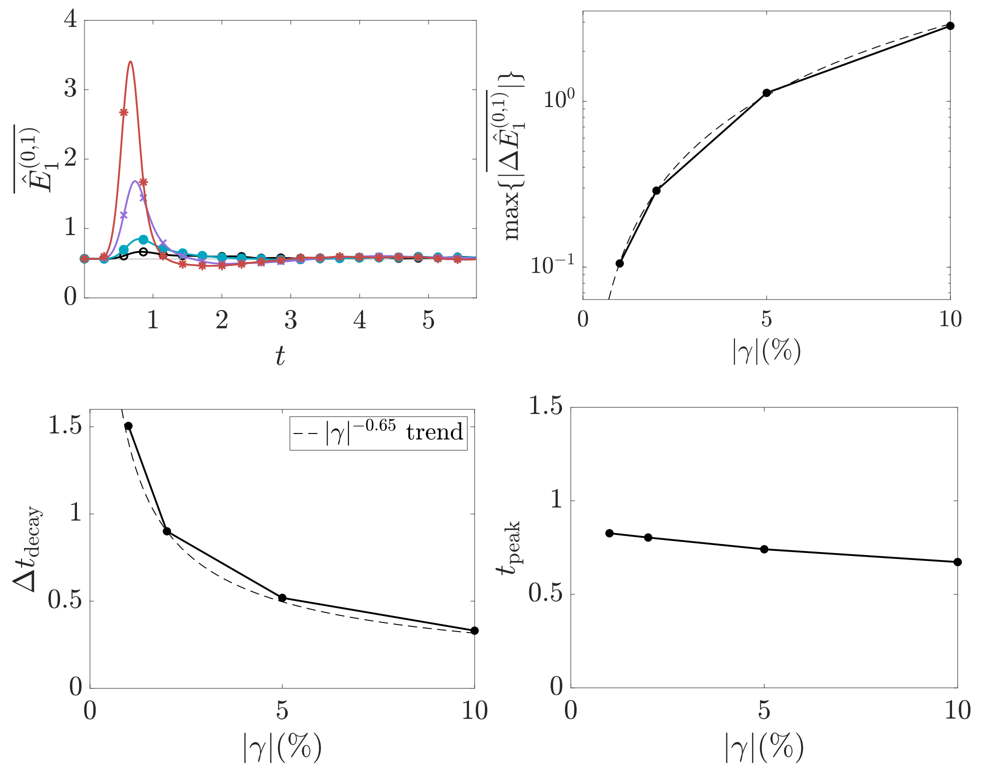

(c)

(d)

Figure 5.3: (a) Average streak energy as a function of time; the cases plotted are $\gamma = 1\%$ (black ○), $\gamma = 2\%$ (cyan ●), $\gamma = 5\%$ (purple ×), and $\gamma = 10\%$ (red ∗). (b) Streak energy peaks, (c) peak times, and (d) decay times as a function of γ. The dashed line represent the trends (b) $80.48|\gamma|^{1.44}$, and (d) $|\gamma|^{-0.65}$

quadratically, which indicates that the nonlinearities lead to the premature peaking of streak energy. The stronger the forcing, the faster the streak energy's growth rate, and the faster its decay. The peak times, t_{peak}, defined as the times at which the energies reach their maxima, decrease slightly with forcing amplitude, but are relatively constant compared to the decay times, Δt_{decay}, which we define as the time it takes for the energy to reduce from the peak to 10% of its peak (Figures 5.3(c, d)). Indeed, the differences in decay rate are more dramatic across the different forcing amplitude cases, and scale as $\Delta t_{\text{decay}} \sim |\gamma|^{-0.65}$. We note that all fully-coupled simulations decay significantly faster ($\Delta t_{\text{decay}} \approx 1$) than the linear response ($\Delta t_{\text{decay}} \approx 15$).

To measure the proportion of the linearly-amplified energy captured by the forced simulations, we compute an ensemble-averaged forcing efficiency, or effective am-

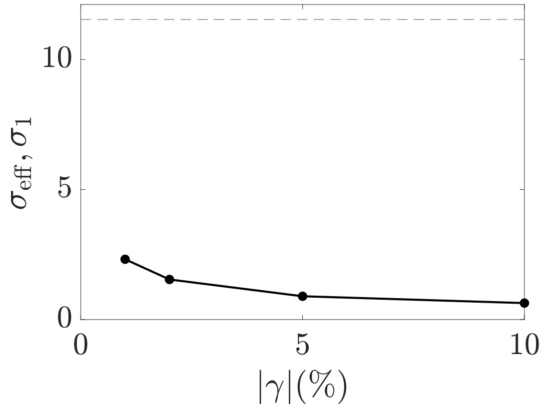

Figure 5.4: Effective amplification σ_{eff} (solid) and σ_1 (dashed).

plification, which we define to be

$$\sigma_{\text{eff}} = \left(\int_0^T \frac{\overline{\Delta \hat{E}^{(0,1)}}}{|\kappa|^2/2} \text{d}t \right)^{1/2} . \tag{5.7}$$

This is analogous to $\sigma_1 = \max_{\tilde{\boldsymbol{f}}} \|\tilde{\boldsymbol{H}}^{(0,1)} \boldsymbol{B} \tilde{\boldsymbol{f}}\|_2 / \|\tilde{\boldsymbol{f}}\|_2$, where the numerator reflects the energy contained in the velocity perturbation field, and the denominator corresponds to the forcing amplitude. The computed σ_{eff} is shown in Figure 5.4. The forcing efficiencies decrease with the intensity of the forcing, and all effective amplifications are lower than $\sigma_1 = 11.54$. This indicates that, for smaller resolvent forcing amplitudes, more of the forcing energy is linearly converted into streak energy. For higher values of γ, nonlinear interactions that scale superlinearly curtail the growth of the response mode—the integrated action of which scales linearly with γ in the linearized setting—and hinder the effectiveness of the resolvent forcing mode.

Comparison of the velocity deviation with the linear response

To visualize the alignment of the velocity fluctuation fields with the linear response mode across all wall normal heights, we plot the contours of $|\overline{\Delta \hat{u}^{(0,1)}/\kappa}|$, *i.e.* the magnitude of the $\hat{u}_1^{(0,1)}$ deviations normalized by the forcing coefficient κ, along with the contours of the linear resolvent response modes (Figure 5.5). We note that $\Delta \hat{u}^{(0,1)}$ is divided by the complex value of κ prior to ensemble averaging so as to align the phases of the forcing (Chapter 5.2) across the ensemble members. At earlier times ($t < 0.7$), the responses for both the $\gamma = 1\%$ and $\gamma = 10\%$ cases are similar to the linear mode. The strongly-forced case, however, quickly reverts to the unforced channel flow statistics beyond an eddy turnover time unit. In contrast, the lightly forced case of $\gamma = 1\%$ exhibits a longer-lasting velocity deviation, especially

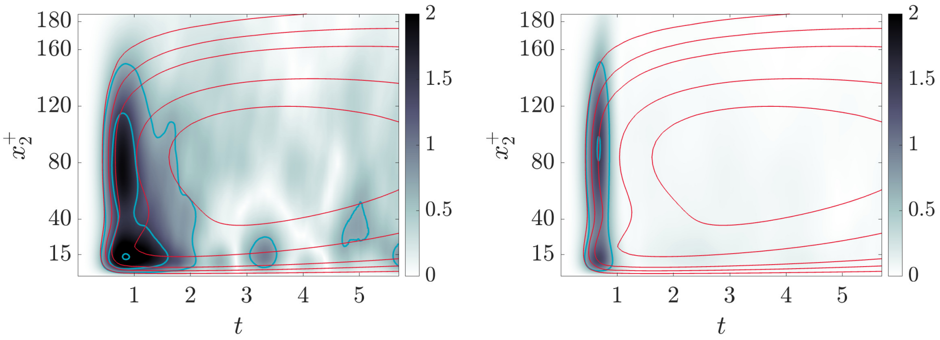

(a)

(b)

Figure 5.5: Average deviation in the streamwise velocity of the (0, 1)-Fourier mode, $\overline{|\Delta\hat{u}^{(0,1)}/\kappa|}$, for the (a) $\gamma = 1\%$ and (b) $\gamma = 10\%$ cases. The contours correspond to 7%, 15%, 25%, 75%, and 90% of the maximum value of $\sigma_1\boldsymbol{\psi_1}$. The lines represent the forced DNS case (blue), and the resolvent response (red).

in the near wall region ($x_2^+ < 15$). To more closely investigate how the agreement of the forced simulations and the optimal linear response varies with x_2^+, we show $\Delta\hat{u}_1^{(0,1)}$ at two wall-normal heights, along with the linear response at those heights (Figure 5.6). At both wall-normal locations, the initial growth rates are similar to the linear case for all γ, and we obtain good collapse prior to $t \approx 0.7$. However, the streak velocities peak earlier and decay more quickly for larger forcing amplitudes. For a fixed forcing amplitude, we note that $\Delta\hat{u}^{(0,1)}$ diverges from the optimal linear response around the same time at both wall-normal locations plotted in Figure 5.6, but the agreement between the forced simulations and the optimal linear response turns out better in the near-wall region. As x_2^+ moves closer to the wall, the growth rate due to linear mechanisms increases, and $\Delta\hat{u}_1^{(0,1)}$ manages to recover more of the linearly-amplified energy before decaying due to nonlinear effects.

Optimality of resolvent forcing

We compare the results of forcing using the principal resolvent forcing mode $\boldsymbol{\phi_1}$, the first suboptimal mode $\boldsymbol{\phi_3}$, and the random mode $\boldsymbol{\phi_{\mathrm{rand}}}$. We see that the streak energy grows to higher peak when the minimal flow unit is forced by $\boldsymbol{\phi_1}$ than when forced by $\boldsymbol{\phi_3}$ (Figure 5.7). In both cases, the minimal flow unit is much more responsive compared to the case with random forcing. This suggests that resolvent analysis identifies a forcing structure to which the minimal flow unit is indeed sensitive, even when governed by the fully nonlinear Navier-Stokes equations. The advantage of the optimal forcing mode, however, is significantly reduced. The

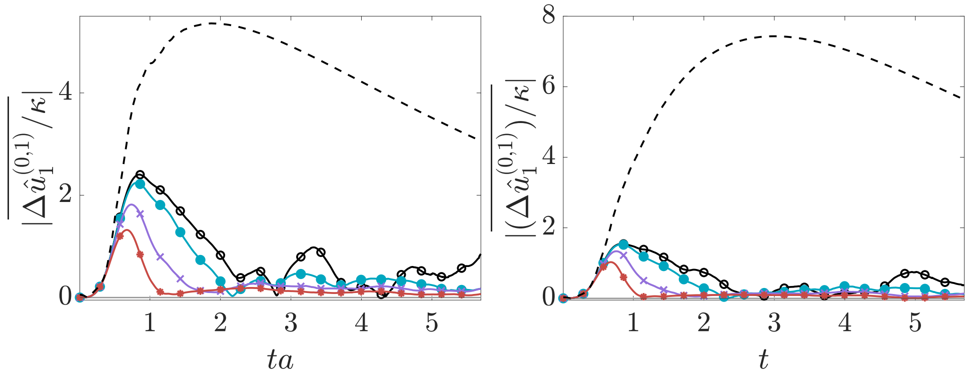

(a) (b)

Figure 5.6: Average deviation in the streamwise velocity of the $(0, 1)$-Fourier mode at $x_2^+ \approx 16$ (a) and $x_2^+ \approx 39$ (b). The cases plotted are $\gamma = 1\%$ (black $\circ$), $\gamma = 2\%$ (cyan $\bullet$), $\gamma = 5\%$ (purple $\times$), $\gamma = 10\%$ (red $*$), and the linear response mode $\sigma_1 \boldsymbol{\psi_1}$ (black, dashed).

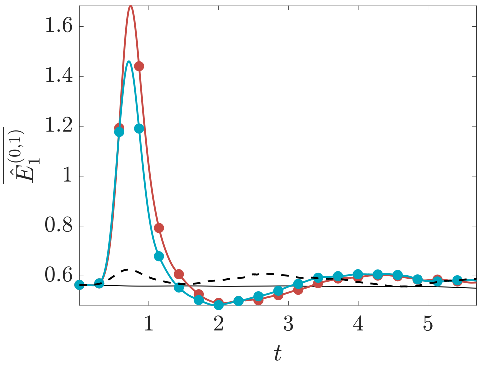

Figure 5.7: Average streak energy for cases forced by $\boldsymbol{\phi_1}$ (red $*$), $\boldsymbol{\phi_3}$ (cyan $\bullet$), and $\boldsymbol{\phi_{\text{rand}}}$ (dashed black). The unforced case is shown in black.

effective amplifications, σ_{eff} in DNS forced by $\boldsymbol{\phi_1}$ and $\boldsymbol{\phi_3}$ differ only by a factor of 1.03, whereas $\sigma_1/\sigma_3 = 2.16$. Though the initial growth of the streak energy is faster for the case forced by $\boldsymbol{\phi_1}$, the induced streak in both resolvent-forced cases triggers nonlinear effects at roughly the same time. These quickly clip the transient growth of the induced streaks and drain energy from the actuated mode before the differences between the responses to $\boldsymbol{\phi_1}$ and $\boldsymbol{\phi_3}$ can deepen.

We remind the reader that the mean profile is fixed by an additional forcing $\mathscr{F}$ which removes the $(0, 0)$ contribution to $\partial \boldsymbol{u}/\partial_t$ at every time step. Freezing the mean replenishes the energy in the $(k_1, k_3) = (0, 0)$ mode and preserves the energy transfer mechanism to the resolvent response mode. In other words, allowing the mean profile to vary may reduce the effectiveness of the forcing mode, since the

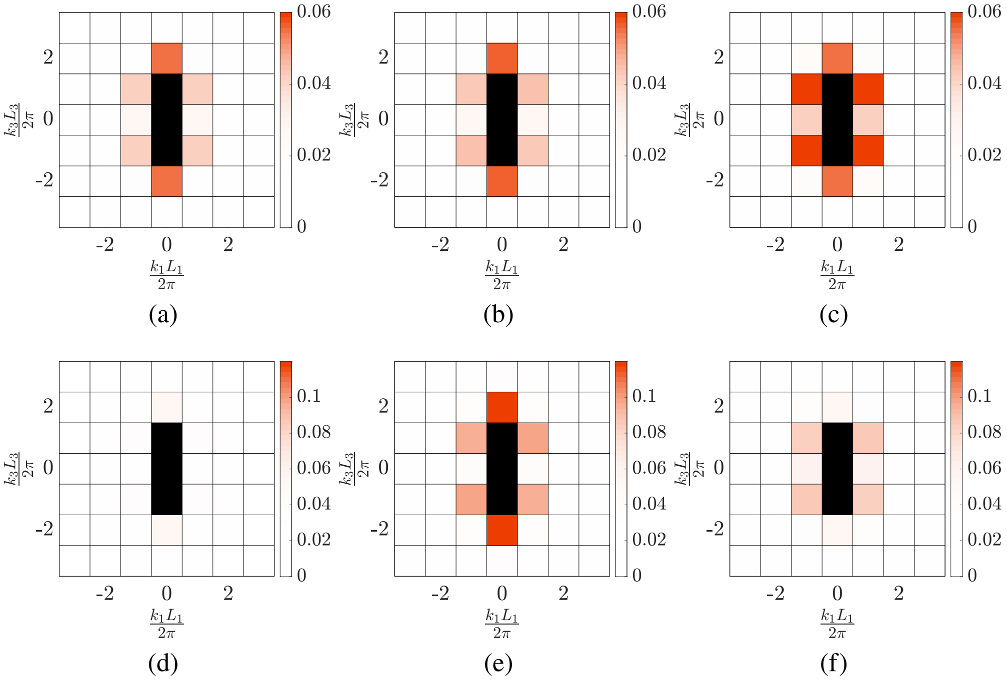

Figure 5.8: Integrated streamwise spectral energy content $\overline{[|\hat{u}_1^{(n_1,n_3)}|^2]}/2$ for $\gamma = 2\%$ (top) and $\gamma = 10\%$ (bottom). The spectra shown are at times $t = 0$ (left), $t = 0.6$ (middle) and $t = 1.2$ (right). The energy contained in the $(0,0)$, $(0,1)$, and $(0,-1)$–modes (black) are excluded for clarity.

mode is only optimal for the mean profile without forcing. This is observed in Bae et al. (2021): subtracting the contribution of the resolvent forcing mode from the nonlinear term succeeds at reducing the turbulent kinetic energy initially, but this effect fades after $t \approx 12$ as the mean flow is modified. However, our injected forcing has a short extent in time ($t \approx 1.5$), and we do not expect the initial linearly driven growth of the induced response mode to change much whether we fix the mean profile or not. Though not shown, the streak energy profile obtained for $\gamma = 5\%$ and an unfixed mean velocity is indeed close to what is shown in Figure 5.3(a).

Spectra

We compute the x_2–integrated streamwise and spanwise spectra for $\gamma = 2\%$ and $\gamma = 10\%$, at the initial time, right before the peak in streak energy ($t = 0.6$), and during the streak energy decay ($t = 1.2$). The results are shown Figure 5.8. Though not plotted, we note that the $(0, \pm 1)$–mode is the most dominant one across all times, accounting for $30\% - 70\%$ of the total turbulent energy over the entire simulated time horizon. For all forcing amplitudes, though only the $\gamma = 2\%$ and $\gamma = 10\%$ cases are

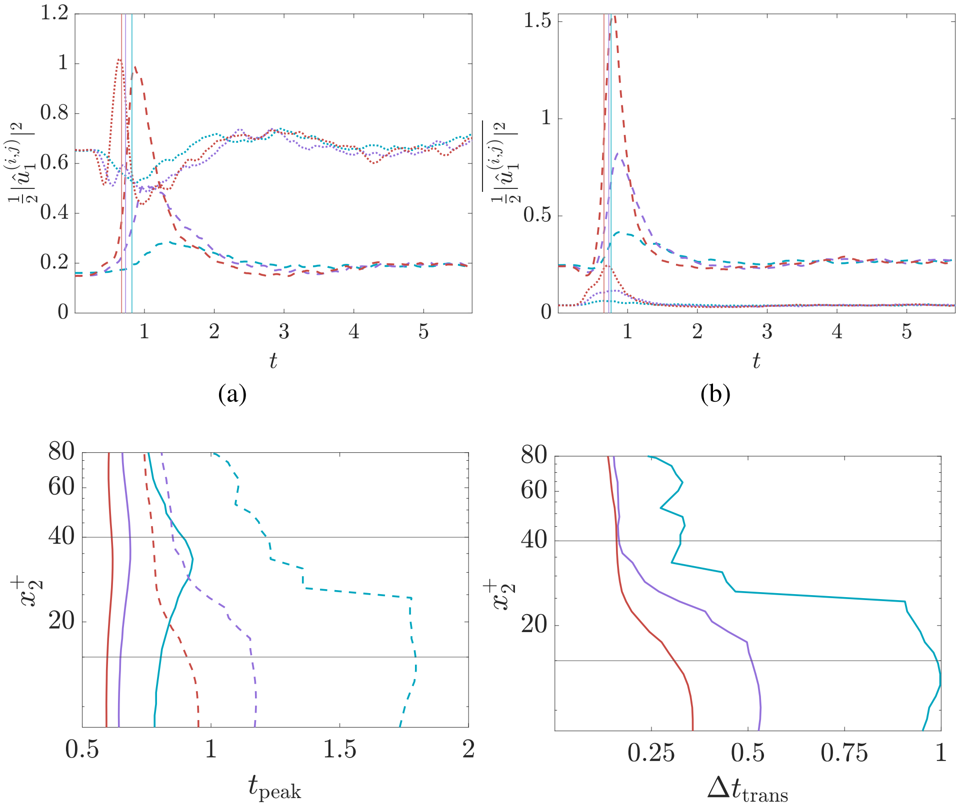

(a) (b)

(c) (d)

Figure 5.9: Streamwise spectral energy content at (a) $x_2^+ \approx 16$ and (b) $x_2^+ \approx 39$ for the $(0, \pm 2)$–Fourier mode (dotted lines) and the $(\pm 1, \pm 1)$–Fourier mode (dashed lines). (c) Energy peak times for the $(0, \pm 1)$–mode (solid) and the smaller scales (dashed) cases. (d) Timescale for the cross-scale energy transport. Colors indicate $\gamma = 2\%$ (blue), $\gamma \approx 5\%$ (purple), and $\gamma = 10\%$ (red). The vertical lines in (a) and (b) represent the local peaks of $|\hat{u}_1^{(0,1)}|$. The horizontal black lines in (c) and (d) represent $x_2^+ = 15$ and $x_2^+ = 40$, which delineate the buffer layer.

shown, the behavior of the non-actuated modes is similar for all γ: the energy of the non-actuated modes grows during the decay of the $(0, 1)$–mode, with the $(0, \pm 2)$ and $(\pm 1, \pm 1)$–modes growing most significantly, which highlights their key role in exchanging energy with the actuated $(0, 1)$–mode. The share of total turbulent energy accounted for by the $(0, \pm 2)$ and $(\pm 1, \pm 1)$–modes is roughly constant across all forcing amplitudes, amounting to approximately $9 - 10\%$ and $7 - 8\%$ at their peaks, respectively. Some differences do exist across forcing amplitudes: the transient behavior of the $(0, \pm 2)$–mode appears more sensitive to the value γ. For the lightly forced case, the energy of the $(0, \pm 2)$–mode continues to grow beyond t_{peak}, while for the strongly forced case, the energy of the mode peaks soon after the peak in streak energy before decaying rapidly and ceding to the $(\pm1,\pm1)$–mode. This suggests that the $(0,\pm2)$–mode tends to grow faster and peak earlier as the forcing amplitude increases. The particular sensitivity of the integrated energy of the $(0,\pm2)$–mode to forcing amplitude can be partially explained by the fact that it is fed by the dyadic interaction involving the self-interaction of the actuated $(0,\pm1)$–mode. The nonlinear energy transfer from the $(0,\pm1)$–mode to secondary scales is discussed in more detail in the next section.

The instantaneous growth and decay of the two preferred secondary modes, the $(0,\pm2)$– and $(\pm1,\pm1)$–modes, at different wall-normal locations can be seen in Figures 5.9(a, b). Closer to the wall, the energy of the $(0,\pm2)$–mode first decreases during the growth of the $(0,\pm1)$–mode, then exhibits two peaks for the larger amplitude cases, one coinciding with the peak of the $(0,\pm1)$–mode, and one much later at around $t \approx 3$, as the energy of the mode reverts back to its initial state. The first peak, which is only visible for the higher amplitude cases, occurs earlier as γ increases, while the later peak occurs roughly at the same time across forcing amplitudes. The behavior of the $(\pm1,\pm1)$–mode is simpler and its energy peaks earlier as the forcing amplitude increases. Farther away from the wall, the energy peaks of both the $(0,\pm2)$– and $(\pm1,\pm1)$–modes depend little on γ and occur roughly at the same time for all forcing amplitudes, at $t \approx 0.8$ and $t \approx 1$, respectively. Thus, the energy of the $(0,\pm2)$– and $(\pm1,\pm1)$–modes is similarly influenced by x_2 and γ: while the forcing magnitude γ affects the growth time scale of the secondary modes, causing their energy to peak earlier as it increases, the wall-normal location modulates the sensitivity of these modes to γ.

To better visualize the cross-scale energy transport time scales, we plot the streamwise energy peak times for the $(0,\pm1)$–mode and the smaller scales as a function of x_2^+ and for different forcing amplitudes (Figure 5.9(c)). Across all wall-normal heights, increasing the forcing amplitude causes the energy of both the $(0,\pm1)$–mode and the smaller scales to peak earlier. For all forcing amplitudes, the peak times for the $(0,\pm1)$–mode and the smaller scales vary inversely with x_2^+. For the $(0,\pm1)$–mode, they are roughly constant with x_2^+ in the near-wall region, increase slightly in the buffer layer as we move farther away from the wall, and plateau in the outer region of the flow. For the non-actuated modes, the peak times are also constant in the near-wall region, but decrease dramatically within the buffer layer as x_2^+ increases, before leveling off in the outer region. The growth of the smaller scales is thus more sensitive to both forcing amplitude and distance to the wall than the actuated $(0, \pm 1)$–mode.

We define the timescale for cross-scale energy transport, Δt_{trans}, as the time delay between the energy peaks of the $(0, \pm 1)$–modes and the smaller scales; its dependence on x_2^+ is mostly determined by the energy peak time for the smaller scales (Figure 5.9(d)). Interestingly, though a larger forcing amplitudes accelerates the energy transport from the $(0, \pm 1)$–mode to smaller scales for all wall normal heights, the sensitivity of Δt_{trans} to forcing amplitude decreases as we move farther away from the wall. Indeed, in the outer regions of the flow, the transfer time scale converges to a value of approximately $\Delta t_{\text{trans}} \approx 0.18$ for high forcing amplitude. The plots in Figures 5.9(c, d) indicate two cross-scale energy transfer mechanisms: one for the near-wall region ($x_2^+ \leq 25$) which is highly dependent on γ, and one for the outer ($x_2^+ \geq 25$) region which is less dependent on γ. The outer region is already highly nonlinear, which allows for a rapid energy cascade from the actuated mode to smaller scales. Perturbing this region seems to have little effect on the time scale of this cross-scale energy transfer. Near the wall, linear mechanisms dominate; the $(0, \pm 1)$–mode, growing significantly under the action of the resolvent forcing term, greatly enhances the nonlinear interactions involving the mode and markedly changes the underlying energy transfer to secondary scales, which may explain the heightened sensitivity of Δt_{trans} to γ in the near-wall region.

To sum up, the time-localized principal mode obtained from windowed wavelet-based resolvent analysis is indeed more effective than a randomly generated forcing function at actuating the minimal flow unit. This effectiveness, however, is greatly reduced to nonlinear interactions that interrupt the transient growth of the principal response mode. The transfer of energy from the targeted length scale to secondary scales seems to proceed according to two different mechanisms, operating in two distinct wall-normal regions at different time scales. In the next section, we study this nonlinear energy transfer directly in an attempt to clarify this behavior.

5.4 Nonlinear energy transfer

The energy content of the secondary modes (Figures 5.8, 5.9) are the result of nonlinear interactions among all length scales. We wish to disentangle these interactions and focus on the nonlinear energy transfer that specifically drain energy from the actuated $(0, 1)$–mode. As in Symon et al. (2021) and Ding et al. (2025), we represent the nonlinear energy transfer from a mode (n_1, n_3) using the following term:

$$\hat{N}(n_1, n_3) = -\hat{u}_i^{(-n_1,-n_3)} \widehat{\frac{\partial u_i u_j}{\partial x_j}}^{(n_1,n_3)}. \tag{5.8}$$

We note that $(\cdot)^{(-k_1,-k_3)}$ refers to the complex conjugate of $(\cdot)^{(k_1,k_3)}$. The term $\hat{N}(n_1, n_3)$ satisfies

$$\begin{aligned} \int_0^2 \sum_{n_1} \sum_{n_3} \hat{N}(n_1, n_3) dy &= -\int_0^2 \overline{u_i \frac{\partial u_i u_j}{\partial x_j}}^{(0,0)} \\ &= \frac{1}{L_1 L_3} \int_0^2 \int_0^{L_3} \int_0^{L_1} u_i \frac{\partial u_i u_j}{\partial x_j} dx_1 dx_3 dx_2 \\ &= 0, \end{aligned} \tag{5.9}$$

due to continuity and the no-penetration boundary conditions at the walls. This indicates that the nonlinear transfer does not contribute to adding or removing energy from the system and simply redistributes energy between scales (Ding et al., 2025). We can express $\hat{N}(n_1, n_3)$ as a sum of contributions from interacting scales:

$$\hat{N}(n_1, n_3) = -\sum_{s_1} \sum_{s_3} \hat{u}_i^{(-n_1,-n_3)} \widehat{\frac{\partial u_i}{\partial x_j}}^{(s_1,s_3)} \hat{u}_j^{(n_1-s_1,n_3-s_3)}. \tag{5.10}$$

We refer to an individual contribution to the sum as $\hat{M}^{(n_1,n_3)}(s_1, s_3)$, defined below:

$$\hat{M}^{(n_1,n_3)}(s_1, s_3) = -2\mathfrak{Re}\left\{ \hat{u}_i^{(-n_1,-n_3)} \widehat{\frac{\partial u_i}{\partial x_j}}^{(s_1,s_3)} \hat{u}_j^{(n_1-s_1,n_3-s_3)} \right\}. \tag{5.11}$$

The term $\hat{M}^{(n_1,n_3)}(s_1, s_3)$ represents the energy transfer from the (n_1, n_3)–mode to the (s_1, s_3)–mode and satisfies the following properties:

$$\int_0^2 \hat{M}^{(n_1,n_3)}(s_1, s_3) dx_2 = -\int_0^2 \hat{M}^{(s_1,s_3)}(n_1, n_3) dx_2, \tag{5.12}$$

$$\int_0^2 \hat{M}^{(n_1,n_3)}(n_1, n_3) dx_2 = 0. \tag{5.13}$$

Equation (5.12) implies that the scale-to-scale energy transfer is conservative; equation (5.13) implies that it purely captures the energy transferred from one scale to a different scale and excludes self-interactions. We finally define $\Delta\hat{M}^{(n_1,n_3)}$ as $\hat{M}^{(n_1,n_3)} - \hat{M}_0^{(n_1,n_3)}$, where $\hat{M}_0^{(n_1,n_3)}$ is defined as equation (5.11) using the unforced velocity field $\boldsymbol{u_0}$.

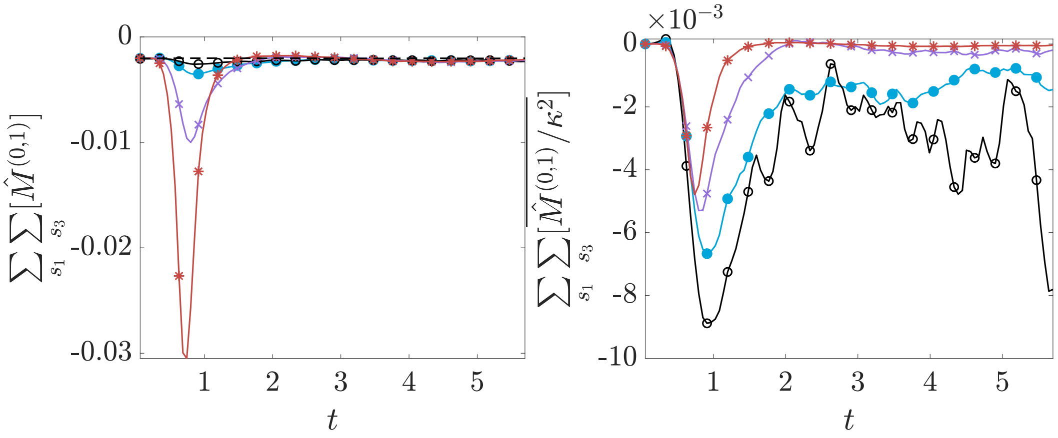

(a) (b)

Figure 5.10: (a) Integrated nonlinear energy transfer from the $(0, 1)$–mode to the non-forced modes; (b) integrated nonlinear energy transport from the $(0, 1)$–mode normalized by the forcing magnitude $|\kappa|^2$. The cases plotted are $\gamma = 1\%$ (black $\circ$), 2% (cyan $\bullet$), 5% (purple $\times$), and 10% (red $*$).

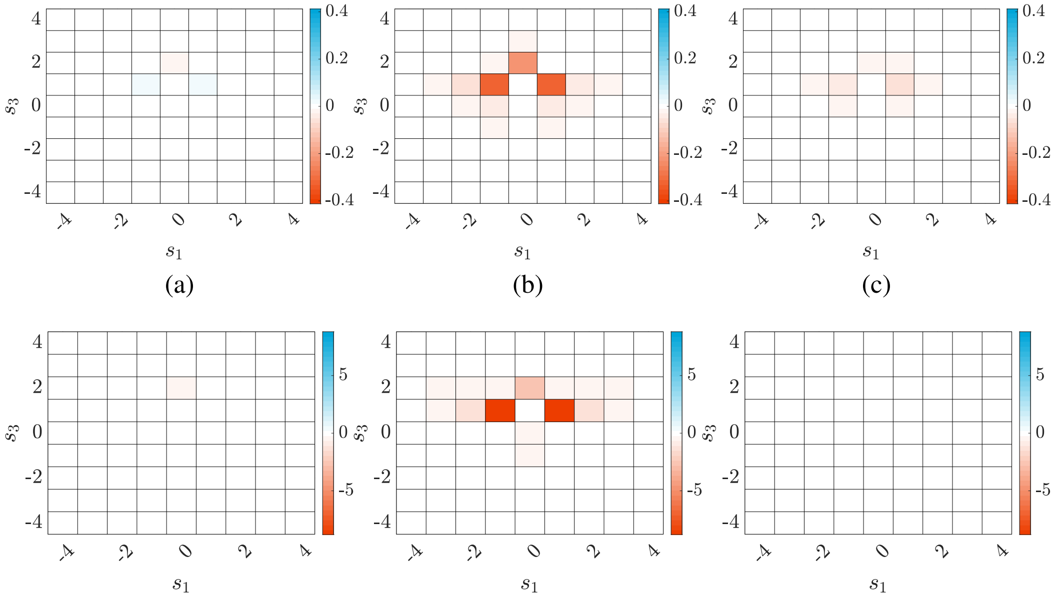

(a) (b) (c)

(d) (e) (f)

Figure 5.11: Nonlinear energy transfer $\Delta\hat{M}^{(0,1)}(s_1, s_3)$ for $\gamma = 2\%$ (a-c) and $\gamma = 10\%$ (d-f), at $t = 0.35$ (a, d), 0.74 (b, e), 2 (c, f).

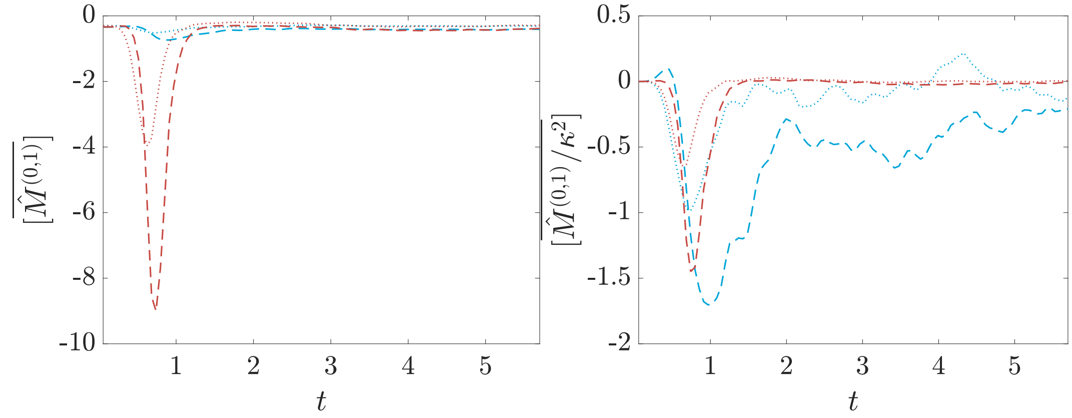

(a) (b)

Figure 5.12: (a) Integrated nonlinear energy transfer from the $(0,1)$–mode to the $(0,2)$–mode (...) and the $(1,1)$–mode ($--$); (b) integrated nonlinear energy transfer from the $(0,1)$–mode normalized by the forcing magnitude $|\kappa|^2$. The cases plotted are 2% (cyan) and 10% (red).

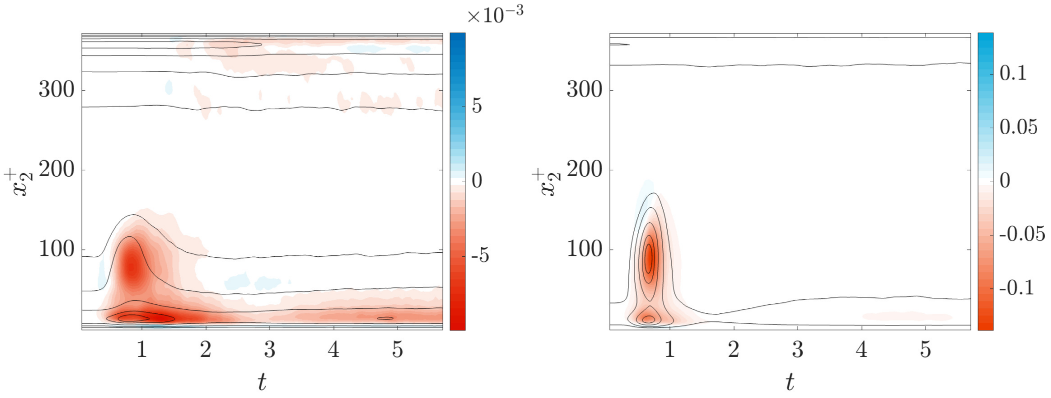

(a) (b)

Figure 5.13: (a) Total nonlinear energy transfer from the $(0,1)$–mode, *i.e.* $\sum_{s_1}\sum_{s_3}\overline{\Delta\hat{M}^{(0,1)}(s_1,s_3)}$. The cases plotted are for (a) $\gamma = 2\%$ and (b) $\gamma = 10\%$. The black lines are contours of $\overline{|\hat{u}_1^{(0,1)}|^2}/2$ and represent 10%, 25%, 50%, 75%, and 90% of the maximum value across x_2 and t.

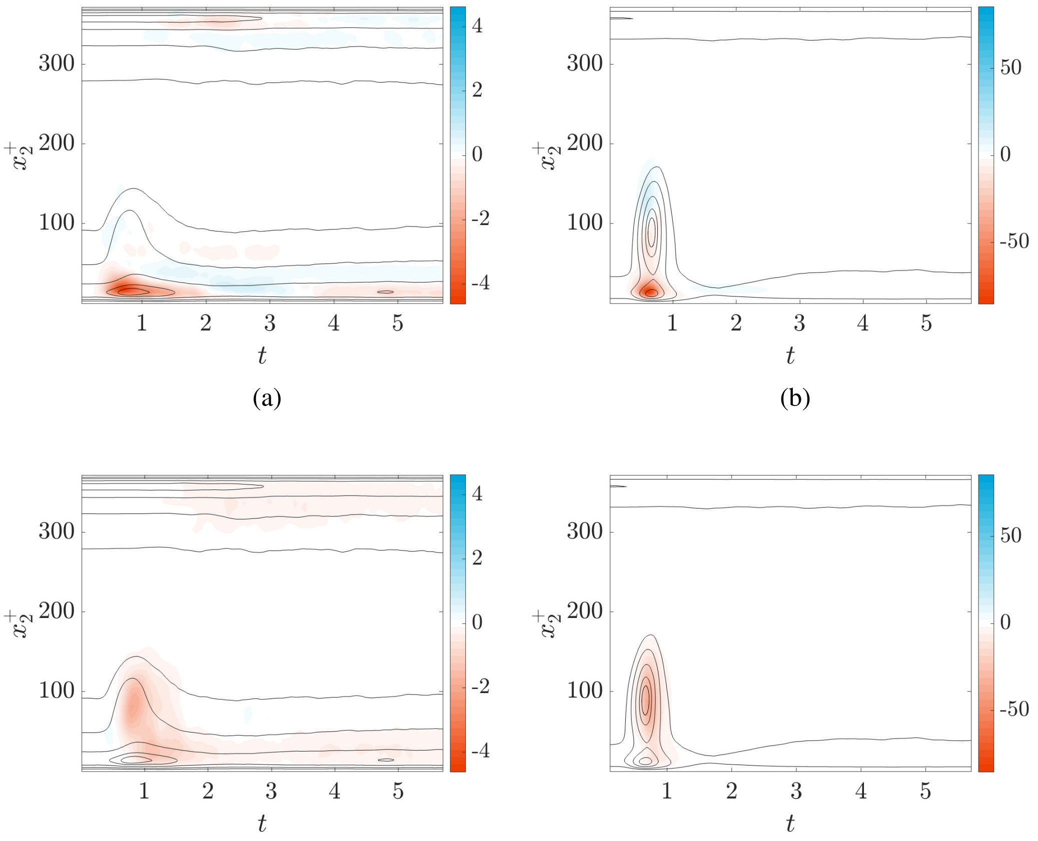

(a)

(b)

(c)

(d)

Figure 5.14: (a, b) $\overline{\Delta\hat{M}^{(0,1)}(0,2)}$ and (c, d) $\overline{\Delta\hat{M}^{(0,1)}(1,1)}$ in the $t-x_2$ plane. The cases plotted are for (a,c) $\gamma = 2\%$ and (b,d) $\gamma = 10\%$. The black lines are contours of $\overline{|\hat{u}_1^{(0,1)}|^2}/2$ and represent 10%, 25%, 50%, 75%, and 90% of the maximum value across x_2 and t.

Interacting modes

Figure 5.10 shows the total nonlinear transfer from the $(k_1L_1/(2\pi), k_3L_3/(2\pi)) = (0,1)$ mode integrated over the wall-normal direction. The integrated transfer is negative and confirms that nonlinear effects are indeed draining energy from the actuated scale. The trends in the plot echo the results in Figure 5.3(a): the larger the forcing term, the larger the integrated transfer to unforced scales. The total energy transfer tends to peak during the decay of the streak, approximately $t = 0.06 - 0.09$ later than the streak energy. Considering the total energy transfer normalized by forcing magnitude $|\kappa|^2$, we see that the plots collapse for all values of γ, for $t < 0.8$. The initial growth rate is the same across all forcing intensities and its magnitude scales with $|\gamma|^2$. The energy transfer mechanism at early times thus seems to

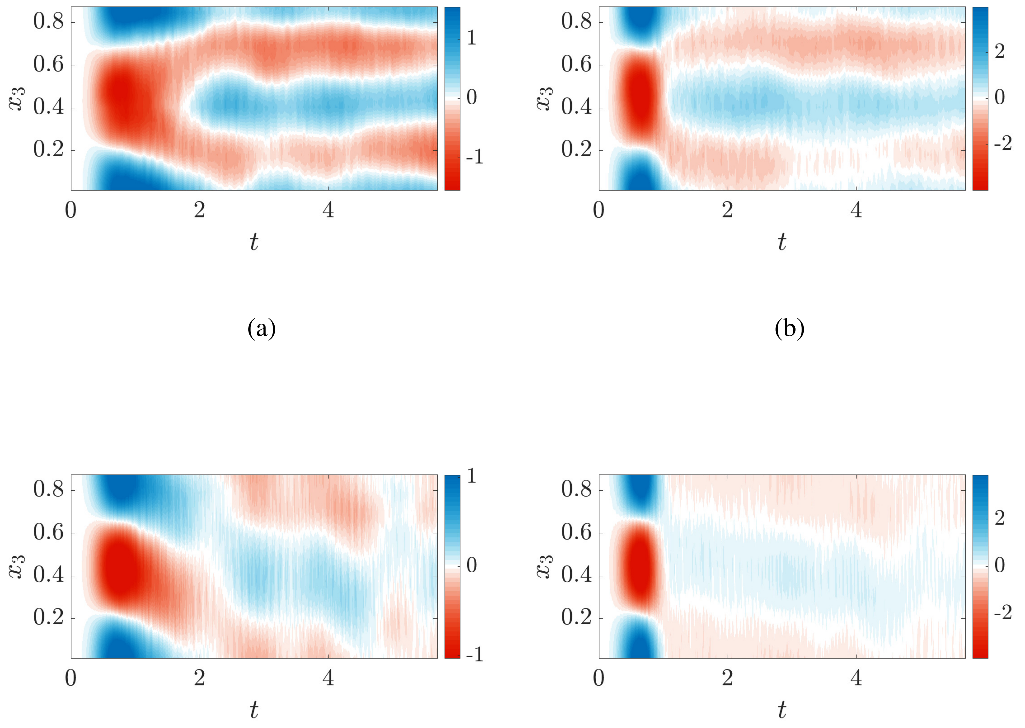

(a) (b)

(c) (d)

Figure 5.15: Ensemble-averaged streamwise velocity deviation $\overline{\Delta u_1}$ for (a, c) $\gamma = 2$‰ and (b, d) $\gamma = 10$‰. The results are for $x_1 = 0$ and two wall-normal heights: (a, b) $x_2^+ = 16$ and (c, d) $x_2^+ = 75$. Before ensemble averaging, the $(0, 1)$–mode for each ensemble member is multiplied by $\mathrm{e}^{-i\angle\kappa}$ to ensure their phase alignment.

be similar for all cases, regardless of forcing magnitude. The larger the forcing, however, the earlier the energy transfer reaches its maximum and starts its decay. At later times, additional multiscale effects, more prominent for the strongly forced cases, likely take over and help drain energy more efficiently from the $(0, 1)$–mode.

In Figure 5.11, we plot the streamwise-spanwise spectra for $\hat{M}^{(0,1)}(s_1, s_3)$ at different times. Only wavenumbers corresponding to $n_1, n_3 \in [-4, 4]$ are shown for clarity; the remaining wavenumbers interact negligibly with the $(0, 1)$–mode. We observe that $\hat{M}^{(0,1)}(s_1, s_3) \approx \hat{M}^{(0,1)}(-s_1, s_3)$. Since the target mode extends the entire length of the channel, the streamwise phase of the interacting modes matters little once the results are averaged over the ensemble of simulations. The figure reveals that the nonlinear energy transfer is dominated by energy transfer to the $(0, 2)$ and

$(1, 1)$–modes. This pattern is consistent across forcing intensities, though only the cases for $\gamma = 2\%$ and $\gamma = 10\%$ are shown. The qualitatively similar results across forcing magnitudes highlight the privileged role of the $(0, 2)$– and $(1, 1)$–modes at exchanging energy with the actuated mode. Since the transfer to the $(0, 2)$–mode results from the self-interaction of the actuated mode, the importance of this particular scale is not surprising. Figure 5.12 shows the x_2–integrated energy transferred to the $(1, 1)$ and $(0, 2)$ modes only. As in Figure 5.10(b), the initial growth rate of the magnitude-normalized quantities across forcing amplitudes, with the plot for $\gamma = 10\%$ peaking and starting its decay earlier than for $\gamma = 2\%$. Another notable observation is that, across forcing amplitudes, the energy transfer to the $(0, 2)$–mode occurs at a faster time-scale than the transfer to the $(1, 1)$–mode.

In Figure 5.13, we study the spatial distribution of the nonlinear energy transfer term $\hat{M}^{(0,1)}$. We observe that, for $\gamma = 2\%$ and $\gamma = 10\%$, the additional nonlinear transfer to other scales due to the induced streak is centered on two wall-normal locations, $x_2^+ \approx 16$ located in the buffer layer, and $x_2^+ \approx 75$ located in the outer region. This is consistent across all forcing magnitudes. The presence of two hubs of energy transfer echo the results in Figure 5.9(d), which similarly shows two distinct regions each characterized by a time scale of energy transfer from the $(0, 1)$–mode to smaller scales.

In Figure 5.14, we plot the nonlinear energy transfer to the $(0, 2)$– and $(1, 1)$–modes, for $\gamma = 2\%$, 10%. The figure reveals that the transfer to the $(0, 2)$–mode accounts for the transfer at $x_2^+ \leq 25$, while the transfer to the $(1, 1)$–mode accounts for the transfer at $x_2^+ > 25$. In the buffer layer, the forced $(0, 1)$–mode thus tends to transfer its energy to a mode that is twice periodic in the spanwise direction; the induced streak splits into two branches, which can be seen in Figures 5.15(a, b). In the outer region, the nonlinear energy transfer favors the $(1, 1)$–mode, suggesting that the induced streak breaks up along the streamwise direction. This is seen in Figures 5.15(c, d), which show the streak meandering but not splitting into two branches as for $x_2^+ = 16$. We note that the transfer from the $(0, 1)$–mode to the $(0, 2)$–mode is due to the self-interaction of the actuated mode, and the term $\hat{u}^{(0,-1)}$ is squared in the expression for $\hat{M}^{(0,1)}(0, 2)$ (equation 5.11). This along with the fact that the energy transfer to the $(0, 2)$–mode is predominant in the near-wall region explains the increased sensitivity of the energy transfer time scale Δt_{trans} to γ for $x_2^+ \leq 25$ (Figure 5.9(d)). More specifically, a higher of γ disproportionately intensifies the transfer of energy to the $(0, 2)$–mode, causing the nonlinear transfer of energy near

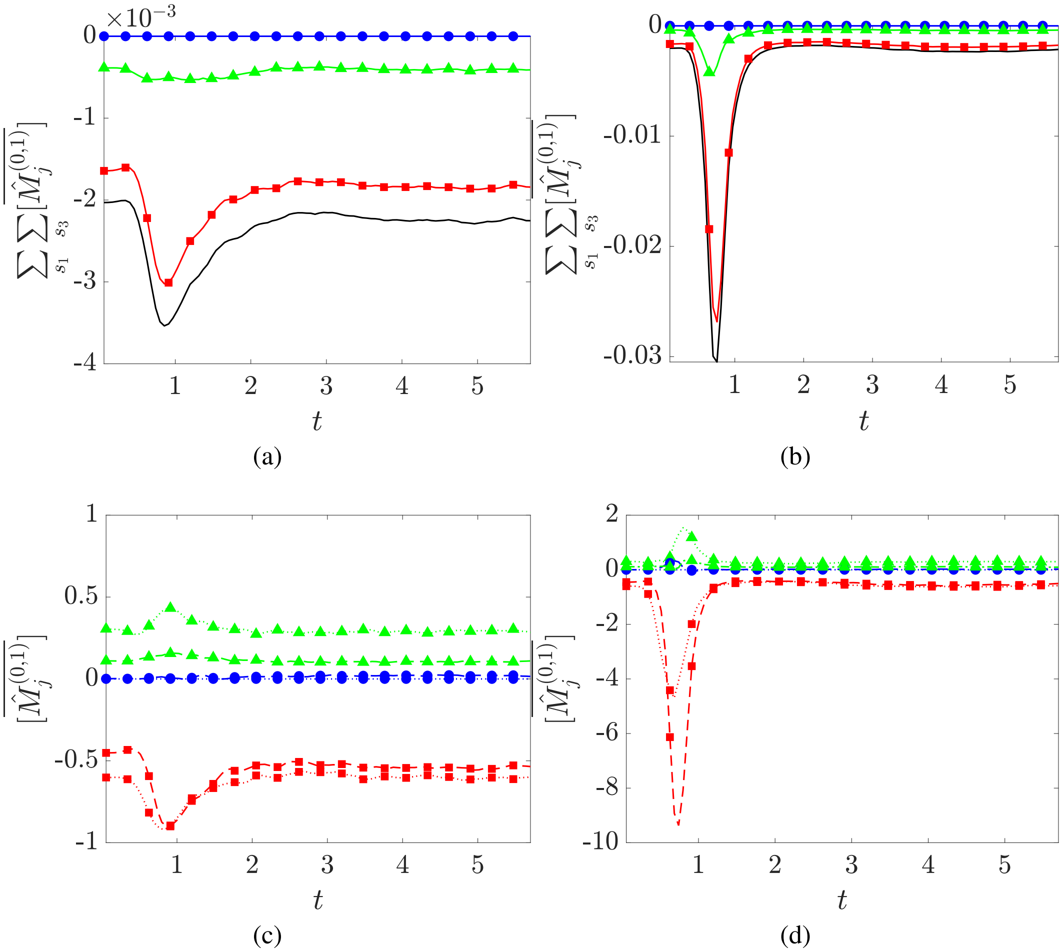

Figure 5.16: Nonlinear energy transfer from the $(0,1)$–mode to unforced modes, broken down by streamwise (blue $-\bullet$), wall-normal ($-\blacktriangle$) and spanwise ($-\blacksquare$) contributions. The cases plotted are (a, c) $\gamma = 2\%$ and (b, d) $\gamma = 10\%$. Plots (a) and (b) represent the contributions to the total nonlinear energy transport from the $(0,1)$–mode, with the black line representing the sum of the contributions; plots (c, d) represent the transfer to the $(0,2)$– and $(1,1)$–modes, denoted by $(\cdots)$ and $(--)$, respectively.

the wall to occur earlier—closer to the focus of $\hat{M}^{(0,1)}(0,2)$—and decreasing Δt_{trans}.

Mechanism of nonlinear energy transfer

To shed light on the mechanism of this nonlinear energy transfer, we split the nonlinear transfer $\hat{M}^{(0,1)}(s_1, s_3)$ into the terms that, respectively, reflect the contributions of the streamwise, spanwise, and wall-normal nonlinear advection. Specifically, in order to study the nonlinear energy transfer from a mode (n_1, n_3) due to streamwise nonlinear advection—henceforth referred to as NLT$_1$ ("NonLinear Transfer,

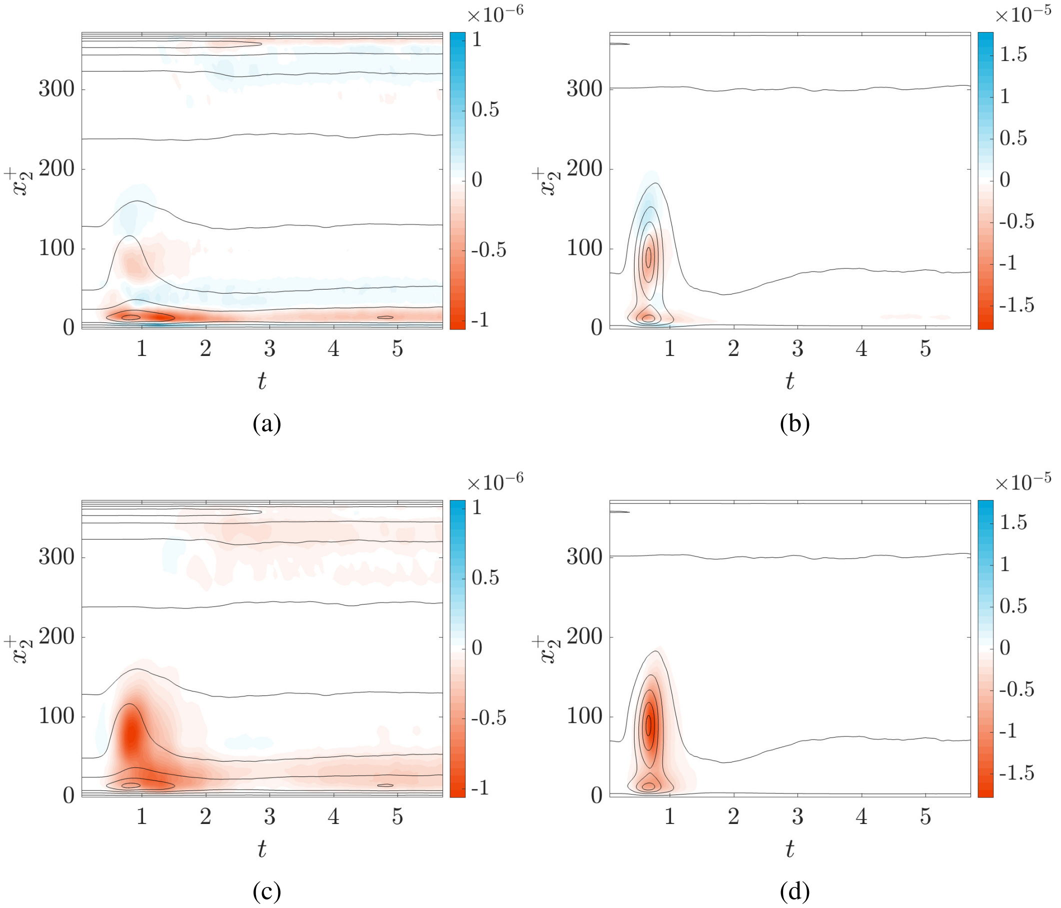

(a) (b) (c) (d)

Figure 5.17: Nonlinear energy transfer from the $(0,1)$–mode split by NLT$_2$ and NLT$_3$ contributions: (a, b) $\overline{\Delta\hat{M}_2^{(0,1)}}$ and (c, d) $\overline{\Delta\hat{M}_3^{(0,1)}}$. The cases shown are for (a,c) $\gamma = 2\%$ and (b,d) $\gamma = 10\%$. The black lines are contours of $\overline{|\hat{u}_1^{(0,1)}|^2/2}$ and represent 10%, 25%, 50%, 75%, and 90% of the maximum value across x_2 and t.

x_1")—we define $\hat{M}_1^{(n_1,n_3)}(s_1,s_3)$ as

$$\hat{M}_1^{(n_1,n_3)}(s_1,s_3) := -2\mathfrak{Re}\left\{\hat{u}_i^{(-n_1,-n_3)}\,\widehat{\frac{\partial u_i}{\partial x_1}}^{(s_1,s_3)}\,\hat{u}_1^{(n_1-s_1,n_3-s_3)}\right\}. \tag{5.14}$$

We similarly define $\hat{M}_2$ and $\hat{M}_3$ to study NLT$_2$ and NLT$_3$, the nonlinear energy transfer due to wall-normal and spanwise gradients self-advection, respectively.

Figure 5.16 shows that the energy transfer due to the coupling with the spanwise velocity component dominates the total energy transfer to other scales, even before the growth of the injected mode and after the mode completely decays for $t > 2$. During the growth of the injected mode, the NLT$_3$ term grows significantly more than the transfer due to self-advection in the streamwise and wall-normal directions.

This demonstrates the unique role of NLT_3 in transferring energy to secondary scales and restoring the system to its unforced state. This behavior is consistent across forcing amplitudes, though only $\gamma = 2\%$ and $\gamma = 10\%$ are shown. The dominance of the NLT_3 contributions also holds for the $(0,2)$ and $(1,1)$–modes individually (Figures 5.16(c, d)). We do note that the NLT_2 is relatively important for the $(0,2)$–mode. The induced streak thus tends to shed its energy to secondary modes via spanwise self-advection. We note that these results match those found in Markeviciute and Kerswell (2024), which computes a streak structure via optimal transient growth analysis then studies the growth of secondary instabilities added to the streak. Authors find that suppressing the pushover mechanism, *i.e.* the spanwise advection of the secondary perturbation due to the streak, prevents the growth of these secondary instabilities. Thus, both this work and Markeviciute and Kerswell (2024) agree that coupling via spanwise gradients dominate the interaction between the streak and secondary modes.

Additionally, by considering the wall-normal variations (Figure 5.17), we see that spanwise self-advection is the primary pathway across all wall-normal heights by which the forced $(0,1)$–mode sheds its energy. This is consistent across all forcing magnitudes, though only the cases for $\gamma = 2\%$ and $\gamma = 10\%$ are shown. For the lightly forced case $\gamma = 2\%$, we do note a significant NLT_2 contribution at $x_2^+ \approx 18$, (Figure 5.17 a), but as γ increases, the NLT_2 contribution is quickly overtaken by the NLT_3. We note that $x_2^+ \approx 18$ corresponds to the section of the wall-normal grid dominated by the transfer to the $(0,2)$–mode, *i.e.* the triadic interaction most sensitive to γ due to the self-interaction of the actuated mode. The growth of secondary instabilities due to push-over occurs locally at both foci of nonlinear energy transfer, and both the $(1,1)$– and $(0,2)$–modes benefit from this energy transfer mechanism.

Quasi-linear approximation

In this section, we seek to determine whether the instantaneous behaviors of the nonlinear energy transfer can be simply modeled by the interactions of the principal response mode with the "background" turbulence—that is, the turbulence frozen in its state at $t = 0$. By neglecting subsequent nonlinear feedback, the velocity field after the injection of the mode can be represented as $\boldsymbol{u}_\psi := \boldsymbol{u_0} + \kappa\sigma_1\boldsymbol{\psi_1}\exp(\mathrm{i}2\pi/L_3) + \kappa^*\sigma_1\boldsymbol{\psi_1}^*\exp(-\mathrm{i}2\pi/L_3)$. Using this field, we define the following nonlinear energy transfer term for the quasi-linear field analogously to equation (5.11):

$$\widetilde{M}^{(n_1,n_3)}(s_1,s_3) := -2\mathfrak{Re}\left\{ \hat{u}_{\psi,i}^{(-n_1,-n_3)} \widehat{\frac{\partial u_{\psi,i}^{(s_1,s_3)}}{\partial x_j}} \hat{u}_{\psi,j}^{(n_1-s_1,n_3-s_3)} \right\} \tag{5.15}$$

where $u_{\psi,i}$ is the i^{th} component of $\boldsymbol{u}_\psi$. This term captures the nonlinear energy transfer from the (k_1,k_3)–mode to the (s_1,s_3)–mode due to interactions of the injected mode with the background turbulence and ignoring the self-interactions of $\boldsymbol{u}_\psi$ at every time-step. We can thus view the term $\widetilde{M}^{(k_1,k_3)}$ as a quasi-linear model of the nonlinear energy transfer. We define the quantities representing the NLT$_1$, NLT$_2$ and NLT$_3$ contributions for the $\boldsymbol{u}_\psi$ field as

$$\widetilde{M}_1^{(n_1,n_3)}(s_1,s_3) := -2\mathfrak{Re}\left\{ \hat{u}_{\psi,i}^{(-n_1,-n_3)} \widehat{\frac{\partial u_{\psi,i}}{\partial x_1}}^{(s_1,s_3)} \hat{u}_{\psi,1}^{(n_1-s_1,n_3-s_3)} \right\}. \tag{5.16}$$

We respectively dub these terms QLT$_1$, QLT$_2$, and QLT$_3$ (“QuasiLinear Transfer, x_i") to distinguish them from NLT$_1$, NLT$_2$, and NLT$_3$. Figure 5.18 shows the quasi-linear estimates for the nonlinear energy transfer to the $(0,2)$– and $(1,1)$–modes, normalized by forcing amplitude. For the lightly forced case of $\gamma = 2\%$ (Figures 5.18(a, c)), the quasi-linear predictions for both the $(0,2)$– and $(1,1)$–modes initially match the DNS results, especially for $t < 1$. For $\gamma = 10\%$, the quasi-linear interactions do not match the DNS. Nevertheless, the region of energy loss to the $(1,1)$–mode is well predicted by $\widetilde{M}^{(0,1)}$ across all forcing amplitudes.

In Figure 5.19, we observe the quasi-linear estimates of the QLT$_1$, QLT$_2$, and QLT$_3$ contributions. We see that the quasi-linear estimates for the transfer to mode $(0,2)$ can roughly predict a strongly negative QLT$_3$ component for the lightly forced system at early times, but fail to do so for later times. For large forcing amplitudes, the quasi-linear mode performs poorly for all times, and even reverses the observed trends for the QLT$_2$ and QLT$_3$ components of the nonlinear transfer. This suggests that the growth of the $(0,2)$–mode cannot be explained by the instantaneous nonlinear interaction of the streak with the background turbulence. In the near-wall region where streak splitting occurs, we suspect that other transient mechanisms dominate the energy growth of mode $(0,2)$, such as linearly driven transient algebraic growth, which is responsible for amplifying the injected resolvent mode at early times. In contrast, the quasi-linear estimates for the transfer to mode $(1,1)$ qualitatively match the behavior of the DNS and reveal a strongly negative QLT$_3$ contribution and a weakly positive QLT$_2$ contribution. Outside the buffer layer, the instantaneous

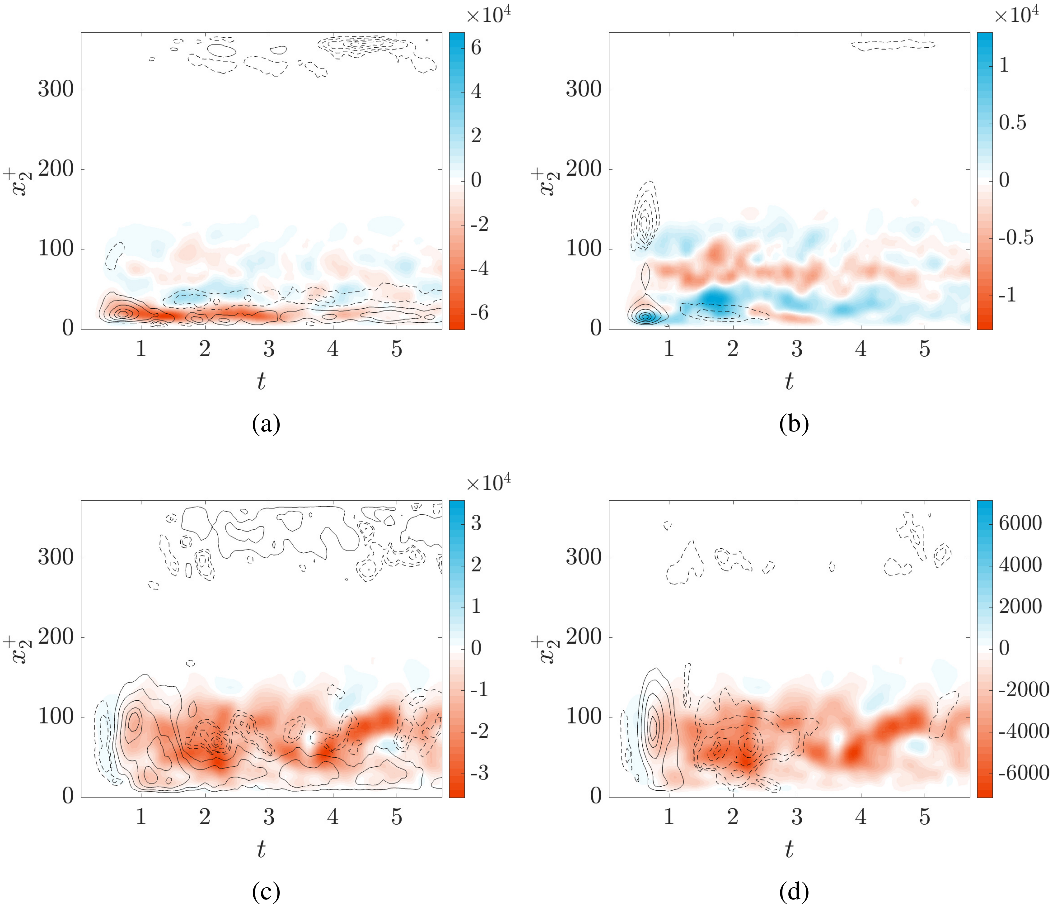

Figure 5.18: Quasi-linear approximation $\widetilde{M}^{(0,1)}$ for the nonlinear energy transfer from the $(0,1)$–mode, normalized by the forcing magnitude $|\kappa|^2$. Figures (a) and (b) correspond to the transfer to the $(0,2)$–mode, and figures (c) and (d) correspond to the transfer to the $(1,1)$–mode. The cases plotted are for (a, c) $\gamma = 2\%$ and (b, d) $\gamma = 10\%$. The black lines represent contours of $\hat{M}^{(0,1)}$ and correspond to 10%, 25%, 50%, 75%, and 90% of the minimum (most negative) value (–), or 10%, 25%, 50%, 75%, and 90% of the maximum (most positive) value (−−).

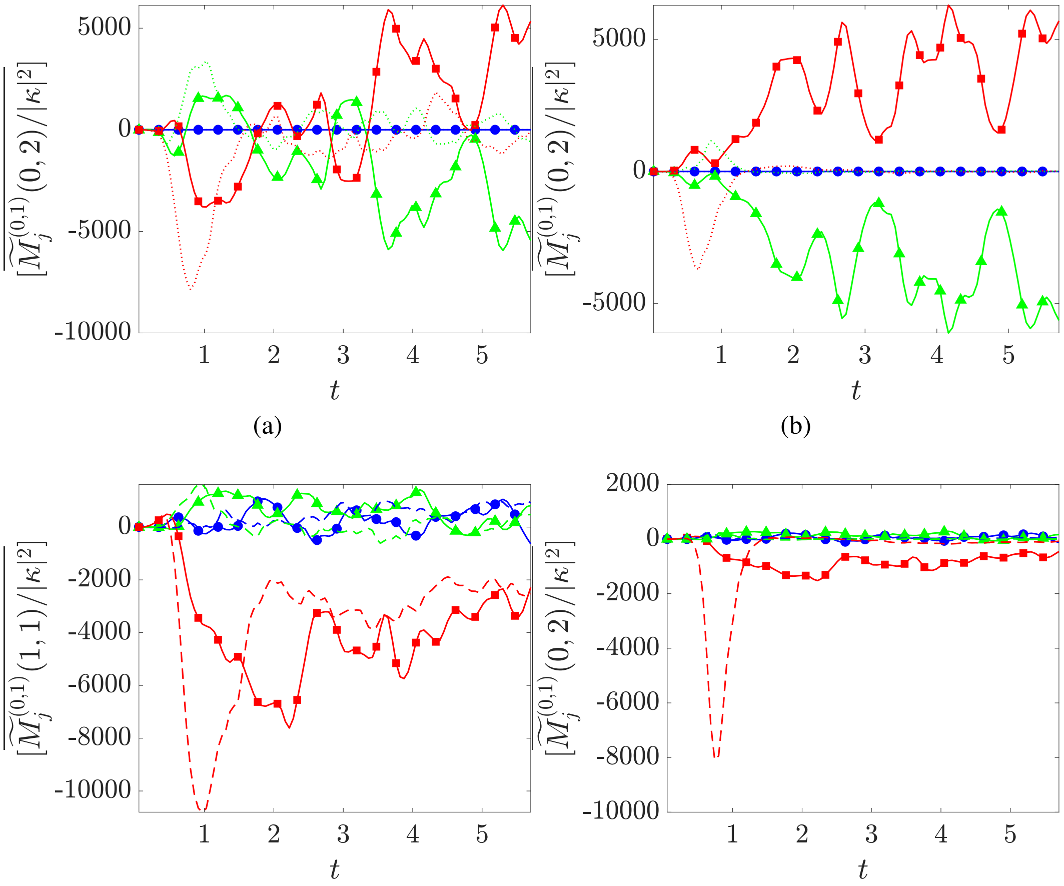

(a) (b)

(c) (d)

Figure 5.19: Nonlinear energy transfer from the $(0,1)$–mode to the (a, b) $(0,2)$–mode and the (c, d) $(1,1)$–mode, broken down by streamwise (blue $-\bullet$), wall-normal (green $-\blacktriangle$) and spanwise (red $-\blacksquare$) contributions, and normalized by forcing magnitude. The solid lines correspond to the nonlinear energy transfer in the quasi-linear model $\overline{[\widetilde{M}^{(0,1)}/|\kappa|^2]}$, while the dashed or dotted lines correspond to $\overline{[\hat{M}^{(0,1)}/|\kappa|^2]}$, the results from DNS (also shown in Figure 5.16). The cases plotted are (a, c) $\gamma = 2\%$ and (b, d) $\gamma = 10\%$.

nonlinear interactions between the target $(0,1)$–mode and the background turbulence can qualitatively explain the streak break-up. For better quantitative accuracy, we suspect that transient growth effects are also important in the outer region.

In addition to studying the interaction of the transiently growing $(0,1)$–mode with the background turbulence, we consider the linear optimal growth of the $(0,2)$– and $(1,1)$–modes. We repeat the windowed wavelet-based resolvent analysis described in Chapter 5.1 but with spatial parameters $(k_1L_1/(2\pi), k_3L_3/(2\pi)) = (0,2)$ and $(k_1L_1/(2\pi), k_3L_3/(2\pi)) = (1,1)$. We use the same spatial grid and choose $T = 44$ to allow the modes ample time to decay to zero, which occurs at $t \approx 20$. The size of the temporal grid is chosen to be $N_t = 880$. Despite the fact that resolvent analysis captures a purely linear process, the x_2–location preferred by the principal resolvent response for $(k_1L_1/(2\pi), k_3L_3/(2\pi)) = (0,2)$ and $(k_1L_1/(2\pi), k_3L_3/(2\pi)) = (1,1)$ coincide with the foci of nonlinear interaction between the $(0,1)$–mode, and the $(0,2)$– and $(1,1)$–modes, respectively (Figure 5.20). The resolvent modes, which capture the maximal linear growth of the two scales considered, accurately predicts the locations of energy exchange with the actuated mode, and thus, transient growth via linear mechanisms can dictate the spatial structure of the nonlinear energy cascade. Moreover, we observe that the principal resolvent response mode for $(k_1L_1/(2\pi), k_3L_3/(2\pi)) = (0,2)$ grows faster than the mode for $(k_1L_1/(2\pi), k_3L_3/(2\pi)) = (1,1)$, peaking earlier, which may explain the earlier peaks of $\hat{M}^{(0,1)}(0,2)$ compared to $\hat{M}^{(0,1)}(1,1)$ (Figure 5.12).

The results in Figure 5.20 support works like Huang et al. (2023), which studies the efficacy of individual dyadic interactions at exciting an energetic scale in the channel. The influence of individual dyadic contributions to the nonlinear term of the Navier-Stokes equations is measured via the projection of the contributions onto the principal resolvent forcing mode for the scale of interest, and dyadic interactions highly aligned with the forcing mode are deemed important contributors to turbulence. The underpinning assumption is that the response mode corresponding to the forcing mode indeed capture the behavior of turbulence in the channel, which Figure 5.20 suggests is true, even for secondary scales like the $(0,2)$– and $(1,1)$–modes. Figure 5.20 also helps explain the success of restricted nonlinear (RNL) models at replicating turbulent statistics (Farrell et al., 2017; Gayme & Minnick, 2019; Thomas et al., 2014). In RNL models, the mean profile is governed by a modified version of the fully nonlinear Navier-Stokes equations where only a reduced subset of fluctuation scales contribute to the nonlinear advection terms, while

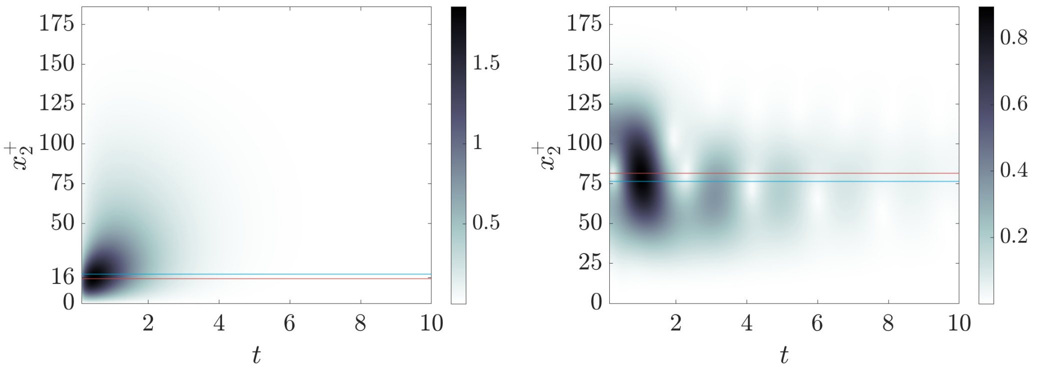

(a) (b)

Figure 5.20: Magnitude of the streamwise component of the principal resolvent response modes for (a) $(n_1, n_3) = (0, 2)$ and (b) $(n_1, n_3) = (1, 1)$. The modes are normalized so that their action pseudo-norm is 1. The horizontal lines represent the peak location of (a) $\hat{M}^{(0,1)}(0, 2)$ and (b) $\hat{M}^{(0,1)}(1, 1)$ for $\gamma = 2\%$ (blue) and $\gamma = 10\%$ (red).

the fluctuations obey the linearized Navier-Stokes equations about the mean profile. The location of the modes in Figure 5.20 indeed suggest that linear mechanisms are enough to at least predict the correct spatial distribution of the nonlinear energy transfer to the two most important secondary modes involved in the energy cascade in this experiment.

The results presented in this chapter thus show that two secondary modes play a dominant role in draining the streak of its energy and curtailing its growth. The first mode, constant in the streamwise direction and twice periodic in the spanwise direction, corresponds to a splitting of the streak into two branches and accounts for the first region of energy transfer near the wall. The second, once periodic in the streamwise and spanwise directions, corresponds to a streamwise break-up of the streak and accounts for the second region of energy transfer farther from the wall. The branching mode receives energy from the actuated mode via the self-interaction of the injected streak, which explains the sensitivity of the energy transfer time scale in the near-wall region to forcing amplitude.

The streak interacts with these secondary modes mostly through an NLT_3 type energy transfer, *i.e.* via the spanwise nonlinear self-advection term. Our crude quasi-linear model generally predicts the dominance of the NLT_3 mechanism for the streak breakup in the outer region, but fails to predict the trend for the streak splitting near the wall. To predict the streak breakdown mechanism in the near-wall region and the buffer layer with better accuracy, we must take into account transient growth phenomena. Finally, the transient principal resolvent response modes for the two scales corresponding to streak break-up and splitting predict the locations of the nonlinear energy exchange between these scales and the actuated scale. This further proves that resolvent modes can be informative of turbulent flows.

Testing the effectiveness of the principal resolvent forcing mode reveals valuable insights on the stability of the streak, the mechanism by which it sheds energy, and the sensitivity of this nonlinear energy transfer mechanism to forcing amplitude. To find structures more effective than the resolvent forcing mode at actuating the minimal flow unit, one could use nonlinear optimization techniques (Heide & Hemati, 2023; Kerswell, 2018). These broadly aim to maximize the growth of kinetic energy within a user-defined time window, and enforce the satisfaction of the (nonlinear) Navier-Stokes equations as an optimization constraint. Nevertheless, an important advantage of wavelet-based resolvent analysis is its computational efficiency and tractability.

Chapter 6

CONCLUSION

6.1 Summary and discussion

In order to expand the linear analysis toolbox that is available to turbulence researchers, we develop a wavelet-based formulation of resolvent analysis. Traditional resolvent analysis formulations rely on a Fourier transformation in time of the linearized Navier-Stokes equations, and are thus only applicable to stationary flows, or flows with periodic mean profiles. Moreover, the optimal modes that the traditional method produces—constructed from Fourier modes in time—cannot practically encode transient, non-periodic trajectories. The wavelet-based formulation addresses these issues and enables resolvent analysis to be applied to the analysis of non-stationary flows, as well as transient linear phenomena within turbulent flows. The wavelet-based modes are functions of the wavelet time shift and scale parameters, which capture information at a particular time interval and frequency band.

In Chapter 3, we show that the wavelet-based resolvent operator is equivalent to the Fourier-based operator for statistically stationary flows and flows with periodic mean statistics, provided we use an orthonormal wavelet transform; the wavelet-based formulation thus represents a generalization of resolvent analysis. We show this by validating the method against traditional resolvent analysis applied to turbulent channel flow, and against harmonic resolvent analysis applied to the turbulent Stokes boundary layer. The formulation of resolvent analysis in a wavelet basis further opens the door to a new type of analysis. With the help of windowing matrices that can restrict the forcing or the response to a chosen shift or scale, we can compute time- and frequency-localized optimal forcing and response modes. In this work, we make use of this windowing approach to compute linearly optimal pulse-like forcing modes and their corresponding transient response.

We apply this newly developed formulation to two types of problems that have historically made use of traditional resolvent analysis methods: the first is the analysis of the mechanisms that sustain wall-bounded turbulence (Chapter 4), and the second is the control of turbulent flows (Chapter 5). For the first application, we capture energetic bursting phenomena in channel flow using our wavelet-based resolvent modes (Chapter 4.1). By post-multiplying the wavelet-based resolvent operator with a windowing matrix, we constrain the forcing to wavelet pulse and compute the optimally perturbing time-localized forcing mode and its corresponding (unconstrained) response, which transiently grows and decays. The principal response represents a maximally amplified burst that is driven by linear mechanisms; it is found to grow and decay in similar time scales as energetic intermittent bursts in the turbulent channel. The resolvent modes reveal that this optimal burst exploits the Orr mechanism, which supports arguments that this mechanism plays an important role in sustaining near-wall turbulence. Indeed, the wall-normal velocity component of the mode grows in amplitude as the velocity structures tilt forward; the streamwise and spanwise component are in turn amplified via the lift-up mechanism before decaying slowly.

Another turbulent flow that we analyze with the wavelet-based resolvent operator is turbulent channel flow subjected to a sudden and sustained spanwise pressure gradient (Chapter 4.2). The mean profile of this flow varies in time, gradually adapting to the new pressure conditions by rotating in the spanwise direction. The resolvent modes for this system reflect the increasing shear velocity and rotating wall shear stress. By appropriately scaling the resolvent modes according to the flow conditions at different times, we find that the resulting resolvent response modes peak at those times, capturing near-wall streaks oriented in the direction of the wall shear stress. Indeed, the predominant velocity component for the resolvent modes progressively shifts from the streamwise component to the spanwise one, mirroring the reorientation of the mean flow. Once the the modes identify the dominant coherent structures, they shed light on the flow conditions that amplify them or, conversely, suppress them. The wavelet-based modes point to a damping of the lift-up mechanism, which normally helps energize streamwise near-wall streaks. Further linear analysis attributes the weakened lift-up to an instantaneous misalignment of the mean shear and velocity profiles during the transient phase of the flow. This constitutes a new explanation to the depletion of tangential Reynolds stresses, *i.e.* the wall-normal transport of streamwise momentum, observed in DNS.

The cases considered showcase the versatility of the wavelet-based formulation in analyzing transient linear energy amplification in flows with both statistically stationary and non-stationary mean profiles. Another application of resolvent analysis is the control, emulation and estimation of turbulent flows. In Chapter 5, we probe the ability of resolvent modes to accurately represent the response of a turbulent system—the minimal flow unit—to actuation by a principal resolvent forcing mode.

We compute a time-localized forcing mode, which appears in the form of streamwise rolls, an inject it at different intensities into a simulation of the minimal flow unit. The wavelet-based formulation allows us to compare the instantaneous discrepancies between the minimal flow unit's response and the optimal linear response, which appears as transiently growing streamwise streaks. Across all forcing amplitudes, the initial growth phase is similar and the systems peak at roughly the same time, but, the higher the forcing amplitude, the faster the decay of the system back to the unforced turbulent system. These results are presented in Chapter 5.3. We observe that the forced DNS flow fields are closer to the resolvent response mode in the near-wall region, where viscous effects are more prominent. The nonlinearities of turbulence interrupt the initial energy growth driven by the linear dynamics of the flow; this is seen in all cases forced by the principal resolvent mode. Nevertheless, when comparing the resulting flow to one forced by the first suboptimal forcing mode and another forced by a spatially-random forcing, we find the principal resolvent forcing still produces a larger transient energy growth than the suboptimal mode, though the energy amplification is notably lower in both cases compared to the linearized case. Both systems were significantly more amplified than the random forcing case.

In an attempt to understand what drives the deviation of the turbulent minimal flow unit from the optimal linear trajectory, we compute the nonlinear energy transfer from the actuated mode to secondary scales (Chapter 5.4). Two secondary modes are found to play a dominant role in draining the streak of its energy and curtailing its growth. The first mode, constant in the streamwise direction and twice periodic in the spanwise direction, corresponds to a splitting of the streak into two branches and dominates the energy transfer in the near-wall region, including the buffer layer. The second, once periodic in the streamwise and spanwise directions, corresponds to a streamwise break-up of the streak and dominates the energy transfer in the outer region. We note that a larger forcing amplitude accelerates the energy transfer from the actuated mode to smaller scales across all wall-normal heights, but this effect is more pronounced near the wall than in the outer region. This can be explained by the fact that the branching mode receives energy from the self-interaction of the injected streak, making it more sensitive to the forcing amplitude. Both streak breakdown mechanisms in the near-wall and outer regions are due to what we dub NLT_3 type energy transfers, which are facilitated by the spanwise nonlinear self-advection term. This result echoes evidence in other works, which argue that push-over is a key mechanism that lies at the heart of the amplification of small scales.

We attempt to model the predicted nonlinear energy transfer from the actuated mode by computing the interaction of the injected streak with the background turbulence at the initial condition. We find that these one-way interactions, without the nonlinear feedback at later times, generally predict the trends for the streak breakup that dominates in the outer region. The crude model cannot, however, predict the dominance of the NLT_3 contribution that occurs during the streak splitting near the wall. We postulate that in the near-wall region and the buffer layer, transient growth phenomena are necessary to explain the behavior of the branching mode. Finally, we find that the transient resolvent response modes computed for the break-up and branching modes predict the wall-normal location of the nonlinear energy transfer to these modes in the DNS. The modes peak exactly at the hubs of nonlinear energy exchange with the actuated scale. The initial linearly driven transient growth, though it may be suppressed at later times, is prominent enough to influence the structure of channel flow turbulence. This further proves that resolvent modes can be informative of turbulent flows despite using the linearized equations of motion.

6.2 Outlook

This work paves the way to a range of new projects that center the analysis of turbulent flows. We split these into two groups: those that refine and deepen the analysis of the systems already considered in the above chapters, and those that broaden the application of resolvent analysis to new systems.

The bursts obtained in Chapter 4.1 exhibit promising similarities with intermittent turbulent statistics measured from simulations. We can directly measure the presence of these linearly optimal resolvent bursts in simulated systems by projecting DNS data onto them. The projection signal can then be correlated turbulent kinetic energy in the buffer layer, for example, in an attempt to determine the relevance of these linearly determined Orr bursts in the production and regeneration of streaks.

Additionally, we can explore methods that do not rely the user's arbitrary choice of mother wavelet. Floryan and Graham (2021) and Guo et al. (2023) propose a data-driven wavelet decomposition algorithm that extracts a set of hierarchical structures "inherent" to simulation data. Practically, the algorithm minimizes the projection error of the DNS flow field onto a set of shifted functions. The process is then repeated with the subsampled residual in order to capture the next scale of data-driven wavelets. These data-driven wavelets can be used to transform the equations of motion instead of a traditional analytical wavelet transform. It would be interesting to study how these data-driven wavelets change the shape and behavior of the optimal Orr bursts, and whether they improve the correlations between these bursts and near-wall turbulence.

The Stokes turbulent boundary layer is also fertile ground for the application of the wavelet-based methods. The cyclical statistics of this flow can exhibit periods of intense turbulence interspersed with periods of re-laminarization. We can apply the windowing approach described in Chapter 3.2 to isolate these different mechanisms and study their dynamics by considering the structure of the principal forcing and response modes.

Finally, we can apply wavelet-based resolvent analysis to new classes of turbulent flows, like those that are only homogeneous in one spatial direction. This significantly raises the computational and storage costs of the method, but the strategies explored in Chapter 3 can help mitigate these. Examples of two-dimensional non-stationary flows include turbulent flows subjected to unsteady pressure gradients. This type of flow is studied experimentally in Parthasarathy and Saxton-Fox (2022), where the unsteady pressure gradients are imposed in a channel using a flexing top wall. Another application of the 2-D method is inspired by Markeviciute and Kerswell (2024): it would be interesting to linearize the equations of motion about a base flow constructed from the sum of the mean channel flow profile and the transient streak-like principal response computed in Chapter 5. We would then test whether wavelet-based resolvent analysis applied to this system can predict the privileged role played by the splitting and break-up modes. Whether wavelet-based resolvent analysis is used for the re-analysis of canonical systems, or the study of new systems, we hope that its flexibility can help unlock new insights on the behavior of turbulence.

BIBLIOGRAPHY

Abreu, L. I., Cavalieri, A. V. G., Schlatter, P., Vinuesa, R., & Henningson, D. S. (2020). Spectral proper orthogonal decomposition and resolvent analysis of near-wall coherent structures in turbulent pipe flows. *J. Fluid Mech.*, *900*, A11.

Adrian, R. J. (2007). Hairpin vortex organization in wall turbulence. *Phys. Fluids*, *19*(4), 041301.

Ahmed, M. A., Bae, H. J., Thompson, A. F., & McKeon, B. J. (2021). Resolvent analysis of stratification effects on wall-bounded shear flows. *Phys. Rev. Fluids*, *6*, 084804.

Akhavan, R., Kamm, R. D., & Shapiro, A. H. (1991). An investigation of transition to turbulence in bounded oscillatory Stokes flows Part 1. Experiments. *J. Fluid Mech.*, *225*, 395–422.

Arun, R., Bae, H. J., & McKeon, B. J. (2023). Towards real-time reconstruction of velocity fluctuations in turbulent channel flow. *Phys. Rev. Fluids*, *8*(6), 064612.

Bae, H. J., Dawson, S. T. M., & McKeon, B. J. (2020a). Resolvent-based study of compressibility effects on supersonic turbulent boundary layers. *J. Fluid Mech.*, *883*, A29.

Bae, H. J., Dawson, S. T. M., & McKeon, B. J. (2020b). Studying the effect of wall cooling in supersonic boundary layer flow using resolvent analysis. *AIAA Scitech 2020 Forum*, 0575.

Bae, H. J., & Lee, M. (2021). Life cycle of streaks in the buffer layer of wall-bounded turbulence. *Phys. Rev. Fluids*, *6*(6), 064603.

Bae, H. J., Lozano-Durán, A., Bose, S. T., & Moin, P. (2018). Turbulence intensities in large-eddy simulation of wall-bounded flows. *Phys. Rev. Fluids*, *3*(1), 014610.

Bae, H. J., Lozano-Durán, A., Bose, S. T., & Moin, P. (2019). Dynamic slip wall model for large-eddy simulation. *J. Fluid Mech.*, *859*, 400–432.

Bae, H. J., Lozano-Durán, A., & McKeon, B. J. (2021). Nonlinear mechanism of the self-sustaining process in the buffer and logarithmic layer of wall-bounded flows. *J. Fluid Mech.*, *914*, A3.

Bakewell, H. P. J., & Lumley, J. L. (1967). Viscous sublayer and adjacent wall region in turbulent pipe flow. *Phys. Fluids*, *10*(9), 1880–1889.

Ballouz, E., Dawson, S. T. M., & Bae, H. J. (2024). Transient growth of wavelet-based resolvent modes in the buffer layer of wall-bounded turbulence. *J. Phys.: Conference Series*, *2753*(1), 012002. https://doi.org/10.1088/1742-6596/2753/1/012002

Ballouz, E., Dawson, S. T. M., & Bae, H. J. (2025). Transient growth and nonlinear breakdown of wavelet-based resolvent modes in turbulent channel flow [Submitted]. *arXiv preprint arXiv:2502.08670*. https://doi.org/10.48550/arXiv.2502.08670

Ballouz, E., Lopez-Doriga, B., Dawson, S. T. M., & Bae, H. J. (2024). Wavelet-based resolvent analysis of non-stationary flows. *J. Fluid Mech.*, *999*, A53. https://doi.org/10.1017/jfm.2024.903

Ballouz, E., Lopez-Dóriga, B., Dawson, S. T. M., & Bae, H. J. (2023). Wavelet-based resolvent analysis for statistically-stationary and temporally-evolving flows. *AIAA SCITECH 2023 Forum*, 0676. https://doi.org/10.2514/6.2023-0676

Beneddine, S., Yegavian, R., Sipp, D., & Leclaire, B. (2017). Unsteady flow dynamics reconstruction from mean flow and point sensors: An experimental study. *J. Fluid Mech.*, *824*, 174–201.

Berkooz, G., Holmes, P., & Lumley, J. L. (1993). The proper orthogonal decomposition in the analysis of turbulent flows. *Annu. Rev. Fluid Mech.*, *25*(1), 539–575.

Blackwelder, R. F., & Eckelmann, H. (1979). Streamwise vortices associated with the bursting phenomenon. *J. Fluid Mech.*, *94*(3), 577–594.

Blondeaux, P., & Vittori, G. (1994). Wall imperfections as a triggering mechanism for Stokes-layer transition. *J. Fluid Mech.*, *264*, 107–135.

Böberg, L., & Brösa, U. (1988). Onset of turbulence in a pipe. *Z. Naturforsch.*, *43*(8-9), 697–726.

Borée, J. (2003). Extended proper orthogonal decomposition: A tool to analyse correlated events in turbulent flows. *Exp. Fluids*, *35*(2), 188–192.

Butler, K. M., & Farrell, B. F. (1992). Three-dimensional optimal perturbations in viscous shear flow. *Phys. Fluids A.*, *4*(8), 1637–1650.

Butler, K. M., & Farrell, B. F. (1993). Optimal perturbations and streak spacing in wall-bounded turbulent shear flow. *Phys. Fluids A*, *5*(3), 774–777.

Carstensen, S., Sumer, B. M., & Fredsøe, J. (2010). Coherent structures in wave boundary layers. Part 1. Oscillatory motion. *J. Fluid Mech.*, *646*, 169–206.

Cess, R. D. (1958). A survey of the literature on heat transfer in turbulent tube flow. *Res. Rep*, *8*.

Chernyshenko, S. I., & Baig, M. F. (2005). The mechanism of streak formation in near-wall turbulence. *J. Fluid Mech.*, *544*, 99–131.

Costamagna, P., Vittori, G., & Blondeaux, P. (2003). Coherent structures in oscillatory boundary layers. *J. Fluid Mech.*, *474*, 1–33.

Cui, G., & Jacobi, I. (2023). Prediction of the phase difference between large-scale velocity and reynolds stress fluctuations in wall turbulence. *J. Fluid Mech.*, *969*, A13.

Del Alamo, J. C., & Jiménez, J. (2006). Linear energy amplification in turbulent channels. *J. Fluid Mech.*, *559*, 205–213.

Ding, J., Chung, D., & Illingworth, S. J. (2025). Mode-to-mode nonlinear energy transfer in turbulent channel flows. *Journal of Fluid Mechanics*, *1002*, A42.

Drineas, P., & Mahoney, M. W. (2016). RandNLA: Randomized numerical linear algebra. *Commun. ACM*, *59*(6), 80–90.

Elnahhas, A., Lenz, E., Moin, P., Lozano-Durán, A., & Bae, H. J. (2024). Are the dynamics of wall turbulence in minimal channels and larger domain channels equivalent? A graph-theoretic approach. *J. Phys.: Conference Series*, *2753*(1), 012004.

Encinar, M. P., & Jiménez, J. (2020). Momentum transfer by linearised eddies in turbulent channel flows. *J. Fluid Mech.*, *895*, A23.

Farrell, B. F., Gayme, D. F., & Ioannou, P. J. (2017). A statistical state dynamics approach to wall turbulence. *Phil. Trans. R. Soc. A*, *375*(2089), 20160081.

Fjørtoft, R. (1950). Application of integral theorems in deriving criteria for instability for laminar flows and for the baroclinic circular vortex. *Geofys. Publ.*, *17*(6), 1–52.

Flores, O., & Jiménez, J. (2010). Hierarchy of minimal flow units in the logarithmic layer. *Phys. Fluids*, *22*(7).

Floryan, D., & Graham, M. D. (2021). Discovering multiscale and self-similar structure with data-driven wavelets. *Proc. Natl. Acad. Sci. USA*, *118*(1), e2021299118.

Gayme, D. F., & Minnick, B. A. (2019). Coherent structure-based approach to modeling wall turbulence. *Phys. Rev. Fluids*, *4*(11), 110505.

Gomez, S. R., Williams, C., Di Renzo, M., Schmid, P., & McKeon, B. J. (2022). Adaptive resolvent analysis with application to high enthalpy flows. *Proceedings of the CTR Summer Program*, 87–96.

Gómez, F., Blackburn, H. M., Rudman, F., Sharma, A. S., & McKeon, B. J. (2016). A reduced-order model of three-dimensional unsteady flow in a cavity based on the resolvent operator. *J. Fluid Mech.*, *798*, R2.

Guo, A., Floryan, D., & Graham, M. D. (2023). Self-similar, spatially localized structures in turbulent pipe flow from a data-driven wavelet decomposition. *J. Fluid Mech.*, *971*, A9.

Halko, N., Martinsson, P.-G., & Tropp, J. A. (2011). Finding structure with randomness: Probabilistic algorithms for constructing approximate matrix decompositions. *SIAM Rev.*, *53*(2), 217–288.

Hamilton, J. M., Kim, J., & Waleffe, F. (1995). Regeneration mechanisms of near-wall turbulence structures. *J. Fluid Mech.*, *287*, 317–348.

Heide, A. L., & Hemati, M. S. (2023). An optimization framework for analyzing nonlinear stability due to sparse finite-amplitude perturbations. *arXiv e-prints*, arXiv–2311.

Hino, M., Sawamoto, M., & Takasu, S. (1976). Experiments on transition to turbulence in an oscillatory pipe flow. *J. Fluid Mech.*, *75*(2), 193–207.

Hoyas, S., & Jiménez, J. (2006). Scaling of velocity fluctuations in turbulent channels up to $Re_\tau = 2000$. *Phys. Fluids*, *18*, 011702.

Hoyas, S., & Jiménez, J. (2008). Reynolds number effects on the Reynolds-stress budgets in turbulent channels. *Phys. Fluids*, *20*(10), 101511.

Huang, Y., Toedtli, S. S., Chini, G. P., & McKeon, B. J. (2023). Spatio-temporal characterization of non-linear forcing in turbulence. *arXiv preprint arXiv:2305.00095*.

Hwang, Y., & Bengana, Y. (2016). Self-sustaining process of minimal attached eddies in turbulent channel flow. *J. Fluid Mech.*, *795*, 708–738.

Hwang, Y., & Cossu, C. (2010). Self-sustained process at large scales in turbulent channel flow. *Phys. Rev. Lett.*, *105*(4), 044505.

Illingworth, S. J., Monty, J. P., & Marusic, I. (2018). Estimating large-scale structures in wall turbulence using linear models. *J. Fluid Mech.*, *842*, 146–162.

Jensen, B. L., Sumer, B. M., & Fredsøe, J. (1989). Turbulent oscillatory boundary layers at high Reynolds numbers. *J. Fluid Mech.*, *206*, 265–297.

Jeun, J., Nichols, J. W., & Jovanović, M. R. (2016). Input-output analysis of high-speed axisymmetric isothermal jet noise. *Phys. Fluids*, *28.4*, 047101.

Jiménez, J. (2013). How linear is wall-bounded turbulence? *Phys. Fluids*, *25*, 110814.

Jiménez, J. (2015). Direct detection of linearized bursts in turbulence. *Phys. Fluids*, *27*(6), 065102.

Jiménez, J. (2018). Coherent structures in wall-bounded turbulence. *J. Fluid Mech.*, *842*, P1.

Jiménez, J., & Moin, P. (1991). The minimal flow unit in near-wall turbulence. *J. Fluid Mech.*, *225*, 213–240.

Jiménez, J., & Pinelli, A. (1999). The autonomous cycle of near-wall turbulence. *J. Fluid Mech.*, *389*, 335–359.

Johansson, A. V., Her, J.-Y., & Haritonidis, J. H. (1987). On the generation of high-amplitude wall-pressure peaks in turbulent boundary layers and spots. *J. Fluid Mech.*, *175*, 119–142.

Jovanovic, M. R. (2004). *Modeling, analysis, and control of spatially distributed systems*. University of California at Santa Barbara, Dept. of Mechanical Engineering.

Jovanović, M. R., & Bamieh, B. (2005). Componentwise energy amplification in channel flows. *J. Fluid Mech.*, *534*, 145–183.

Kerswell, R. R. (2018). Nonlinear nonmodal stability theory. *Ann. Rev. Fluid Mech.*, *50*(1), 319–345.

Kim, H. T., Kline, S. J., & Reynolds, W. C. (1971). The production of turbulence near a smooth wall in a turbulent boundary layer. *J. Fluid Mech.*, *50*(1), 133–160.

Kim, J., & Moin, P. (1985). Application of a fractional-step method to incompressible Navier-Stokes equations. *J. Comput. Phys.*, *59*(2), 308–323.

Klebanoff, P. S., Tidstrom, K. D., & Sargent, L. M. (1962). The three-dimensional nature of boundary-layer instability. *J. Fluid Mech.*, *12*(1), 1–34.

Kline, S. J., Reynolds, W. C., Schraub, F. A., & Runstadler, P. W. (1967). The structure of turbulent boundary layers. *J. Fluid Mech.*, *30*(4), 741–773.

Kojima, Y., Yeh, C., Taira, K., & Kameda, M. (2020). Resolvent analysis on the origin of two-dimensional transonic buffet. *J. Fluid Mech.*, *885*, R1.

Landahl, M. T. (1975). Wave breakdown and turbulence. *SIAM J. Appl. Math*, *28*(4), 735–756.

Landahl, M. T. (1980). A note on an algebraic instability of inviscid parallel shear flows. *J. Fluid Mech.*, *98*(2), 243–251.

Lin, C.-T., Tsai, M.-L., & Tsai, H.-C. (2023). Flow control of a plunging cylinder based on resolvent analysis. *J. of Fluid Mech.*, *967*, A41.

Liu, Q., Sun, Y., Yeh, C.-A., Ukeiley, L. S., Cattafesta III, L. N., & Taira, K. (2021). Unsteady control of supersonic turbulent cavity flow based on resolvent analysis. *J. Fluid Mech.*, *925*, A5.

Lozano-Durán, A., & Arranz, G. (2022). Information-theoretic formulation of dynamical systems: Causality, modeling, and control. *Phys. Rev. Res.*, *4*(2), 023195.

Lozano-Durán, A., & Bae, H. J. (2016). Turbulent channel with slip boundaries as a benchmark for subgrid-scale models in les. *Annual Research Briefs. Center for Turbulence Research*, *2016*, 97–103.

Lozano-Durán, A., & Bae, H. J. (2019). Characteristic scales of Townsend's wall-attached eddies. *J. Fluid Mech.*, *868*, 698.

Lozano-Durán, A., Constantinou, N. C., Nikolaidis, M.-A., & Karp, M. (2021). Cause-and-effect of linear mechanisms sustaining wall turbulence. *J. Fluid Mech.*, *914*, A8.

Lozano-Durán, A., Giometto, M. G., Park, G. I., & Moin, P. (2020). Non-equilibrium three-dimensional boundary layers at moderate Reynolds numbers. *J. Fluid Mech.*, *883*, A20.

Lozano-Durán, A., Hack, M. J. P., & Moin, P. (2018). Modeling boundary-layer transition in direct and large-eddy simulations using parabolized stability equations. *Phys. Rev. Fluids*, *3*, 023901.

Luhar, M., Sharma, A. S., & McKeon, B. J. (2014). Opposition control within the resolvent analysis framework. *J. Fluid Mech.*, *749*, 597–626.

Lumley, J. L. (1967). The structure of inhomogeneous turbulent flows. *Atmospheric turbulence and radio wave propagation*, 166–178.

Lumley, J. L. (2007). *Stochastic tools in turbulence*. Courier Corporation.

Malkus, W. V. R. (1956). Outline of a theory of turbulent shear flow. *J. Fluid Mech.*, *1*(5), 521–539.

Mallat, S. (1999). *A wavelet tour of signal processing*. Elsevier.

Markeviciute, V. K., & Kerswell, R. R. (2024). Threshold transient growth as a criterion for turbulent mean profiles. *J. Fluid Mech.*, *996*, A32.

Martini, E., Cavalieri, A. V. G., Jordan, P., Towne, A., & Lesshafft, L. (2020). Resolvent-based optimal estimation of transitional and turbulent flows. *J. Fluid Mech.*, *900*, A2.

McKeon, B. J. (2017). The engine behind (wall) turbulence: Perspectives on scale interactions. *J. Fluid Mech.*, *817*, P1.

McKeon, B. J. (2019). Self-similar hierarchies and attached eddies. *Phys. Rev. Fluids*, *4*(8), 082601.

McKeon, B. J., & Sharma, A. S. (2010). A critical-layer framework for turbulent pipe flow. *J. Fluid Mech.*, *658*, 336–382.

McKeon, B. J., Sharma, A. S., & Jacobi, I. (2013). Experimental manipulation of wall turbulence: A systems approach. *Phys. Fluids*, *25*(3).

Mezić, I. (2013). Analysis of fluid flows via spectral properties of the Koopman operator. *Annu. Rev. Fluid Mech.*, *45*, 357–378.

Moarref, R., Sharma, A. S., Tropp, J. A., & McKeon, B. J. (2013). Model-based scaling of the streamwise energy density in high-Reynolds-number turbulent channels. *J. Fluid Mech.*, *734*, 275–316.

Moin, P., Shih, T.-H., Driver, D. M., & Mansour, N. N. (1990). Direct numerical simulation of a three-dimensional turbulent boundary layer. *Phys. Fluids*, *2*(10), 1846–1853.

Musco, C., & Musco, C. (2015). Randomized block krylov methods for stronger and faster approximate singular value decomposition. *Adv. Neural Inf. Process Syst.*, *28*, 1396–1404.

Najmi, A.-H. (2012). *Wavelets: A concise guide*. JHU Press.

Orlandi, P. (2000). *Fluid flow phenomena: A numerical toolkit* (Vol. 55). Springer Science & Business Media.

Orr, W. M. (1907). The stability or instability of the steady motions of a perfect liquid and of a viscous liquid. Part I: A perfect liquid. *Proc. R. Ir. Acad.*, *A 27*, 9–68.

Ozdemir, C. E., Hsu, T.-J., & Balachandar, S. (2014). Direct numerical simulations of transition and turbulence in smooth-walled Stokes boundary layer. *Phys. Fluids*, *26*(4), 045108.

Padovan, A., Otto, S. E., & Rowley, C. W. (2020). Analysis of amplification mechanisms and cross-frequency interactions in nonlinear flows via the harmonic resolvent. *J. Fluid Mech.*, *900*, A14.

Padovan, A., & Rowley, C. W. (2022). Analysis of the dynamics of subharmonic flow structures via the harmonic resolvent: Application to vortex pairing in an axisymmetric jet. *Phys. Rev. Fluids*, *7*(7), 073903.

Panton, R. L. (2001). Overview of the self-sustaining mechanisms of wall turbulence. *Prog. Aerosp. Sci.*, *37*(4), 341–383.

Parthasarathy, A., & Saxton-Fox, T. (2022). A novel experimental facility to impose unsteady pressure gradients on turbulent boundary layers. *Exp. Fluids*, *63*(6), 107.

Picard, C., & Delville, J. (2000). Pressure velocity coupling in a subsonic round jet. *Int. J. Heat Fluid Fl.*, *21*(3), 359–364.

Pickering, E., Rigas, G., Nogueira, P. A. S., Cavalieri, A. V. G., Schmidt, O. T., & Colonius, T. (2020). Lift-up, Kelvin–Helmholtz and Orr mechanisms in turbulent jets. *J. Fluid Mech.*, *896*, A2.

Pujals, G., García-Villalba, M., Cossu, C., & Depardon, S. (2009). A note on optimal transient growth in turbulent channel flows. *Phys. Fluids*, *21*(1), 015109.

Reynolds, W. C., & Tiederman, W. G. (1967). Stability of turbulent channel flow, with application to Malkus's theory. *J. Fluid Mech.*, *27*(2), 253–272.

Ribeiro, J. H. M., Yeh, C.-A., & Taira, K. (2020). Randomized resolvent analysis. *Phys. Rev. Fluids*, *5*(3), 033902.

Robinson, S. K. (1991). Coherent motions in the turbulent boundary layer. *Annu. Rev. Fluid Mech.*, *23*(1), 601–639.

Sarpkaya, T. (1993). Coherent structures in oscillatory boundary layers. *J. Fluid Mech.*, *253*, 105–140.

Schmid, P. J., Henningson, D. S., & Jankowski, D. F. (2002). Stability and transition in shear flows. applied mathematical sciences, vol. 142. *Appl. Mech. Rev.*, *55*(3), B57–B59.

Schmidt, O. T., Towne, A., Rigas, G., Colonius, T., & Brès, G. A. (2018). Spectral analysis of jet turbulence. *J. Fluid Mech.*, *855*, 953–982.

Schoppa, W., & Hussain, F. (2002). Coherent structure generation in near-wall turbulence. *J. Fluid Mech.*, *453*, 57–108.

Simon, H. D., & Zha, H. (2000). Low-rank matrix approximation using the Lanczos bidiagonalization process with applications. *SIAM J. Sci. Comput.*, *21*(6), 2257–2274.

Smith, C. R., & Metzler, S. P. (1983). The characteristics of low-speed streaks in the near-wall region of a turbulent boundary layer. *J. Fluid Mech.*, *129*, 27–54.

Smits, A. J., McKeon, B. J., & Marusic, I. (2011). High–Reynolds number wall turbulence. *Annu. Rev. Fluid Mech.*, *43*, 353–375.

Spalart, P. R., & Baldwin, B. S. (1989). Direct simulation of a turbulent oscillating boundary layer. In *Turbulent shear flows 6* (pp. 417–440). Springer.

Symon, S., Illingworth, S. J., & Marusic, I. (2021). Energy transfer in turbulent channel flows and implications for resolvent modelling. *J. Fluid Mech.*, *911*, A3.

Symon, S., Madhusudanan, A., Illingworth, S. J., & Marusic, I. (2023). Use of eddy viscosity in resolvent analysis of turbulent channel flow. *Phys. Rev. Fluids*, *8*(6), 064601.

Taira, K., Brunton, S. L., Dawson, S. T. M., Rowley, C. W., Colonius, T., McKeon, B. J., Schmidt, O. T., Gordeyev, S., Theofilis, V., & Ukeiley, L. S. (2017). Modal analysis of fluid flows: An overview. *AIAA J.*, *55*(12), 4013–4041.

Taylor, G. I. (1938). The spectrum of turbulence. *Proc. R. Soc. A.*, *164*(919), 476–490.

Thomas, V. L., Lieu, B. K., Jovanović, M. R., Farrell, B. F., Ioannou, P. J., & Gayme, D. F. (2014). Self-sustaining turbulence in a restricted nonlinear model of plane Couette flow. *Phys. Fluids*, *26*(10).

Tissot, G., Cavalieri, A. V. G., & Mémin, E. (2021). Stochastic linear modes in a turbulent channel flow. *J. Fluid Mech.*, *912*, A51.

Tissot, G., Zhang, M., Lajús, F. C., Cavalieri, A. V. G., & Jordan, P. (2017). Sensitivity of wavepackets in jets to nonlinear effects: The role of the critical layer. *J. Fluid Mech.*, *811*, 95–137.

Toedtli, S. S., Luhar, M., & McKeon, B. J. (2019). Predicting the response of turbulent channel flow to varying-phase opposition control: Resolvent analysis as a tool for flow control design. *Phys. Rev. Fluids*, *4*(7), 073905.

Towne, A., Lozano-Durán, A., & Yang, X. I. A. (2020). Resolvent-based estimation of space–time flow statistics. *J. Fluid Mech.*, *883*, A17.

Towne, A., Schmidt, O. T., & Colonius, T. (2018). Spectral proper orthogonal decomposition and its relationship to dynamic mode decomposition and resolvent analysis. *J. Fluid Mech.*, *847*, 821–867.

Trefethen, L. N. (2000). *Spectral methods in matlab*. SIAM.

Tropp, J. A., Yurtsever, A., Udell, M., & Cevher, V. (2017). Practical sketching algorithms for low-rank matrix approximation. *SIAM J. Matrix Anal. Appl.*, *38*(4), 1454–1485.

Verzicco, R., & Vittori, G. (1996). Direct simulation of transition in Stokes boundary layers. *Phys. Fluids*, *8*(6), 1341–1343.

Vittori, G., & Verzicco, R. (1998). Direct simulation of transition in an oscillatory boundary layer. *J. Fluid Mech.*, *371*, 207–232.

Von Kerczek, C., & Davis, S. H. (1974). Linear stability theory of oscillatory Stokes layers. *J. Fluid Mech.*, *62*(4), 753–773.

Waleffe, F. (1997). On a self-sustaining process in shear flows. *Phys. Fluids*, *9*(4), 883–900.

Weideman, J. A., & Reddy, S. C. (2000). A matlab differentiation matrix suite. *ACM Trans. Math. Softw.*, *26*(4), 465–519.

Wray, A. A. (1990). Minimal storage time advancement schemes for spectral methods. *NASA Ames Research Center, California, Report No. MS*, *202*.

Yeh, C.-A., Benton, S. I., Taira, K., & Garmann, D. J. (2020). Resolvent analysis of an airfoil laminar separation bubble at Re = 500 000. *Physical. Rev. Fluids*, *5*(8), 083906.

Yeh, C.-A., & Taira, K. (2019). Resolvent-analysis-based design of airfoil separation control. *J. Fluid Mech.*, *867*, 572–610.